Numerical experiments on entrainment, mixing and their effect on cloud dropsize distributions in a cumulus cloud

Paul Vaillancourt
Department of Atmospheric and Oceanic Sciences
McGill University, Montréal

April 1992

A Thesis submitted to the Faculty of Graduate Studies and Research in partial fulfillment of the requirements of the degree of
Master of Science

Abstract

Entrainment, extreme inhomogeneous mixing, in the presence of wind shear, and their effect on cloud droplet spectra are investigated. A dynamical model in conjunction with a microphysical model designed to predict evolution of cloud droplet spectra, is employed to perform a two-dimensional simulation of a small nonprecipitating cumulus cloud in the presence of wind shear.

Results show that vortex circulations and penetrative downdrafts are responsible for entrainment of clear air into the cloud structure. Entrainment and mixing are more severe on the downshear side of the cloud leading to a more fragmented structure and often to total dissipation of cloudy air rather than partial dilution as is the case on the upshear side. Mixing followed by uplifting leads to fresh activation of cloud droplets and results in multimodal spectra. In areas where mixing has occurred, the spectra exhibit smaller average radius and larger standard deviation.

Résumé

Dans ce mémoire nous étudions les processus d'entraînement et de mélange inhomogène en présence de cisaillement dans le vent et leurs effets sur les spectres de gouttelettes d'eau nuageuse. Pour ce faire, nous employons un modèle numérique dynamique jumelé à un modèle numérique microphysique conçu pour prédire l'évolution des spectres de gouttelettes d'eau nuageuse, pour effectuer une simulation en deux dimensions du développement d'un nuage cumulus en présence de cisaillement dans le vent.

Les résultats indiquent que l'entraînement d'air non-saturé à l'intérieur du nuage est dû à la présence de vortex dans la circulation et de courants descendants qui se forment au sommet du nuage. Le côté du cumulus situé en aval du cisaillement a une structure plus fragmentée et est le site d'évaporation complète de petits volumes nuageux plutôt que d'une dilution partielle comme cela se produit de l'autre côté du nuage. Cela est dû au fait que les processus d'entraînement et de mélange sont plus intenses du côté du cumulus situé en aval du cisaillement. Des spectres à plusieurs modes sont obtenus lorsqu'un volume d'air nuageux partiellement dilué est soulevé, ce qui cause l'activation des noyaux de condensation présents. Les spectres, dans les volumes d'air nuageux qui ont été dilués, ont un rayon moyen plus petit et un écart type plus grand.

Acknowledgements

I would like to thank my supervisor, Dr P. Yau, for his patient guidance and thorough correction of this thesis, Dr W. W. Grabowski for his precious help in the use and understanding of the microphysical model developed by him and Dr J. L. Brenguier, Dr T. Clark for providing the dynamical model. I would also like to thank Dr A. Tremblay without whom I would not have been able to run the dynamical model. This research was supported by the office of Naval Research Grant N00014-87-G-0171.

Contents

List of Figures

1 Introduction

1.1 Background

The simplest model of a non-precipitating cloud is given by a closed, homogeneous, moist–adiabatic parcel of air rising in a constant updraft. The droplets in the parcel grow by vapor diffusion from an assumed condensation nuclei spectrum. It is well-known that this simple model leads to monomodal and narrow cloud dropsize spectra (Rogers and Yau, 1989). The maximum size of the droplets is often small except when an abundant supply of giant condensation nuclei becomes available (Johnson, 1982). Numerous observations have shown that this simple model is inadequate. For example:

- Measured in-cloud temperature profiles are much closer to that of the environment than to the moist adiabat (Stommel, 1947);

- Small droplets can be found at all levels within clouds. The dropsize spectrum is frequently broad and bimodal. In-cloud liquid water content is often smaller than the adiabatic value (Warner, 1969a,b).

These discrepancies underline two important problems in cloud physics, namely:

1. The observed cloud dropsize distributions in non-precipitating clouds are significantly broader than those predicted by adiabatic parcel ascent (Warner, 1969b).

2. The observed time for the production of raindrops can be shorter than that calculated from classical theory of condensation growth followed by stochastic coalescence (Baker et al., 1980).

It is obvious that these two problems are not totally independent since any broadening of the dropsize spectra will increase the range of fall velocities and accelerate the rate of formation of precipitation. In particular, a broadening toward larger sizes would have the most important impact.

The inadequacy of the adiabat droplet growth model in explaining the observations has prompted various investigation into its basic assumptions in the past two decades. Specifically, examination of the assumptions of

- *Closed parcel* leads to studies on entrainment (e.g. Stommel (1947) and Squires (1958) have shown that lateral and cloudtop entrainment can significantly dilute in-cloud properties)

- *Homogeneous parcel* leads to studies on variations in relative humidity at cloud base (e.g. Paluch (1971) showed that the effect of the typical variation of the updraft is not important during the early stages of droplet growth by condensation. However, local variations in relative humidity can produce significant variations in droplet sizes.)

- *Constant updraft* leads to studies on the effect of turbulent air motions (e.g. Manton (1979), Cooper (1989) showed that entrainment and mixing introduce variability in the cloud microphysical structure that breaks the close link between supersaturation and vertical velocity, and so can lead to broadening of the size spectra.)

- *Assumed condensation nuclei spectrum* leads to study of the effect of aerosol composition and solubility (e.g. Fitzgerald (1974) concluded that the variability in kind and fraction of soluble material among atmospheric aerosol particles is not important. Johnson (1982) showed that giant and ultragiant aerosol particles are a regular component of the atmospheric aerosol. When present in sufficient concentrations, they can be a significant destabilizing factor in speeding up the development of precipitation.)

- *Classical diffusion growth equation* leads to criticism of the use of macroscopic supersaturation (e.g. Srivastava (1989) argued that the macroscopic supersaturation yields only the average value over a large volume but the supersaturation in the vicinity of a drop can differ significantly from the average value.)

Most of the above studies have, to different degrees, succeeded in explaining some aspects of the broadening of the size distributions. However, the problem remains because there is no general agreement as to which modifications are the more realistic. The picture is further complicated by the fact that very high resolution is needed to resolve these processes. Present limitation in observation and computer resources often require additional assumptions or parameterizations if these processes were to be included in the problem of condensational growth.

At the present time, the most likely candidate in explaining observed cloud droplet spectra is entrainment of environmental air into clouds followed by the mixing of the clear and cloudy air. Research on the role of entrainment has been going on since Stommel in 1947 presented good evidence that cumulus clouds were diluted from mixing of dry air. Many of the subsequent studies have concentrated on the dynamical and thermodynamical effects of entrainment; particularly on the source of the entrained air (see Reuter (1986) for a review of the subject). More recent studies have also addressed the effect of entrainment on cloud dropsize spectra.

How does mixing occur

Prior to 1977 all work on the mixing process assumed that it was uniform and homogeneous. In other words it was assumed that following an entrainment event all droplets at a given level in the cloud are exposed, at the same time, to identical conditions of subsaturation, and therefore all droplets are reduced in size, possibly some being totally evaporated. This parameterization of mixing led to spectra quite unlike those observed (Warner 1973a). Latham and Reed (1977), based on laboratory experiments, suggested an alternative description of the mixing process, i.e. inhomogeneous mixing. They proposed that when undersaturated air enters a cloud, only droplets in direct contact with infilrating blobs or filaments will be affected, being greatly reduced in size or totally evaporated, while other droplets are negligibly affected.

Studies made by Broadwell and Breidenthal (1982) and Baker et al. (1984) concentrated on the actual physical process that produces mixing. Observations of a turbulent shear layer led them to present the following scenario of turbulent mixing:

> As a result of instability at the interface between two fluids, large scale motions develop that transport both fluids, unmixed, across the entire depth of the shear layer. The entrained volumes will break up into smaller and smaller, essentially unmixed, units, causing an increasingly intimate intermingling of the two fluids. This breakdown will continue until the Kolmogorov scale is reached, which in the case of mixing between cloudy and cloud free air will occur when filaments of mixing air have scales near $\approx 1mm$. Approaching this scale, the interfacial area grows very rapidly and remaining structures are destroyed by molecular diffusion.

Adopting this description, mixing is roughly a two-stage process: During the first stage, the breakdown of the entrained volumes, evaporation of droplets only occurs at clear–cloudy interfaces resulting in a few droplets being substantially affected. Note that during this stage, a measuring instrument (resolution large compared to Kolmogorov scale) would measure an average spectrum of the same shape as that in the original cloudy air but diluted by unresolved filaments of cloudfree air. During the second stage, when the Kolmogorov scale is reached, all droplets experience the same environment. If the air is subsaturated, uniform evaporation of all droplets follows. Mixing can be described as homogeneous if the first stage is very rapid or extreme inhomogeneous if it is very slow. The real case would lie between these two extremes and the exact state would depend on the level of turbulence, i.e on the rate of thinning of the filaments of clear and cloudy air.

What is predicted by models about how mixing affects spectra

Numerical models have been used to test different parametizations of mixing and how they affect dropsize spectra. It was found by Baker et al. (1980), Hill and Choularton (1986) and Bower and Choularton (1988) that inhomogeneous mixing can lead to superadiabatic growth. In their models, each mixing event causes a decrease in concentration of droplets. Droplets that survive experience a new peak in supersaturation as the air parcel is carried upwards and would grow to sizes larger than those given by an adiabatic ascent. Whether superadiabatic growth actually occurs depends critically on whether a number of events can be realized: For peaks in the supersturation to occur, the mixed parcel must rise. The same parcel must experience several of these peaks and must therefore undergo several mixing events. Also the same large droplets must avoid evaporation at each mixing event. Moreover, these studies assume that fine-scale mixing will rapidly and uniformly mix the entrained nuclei throughout the parcel before they are activated. If this is the case the supersaturation can increase before the entrained nuclei are activated and grow sufficiently to compete for the available water. However, if the entrained nuclei are activated before they are uniformly mixed throughout the parcel, supersaturation will not increase (Brenguier, 1990).

Telford and Chai (1980) suggested a theoretical scenario, called entity type entrainment model(ETEM), which leads to broader spectra and larger maximum drop sizes. Enhanced growth is again a result of the lifting of a parcel containing a reduced number of droplets. However, in their scenario, the reduction in concentration of droplets is not a result of inhomogeneous mixing with clear air but rather of entrainment of droplets into saturated penetrative downdrafts from adjacent ascending parcels. Small vertical velocities, which ensure that not all nuclei are reactivated when the mixed parcel rises, and multiple vertical cycling of the same parcel are necessary conditions for enhanced growth. Note that in this scenario as well as in superadiabatic growth due to inhomogeneous mixing the largest droplets are predicted to be found in diluted parcels of cloudy air.

Cooper (1989) developed a general framework, which is independant of the exact sequence of the motion or mixing of the parcels, to predict the effect of the observed turbulent stucture of clouds on spectra. He suggested that " simple turbulent motions in a stochastically varying cloud may provide significant broadening of the spectra if those motions are accompanied by a variable microphysical structure produced by *dry-air entrainment.*"

What do observations show

Concurrent with the development of theoretical and conceptual ideas is the analysis of mixing from observational data. In mixed regions of clouds, large fluctuations of droplet concentration are measured (Paluch and Baumgardner 1989). Because the sampling rate of the measuring instruments is not infinite the question remains as to whether a measured low concentration characterizes an actual homogeneous droplet population at the scale of the sample or if it is a result of averaging highly variable concentrations in a heterogeneous sample. Paluch and Baumgardner (1989), in a study on continental cumuli, compared the droplet concentrations sampled at 1 Hz (100m sample) and 50 Hz (2m sample). They showed that the former significantly underestimates the local concentration of droplets because large changes in droplet concentration were observed over distances of the order of meters. They also reported that:

- No increase in maximum droplet sizes with increasing dilution of droplet concentration was observed.

Similar results were also reported in other studies(e.g. Paluch and Knight 1984, Blyth and Latham 1985). These observations indicate that superadiabatic droplet growth as predicted by certain conceptual models described earlier is probably quite rare in continental clouds. However, some contradicting results exist. Hicks, Pontikis and Rigaud (1990) in a study on continental cumuli and on tropical band clouds, did find that the highest concentrations of large droplets were present in samples with an intermediate degree of dilution on the downshear side of clouds.

- The large droplet peak of the spectrum remains at a nearly constant diameter despite major variations in local concentrations.

Brenguier (1990) also reported similar results. Using high resolution measurements and statistical techniques he showed that this was due to the fact that regions with large variations in droplet concentrations are mostly inhomogeneous and that local concentrations are in fact similar to concentrations measured in regions where fluctuations are small.

Most of the observations described above show that mixing does not lead to large uniformly mixed cloud volumes with low droplet concentrations. This suggests that the rate of turbulent mixing is slow and therefore supports the extreme inhomogeneous description of mixing. It is noted that not all studies support this conclusion. Some have reported the existence of large highly diluted regions with uniform characteristics (Austin et al. 1985, Jensen et al. 1985). While a satisfactory resolution of the apparent conflict between different sets of observations still awaits further investigation, we consider that the evidence presented by Paluch and Baumgardner (1989) and Brenguier (1990), using new techniques permitting a more precise evaluation of the local concentration of droplets, in support of the scenario of extreme inhomogeneous mixing is sufficiently appealing to warrant a more detailed numerical study.

1.2 Thesis objectives and outline of content

The objective of this thesis is to study the processes of entrainment and mixing(a specific definition of these terms is given in Chapter 3) and to determine how they affect the cloud dropsize distributions in a small non-precipitating continental cumulus cloud in a sheared environment. Clouds generally develop in an environment with wind shear and observations have shown that the upshear portions of clouds are typically warmer and wetter than their downshear sides (Heymsfield et al., 1978) and are preferred sites for subsiding motion and decay. (Telford and Wagner, 1980). Thus differences in terms of mixing and cloud dropsize distributions are to be expected in the up and downshear portions of clouds. Specifically, we shall investigate the following questions:

1. How and where does entrainment and mixing occur?

2. Is there any differences between the upshear and downshear sides of cloud in terms of entrainment and mixing?

3. How are cloud dropsize distributions modified by extreme inhomogeneous mixing?

Our approach would be to perform high resolution simulations using a numerical cloud model.

This thesis is organized into four chapters. In addition to the brief review of past research presented here, the numerical model and the setup of experiments are discussed in Chapter 2. The results form the subject of Chapter 3. Summary and concluding remarks are in Chapter 4.

2 The Numerical Model

In this thesis, the two-dimensional, slab-symmetric version of the cloud model developed by Clark (1977,1979) is used. Condensation is calculated by a bulk scheme. Certain fields from the bulk model serve as input into a microphysical model developed by Brenguier and Grabowski (1992)(hereafter referred to as BG), where the droplet spectra will be predicted.

2.1 Dynamical model

Clark's model is nonhydrostatic. The anelastic assumption supports gravity waves but filters out acoustic waves. The momentum equations are solved using the second-order accurate, centered time and centered space finite difference scheme of Lilly (1965) and Arakawa (1966). Advection is treated by the advection algorithm of Smolarkiewicz (1984) with one corrective iteration and with monotonicity correction (Smolarkiewicz and Grabowski 1990) for all thermodynamic variables. Moist thermodynamics is restricted to the condensation evaporation process. Sedimentation, coalescence, and ice phase processes are not included. An interactive nesting technique (Clark and Farley 1984) is employed.

The notation used to represent the thermodynamic variables is :

$$T = \overline{T}(z) + T'(z) + T''(\mathbf{x}, t) \tag{1}$$

$$P = \overline{P}(z) + P'(z) + P''(\mathbf{x}, t) \tag{2}$$

$$\rho = \overline{\rho}(z) + \rho'(z) + \rho''(\mathbf{x}, t) \tag{3}$$

$$\theta = \overline{\theta}(z) + \theta'(z) + \theta''(\mathbf{x}, t) \tag{4}$$

$$q_v = \overline{q_v}(z) + q_v'(z) + q_v''(\mathbf{x}, t), \tag{5}$$

where T, P, ρ, θ, q_v denote the air's absolute temperature, pressure, density, potential temperature and water vapor mixing ratio. $\mathbf{x} = (x, z)$ is the two dimensional coordinate system. Any variable can be written as the sum of an overbarred term (denoting conditions for an idealized atmosphere with constant stability S), a single primed term (denoting deviations of the hydrostatically balanced initial conditions from the constant stability profiles), and a double primed term (denoting the time-dependent perturbations). Using the anelastic approximation where the local time variation of density is neglected, the momentum and continuity equations can be written as

$$D\mathbf{u}/Dt = -\nabla(P''/\overline{\rho}) + \mathbf{k}g(\theta''/\overline{\theta} + \epsilon q_v'' - q_c) + \frac{1}{\overline{\rho}}\nabla \cdot \tau \tag{6}$$

$$\nabla \cdot (\overline{\rho}\mathbf{u}) = 0, \tag{7}$$

where $\mathbf{k}$ denotes the vertical unit vector, $\epsilon = R_v/R_d - 1$, and τ is the stress tensor. The conservation equations for heat and water substances are:

$$\overline{\rho}D\theta/Dt = \overline{\rho}L\theta_e/C_pT_e + \nabla \cdot (\overline{\rho}K_m\nabla\theta) \tag{8}$$

$$\overline{\rho}Dq_v/Dt = -\overline{\rho}C_d + \nabla \cdot (\overline{\rho}K_m\nabla q_v) \tag{9}$$

$$\overline{\rho}Dq_c/Dt = \overline{\rho}C_d + \nabla \cdot (\overline{\rho}K_m\nabla q_c), \tag{10}$$

where $T_e = \overline{T} + T'$ and $\theta_e = \overline{\theta} + \theta'$ are initial environmental profiles, q_c is the cloud water mixing ratio, C_d the condensation/evaporation rate and K_m

is the eddy mixing coefficient. These equations are solved with advection and eddy mixing as a first step and adjustments associated with condensation/evaporation as the second step. The subgrid-scale turbulence is parameterized according to the first-order theory of Smagorinsky (1963) and Lilly (1962) where the stress tensor is approximated as:

$$\tau_{ij} = \overline{\rho} K_m D_{ij}, \tag{11}$$

with D_{ij} the deformation tensor, is written as

$$D_{ij} = \frac{\partial u_i}{\partial x_j} + \frac{\partial u_j}{\partial x_i} - \frac{2}{3}\delta_{ij}\frac{\partial u_k}{\partial x_k}. \tag{12}$$

By defining the net deformation squared as

$$Def^2 = \frac{1}{2}\sum_i \sum_j D_{ij}^2, \tag{13}$$

the eddy mixing coefficient takes on the form

$$K_m = \begin{cases} (C\Delta)^2/2^{1/2} Def(1-R_i)^{1/2} & \text{if } R_i < 1 \\ 0 & \text{if } R_i > 1, \end{cases} \tag{14}$$

where R_i is a local Richardson number

$$R_i = g\left(\frac{\partial B}{\partial z} + S\right)/Def^2. \tag{15}$$

The buoyancy, B, and the environmental stability, S, are given by:

$$B = \theta'/\overline{\theta} + \epsilon q_v - q_c, \tag{16}$$

$$S = \frac{\partial}{\partial z}\ln\overline{\theta}. \tag{17}$$

2.2 Microphysical model

The microphysical model exerts no feedback on the dynamics of the bulk model. It uses as input the condensation/evaporation rate C_d and the cloud water mixing ratio q_c to infer the value of supersaturation (or subsaturation) in calculating the evolution of the dropsize spectra. The velocity and buoyancy fields are also required to calculate changes in the spectra due to advection and eddy mixing of droplets.

2.2.1 Model assumptions: explanation and justification

The approach developed in BG is based on four assumptions.

> 1) "The amount of water substance subject to phase change is taken as predicted by the bulk model."[1]

The amount of condensation/evaporation at each time step is calculated from the bulk model by assuming that the relative humidity is always 100% at the end of each time step. This assumption is justified as calculations have shown that the typical values for supersaturation inside a nonprecipitating cloud are small, of the order of .1%. Near the cloud base where the activation of cloud condensation nuclei is not yet complete or in regions of entrainment the supersaturation can be an order of magnitude higher ($\approx 1\%$). However, Grabowski (1989) has compared the evolution of a simulated cloud

[1] Brenguier and Grabowski, "Cumulus entrainment and cloud droplet spectra: A numerical model within a two-dimensional dynamical framework", accepted for publication in *JAS*, pp.5,26

using a bulk condensation/evaporation scheme against one where condensation/evaporation process is treated explicitly and concluded that a detailed treatment of condensation/evaporation imposes a relatively minor effect on cloud dynamics and thermodynamics.

> 2) "Nucleation of droplets is assumed to always produce the same initial droplet spectrum f_o."[2].

The implications of this assumption are that the CCN size distribution and the maximum supersaturation in regions where nucleation takes place do not vary in time and space.

The assumption of a uniform CCN distribution is of course a gross simplification as observations generally show that the number concentration of CCN varies with height over continents and oceans (Pruppacher and Klett 1978). However, BG has shown in a numerical simulation that the circulations induced by a cloud transports CCN upwards. Therefore even when secondary nucleation occurs at levels other than the cloud base, the local CCN spectrum is strongly modified by the CCN distribution in the boundary layer.

It is known that strong variation of supersaturation can be found in a cloud where entrainment occurs. Observations (Paluch and Baumgardner 1989) and high resolution cloud simulations with detailed microphysics (Grabowski 1989) indicate that entrainment can produce strong variation in

[2] *ibid*, pp 6,25-26.

properties of the cloud on scales as small as meters. In particular, the fluctuations in supersaturation are larger in diluted cloud regions than in undiluted cores (Politovich and Cooper 1988, Grabowski 1989). A further complication was pointed out by Srivastava (1989) who suggested that it is the supersaturation in the vicinity of a drop which is relevant to its growth rate. The use of an average supersaturation over a macroscopic volume to calculate the growth of droplets may be inappropriate. He further formulated a scheme for the evolution of supersaturation and droplet growth by condensation which includes the random distribution of droplets and the variations in vertical air velocity.

The above discussion has shown that the explicit modeling of secondary activation would require extremely high resolutions which is impractical given the limitation in speed and memory size of the present generation computers. Srivastava's microscopic approach for condensational growth was also not attempted because of excessive demand on computational resources and because of numerical difficulties. As a first attempt, it is simply assumed that the maximum supersaturation achieved at all nucleation regions is the same and therefore the same prescribed CCN spectrum is activated.

> 3) "Locally, only droplet concentration corresponding to that at nucleation may be present."[3]

[3] *ibid*, pp.3,6-7,23,25-26

This assumption can be justified on two counts. First, observations have shown that at a given level in a cloud, the shape of the droplet size distribution is almost constant despite large fluctuations in droplet concentrations (Paluch and Knight 1984, Paluch and Baumgardner 1989, Brenguier 1990). The explanation, as revealed by high resolution measurements, is that these regions with large fluctuations of droplet concentrations are actually composed of sub-regions with low or zero concentrations and sub-regions where the local concentrations are similar to those characterized by small fluctuations in number concentrations. In other words, the apparent variation in number concentration may be an artifact of the inadequate resolution in the sampling rate. Secondly, Paluch and Baumgardner (1989) deduced that the time scale to complete a mixing event (i.e. the duration to completely homogenize an initial mixture of cloud and clear air with a typical dimension of 100 m), is comparable to the time scale of the evolution of the cloud. Because it takes a long time for filaments of cloudy and clear air to break down to the Kolmogorov microscale where homogenization takes place, and because the droplet concentration would only be substantially modified on that scale (Jensen and Baker, 1989), the local droplet concentration would likely stay the same as that at nucleation.

> 4) "After nucleation further evolution of the cloud droplet spectrum is represented using base functions (called elementary droplet populations) which are spectra generated from f_o, the initial

droplet spectrum, through further condensational growth."

This method will be explained in the next section.

2.2.2 Formulation of the microphysical model

As described in Brenguier (1991) a cloud droplet spectrum can be represented as a combination of narrow base functions called elementary droplet populations (EDP). An EDP is defined as an ensemble of droplets having followed the same trajectory in the cloud. The droplets have therefore encountered the same sequence of supersaturations. An EDP is represented by an elementary size distribution $f(r,t)$, which satisfies the kinetic equation:

$$\frac{\partial f}{\partial t} = -\frac{\partial}{\partial r}\left[\frac{f dr}{dt}\right]. \tag{18}$$

The term $\frac{dr}{dt}$ is the time rate of change of radius by condensation/ evaporation. If the solute and curvature effects are neglected, it can be written as:

$$\frac{dr}{dt} = \frac{A_1 s_e}{r+a} \tag{19}$$

where s_e is the supersaturation, $a = 2\mu m$ is the length associated with the accommodation coefficient, and A_1 is a slowly varying function of pressure and temperature. By integrating (19) along the trajectory followed by the droplets, and by assuming that the variation in temperature is small so that $A_1 \approx$ constant, we obtain

$$(r+a)^2 = (u+a)^2 + b^2(t), \tag{20}$$

where $u = r(t_0)$ is the radius of the droplet at activation time t_0, and r is the radius at observation time t. Also

$$b^2(t) = 2A_1 \int_{t_0}^{t} s_e(t)dt. \tag{21}$$

By using (20) and (21), the general solution to the kinetic equation (18) (see Brenguier 1991) can be expressed as:

$$f(r,b) = f_0(u)\frac{(r+a)}{(u+a)} \tag{22}$$

$$f(r,b) = f_0(u)\left[1 + \frac{b^2(t)}{(u+a)^2}\right]^{1/2}. \tag{23}$$

An EDP is therefore a function of the elementary size spectrum at nucleation $f_0(u)$ and its degree of condensational growth $b^2(t)$. As explained in Brenguier (1991) the EDP's can be used as base functions to calculate the mixing ratio of the size distribution of cloud droplets (number per unit mass of air per unit radius interval):

$$h(\mathbf{x},r,t) = \sum_{i=0}^{n_c-1} \psi_i(\mathbf{x},t) f_i(r), \tag{24}$$

where n_c is the total number of base functions. f_i is numbered from 0 to $n_c - 1$. $\psi_i(\mathbf{x},t)$ is the weight function associated with the i^{th} base function at the grid location $\mathbf{x}$ at time t. By definition $0 \leq \psi_i(\mathbf{x},t) \leq 1$ and $\sum \psi_i(\mathbf{x},t) = \beta(\mathbf{x},t) \leq 1$, $\beta(\mathbf{x},t)$ gives a measure of the degree of inhomogeneity. In a unit cloud volume characterized by a certain value of β, a fraction β of the volume will be assumed to consist of cloudy air and the remaining fraction (1-β) of clear air. In principle, the mixing ratio of the size distribution can be used to calculate the number density function defined as $g = h\rho$. If sedimentation is neglected, the conservation equation for $g(\mathbf{x},r,t)$ is (Grabowski 1989):

$$\frac{\partial g}{\partial t} = -\nabla \cdot (\mathbf{u}g) + \nabla \cdot (K\nabla g) - \frac{\partial}{\partial \lambda}\left(\frac{d\lambda}{dt}g\right) + P_g, \tag{25}$$

where $\mathbf{u}$ is air velocity and $\lambda = b^2$. The first term on the right hand side represents advection, the second is eddy mixing, the third is the condensation/evaporation process and the last term P_g is associated with nucleation. In practice, (25) is not explicitly used. Instead, in the framework developed by BG, the evolution of the weight functions associated with each base function is calculated in two steps. First, the effects of advection and eddy mixing in physical space are computed from

$$\frac{\partial \rho\psi_i}{\partial t} + \nabla \cdot (\rho u^* \psi_i) = 0, \tag{26}$$

where $\mathbf{u}^*$ is the velocity field which already includes diffusive fluxes. Then the effect of condensational/evaporation is represented by the transport of ψ in $\lambda(\lambda = b^2)$ space as:

$$\frac{\partial \psi}{\partial t} + \frac{\partial}{\partial \lambda}\left[\frac{d\lambda}{dt}\psi\right] = 0, \tag{27}$$

For example if the drops are growing, the weight functions ψ will be associated with larger and larger values of b^2. Condensation and evaporation are parameterized differently depending on whether the grid volume is homogeneous ($\beta = 1$) or inhomogeneous ($\beta < 1$).

a) *Homogeneous grid volume*

In this case it is assumed that all droplets experience the same supersaturation whose value is calculated in a manner consistent with the first assumption described in section (2.2.1). We first assume a certain supersaturation S^*, and then calculate using equation (27) the resulting weight functions ψ^* and the change in cloud water mixing ratio : $\Delta q^* = \sum_i q_i(\psi_i^* - \psi_i)$ where q_i is the mixing ratio associated with the base function f_i. Since the change in cloud water mixing ratio is proportional to supersaturation , $S = \frac{S^*\Delta q}{\Delta q^*}$, where Δq is the change in cloud water mixing ratio predicted by the bulk model. The value of supersaturation S can then be used in (27) to calculate the actual evolution of the droplet spectrum.

b) *Inhomogeneous grid volume*

When condensation occurs ($\Delta q > 0$), the growth of the drops in the undiluted β portion of the grid volume is the same as in a homogeneous grid volume but using $\psi_i^H = \psi_i/\beta$. In the remaining $1 - \beta$ cloud free portion, nucleation and possibly some growth will occur. If $\Delta q < q_0$, where q_0 is the mixing ratio associated with the nucleation spectrum f_0, then partial activation occurs and $\psi_0^I = \Delta q/q_0$. If $\Delta q > q_0$, activation of all nuclei in f_0 will occur followed by some condensational growth of the amount $\Delta q - q_0$. The weight functions are then given by ψ_i^{*I}. To ensure that the increase in cloud water mixing ratio is exactly Δq calculated from the bulk model, the final weight function is calculated as $\psi_i^* = \beta\psi_i^{*H} + (1-\beta)\psi_i^{*I}$.

When $\Delta q < 0$, evaporation can only occur in the β portion of the grid volume where the cloud water mixing ratio has to decrease by the amount $\Delta q/\beta$. In the model, evaporation can result either from descending motions or mixing. In the former case, evaporation is homogeneous and in the latter case it will be extreme inhomogeneous. However, there is no simple way to determine exactly the relative contribution of these two evaporative processes, being dependent on the cause of evaporation and the subgrid-scale structure of the thermodynamic and dynamic fields. For simplicity, it would be assumed that homogeneous evaporation occurs in $\beta\delta$ portion of the grid volume and extreme inhomogeneous evaporation in the remaining $\beta(1-\delta)$ portion. Formally, for extreme inhomogeneous evaporation, the weight functions before and after the evaporative process are related via the formula $\psi_i^{*I} = \epsilon\psi_i^I$, where $\psi_i^{*I} = \psi_i/\beta$. Physically, ϵ is the fraction of cloud water remaining in a grid volume after evaporation and is given by $\epsilon = (q_c^m + \Delta q)/q_c^m$, where q_c^m is the cloud water mixing ratio prior to evaporation. To ensure that the change in cloud water mixing ratio equals Δq, the final weight function is calculated as $\psi_i^* = \beta[\delta\psi_i^{*H} + (1-\delta)\psi_i^{*I}]$. In this study, it will be assumed that $\delta = \beta$. This assumption makes physical sense because when the grid volume is homogeneous ($\beta = 1$), only homogeneous evaporation occurs. When the grid volume is considered inhomogeneous ($\beta < 1$), both homogeneous and extreme inhomogeneous evaporation occur. In particular, the smaller the value of β, the more will clear air be mixed in with the cloudy air and the more will the evaporation be extreme inhomogeneous .

2.3 Setup of Experiments

2.3.1 Dynamical model

a)*Computational domain and boundary conditions*

Four experiments were performed. Expt. 1 is the case with no environmental wind shear. Expt. 2 is the control case where the environmental wind varies with height and where the parameter $\delta = \beta$. Expt.3 and Expt. 4 are similar to the control except that the values for δ are set to 0 and 1 respectively. For reasons of economy, we will only discuss the control in detail. The other cases will be commented on very briefly in the conclusion. Two interacting domains are used in these experiments. The outer domain has 98×98 grid points with a resolution of $45m$. The area simulated is therefore $4410m \times 4410m$. The inner domain has 98×98 grid points with a resolution of $15m$ for a total area of $1470m \times 1470m$. The outer domain is large enough to properly resolve the convective circulation resulting from the thermal forcing in the boundary layer described in the next section. The inner domain provides higher resolution where the cloud forms and evolves. A uniform time step of 2 seconds is used in the two domains.

For the outer domain , cyclic boundary conditions are specified in the horizontal, at the upper and lower surfaces the boundary conditions are:

$$\frac{\partial}{\partial z}(v, q_v, q_c, \theta) = w = 0 \ at \ z = 0, H \ , \tag{28}$$

where H is the top of the outer domain, and v is the horizontal velocity in the x direction in the x-z coordinate system. The interactive grid technique of Clark and Farley (1984) is used. Basically, at each time step, the outer grid supplies boundary information for the inner model. Integration of the inner model then takes place. At the end of the time step, the inner model variables are averaged onto the outer model grid. A two-way interaction is thereby effected.

b)*Initial conditions and cloud forcing*

The initial environment is very similar to the one given in Klaassen and Clark (1985) which was chosen to represent one of the simplest atmospheric conditions that can support the growth of small cumulus clouds. Figure 1*a* shows the initial profiles of θ and q_v. The lowest 1.4 km is the boundary layer characterized by a slightly stable potential temperature gradient ($0.36K \ km^{-1}$) and a mixing ratio profile which decreases from $8.5g \ kg^{-1}$ at the surface to $8.0g \ kg^{-1}$ at $z = 1.4km$. Between $z = 1.4 \ and \ 1.8km$ we specify a layer of strong stability ($d\theta/dz = 4K \ km^{-1}$) where the relative humidity decreases from 91% to 39%. Above $z = 1.8km$ the potential temperature gradient is $4.5K\ km^{-1}$ while the relative humidity decreases to 23% at $z = 3.0km$. The humidity decreases at a slower rate thereafter.

For the specified initial condition, the lifting condensational level for a parcel rising from the surface is $1.4km$. For saturated adiabatic ascent the point of neutral buoyancy is at $2.5km$.

In the experiments where the wind varies with height, a vertical wind shear of $3.0m\ s^{-1}\ km^{-1}$ is specified from $z = 1.4km$ upwards. Figure 1*b* shows the initial horizontal wind field as well as the position of the inner domain. The location of the inner domain is chosen so that most of the cloud would stay within the inner domain during its life cycle.

To initiate the cloud circulation we apply a surface sensible heat flux $F(x,z)$ following the manner of Klaassen and Clark (1985):

$$F(x,z) = F_0 exp[-\frac{(x-x_0)^2}{\alpha^2}]exp(-\frac{z}{\sigma}), \tag{29}$$

where x_0 is the center of the outer domain, and $F_0 = 150Wm^{-2}$ is the maximum surface heat flux at x_0. The half height of the boundary layer is $\sigma = 700m$ and $\alpha = 300m$ is the horizontal attenuation length. The type of forcing specified provides a smooth initialization of the cloud, and is considered more realistic than "buoyant bubble" initialization since no buoyancy shock is introduced. In our case, the cloud retains its initial shape for a long time and the cloud base remains essentially at the initial lifting condensational level.

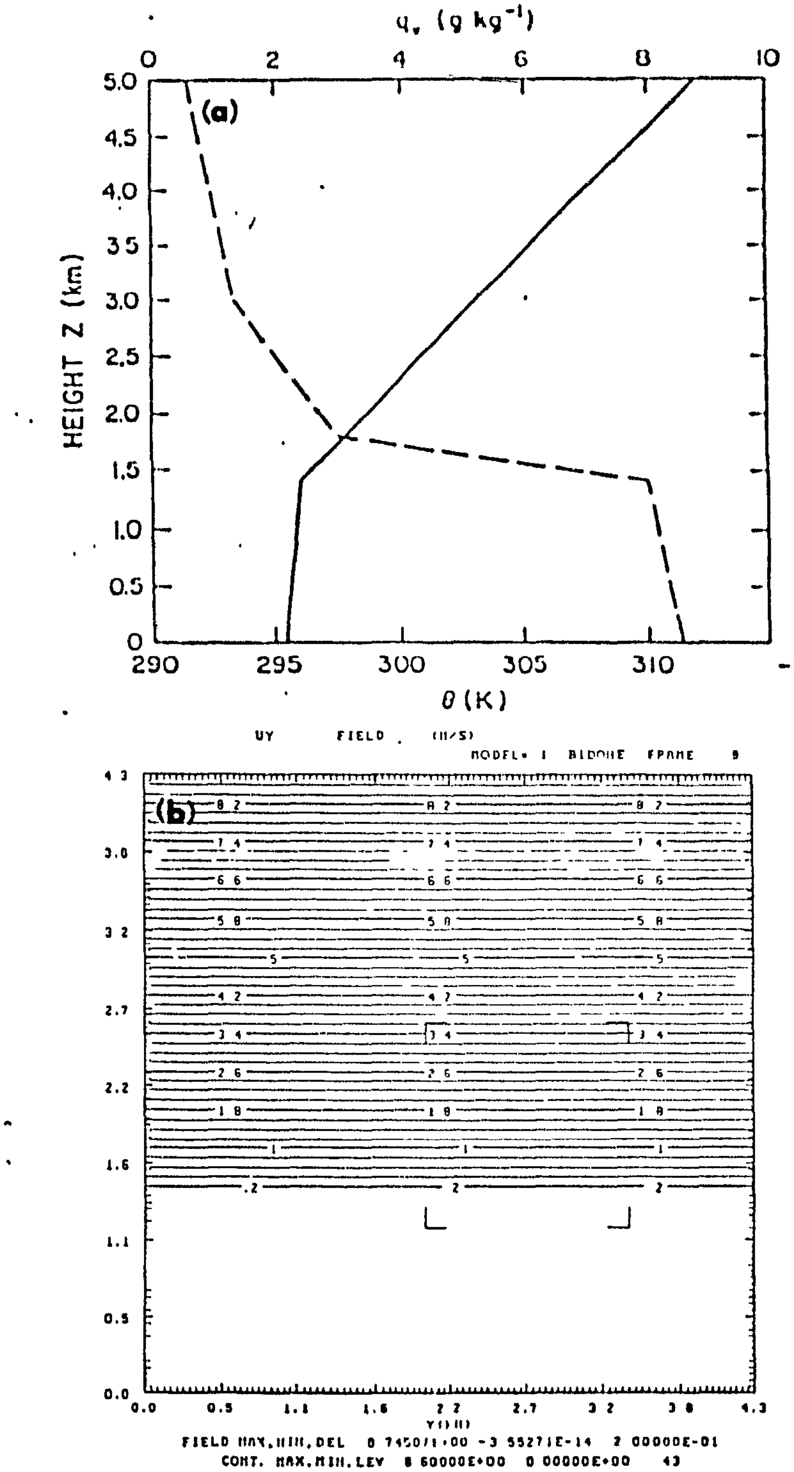

Figure 1: Initial environmental conditions: (a) vertical profile of potential temperature, θ (solid line), and water vapor mixing ratio, q_v(dashed line). This figure is taken from Klassen and Clark (1985); (b) horizontal wind field.

2.3.2 Microphysical model

In all experiments the number of base functions is $n_c = 30$. Each base function is associated with a b^2 value linearly distributed from $b^2 = 0$ to $b^2 = (r_{max} + a)^2 - (r_0^- + a)^2$ (see equation 20). Here $r_0^- = 1\mu m$ is the smallest activated nuclei, $r_{max} = 12\mu m$ is the radius of the smallest droplet associated with the 30^{th} base function and $a = 2\mu m$. The nucleation spectrum f_0 is chosen as in Brenguier (1991), with the form ; $f_0(r_0) = k/r_0^{\gamma+1}$ for $r_0^- \leq r_0 \leq r_0^+$ and $f_0(r_0) = 0$, otherwise.

The values of the parameters are $k = N_0\gamma/[(r_0^-)^{-\gamma} - (r_0^+)^{-\gamma}], N_0 = 10^3 mg^{-1}$ ($10^3 cm^{-3}$ for a density of $1 kgm^{-3}$), $\gamma = 3$ and r_0^+ (the size of the largest activated nuclei)$= 15\mu m$.

3 Results

The results of the control experiment are presented in four sections. The first section gives a general overview of the cloud's structure and its evolution in terms of various peak quantities. The second section is devoted to explaining the format of presentation for the microphysical model. In the third section we will identify entrainment sites and zones of important mixing. Finally, the effect of entrainment and mixing on cloud dropsize distributions will be investigated.

3.1 General features of dynamical model results

As a result of surface heating, convective circulation develops in the boundary layer. The thermal updraft near the center of the domain carries air from the surface to the lifting condensation level near the top of the boundary layer at $1440m$. Figure 2 shows a highly symmetrical vertical velocity field at $t = 30min.$. The narrow thermal updraft, with a maximum velocity of $2.9m/s$, is flanked by wider areas of subsiding motion having a maximum amplitude of $-1.1m/s$.

After $\approx 34min.$, the cloud starts to form. Table 1 lists the characteristics of the development of the cloud from $t = 38min.$ to $t = 50min.$. Throughout the life cycle of the cloud, the rate of rise of the cloud top, defined as the highest level where $q_c = 0.1g/kg$, varies between 0.5 and $1.0m/s$; with an average value of $0.8m/s$.

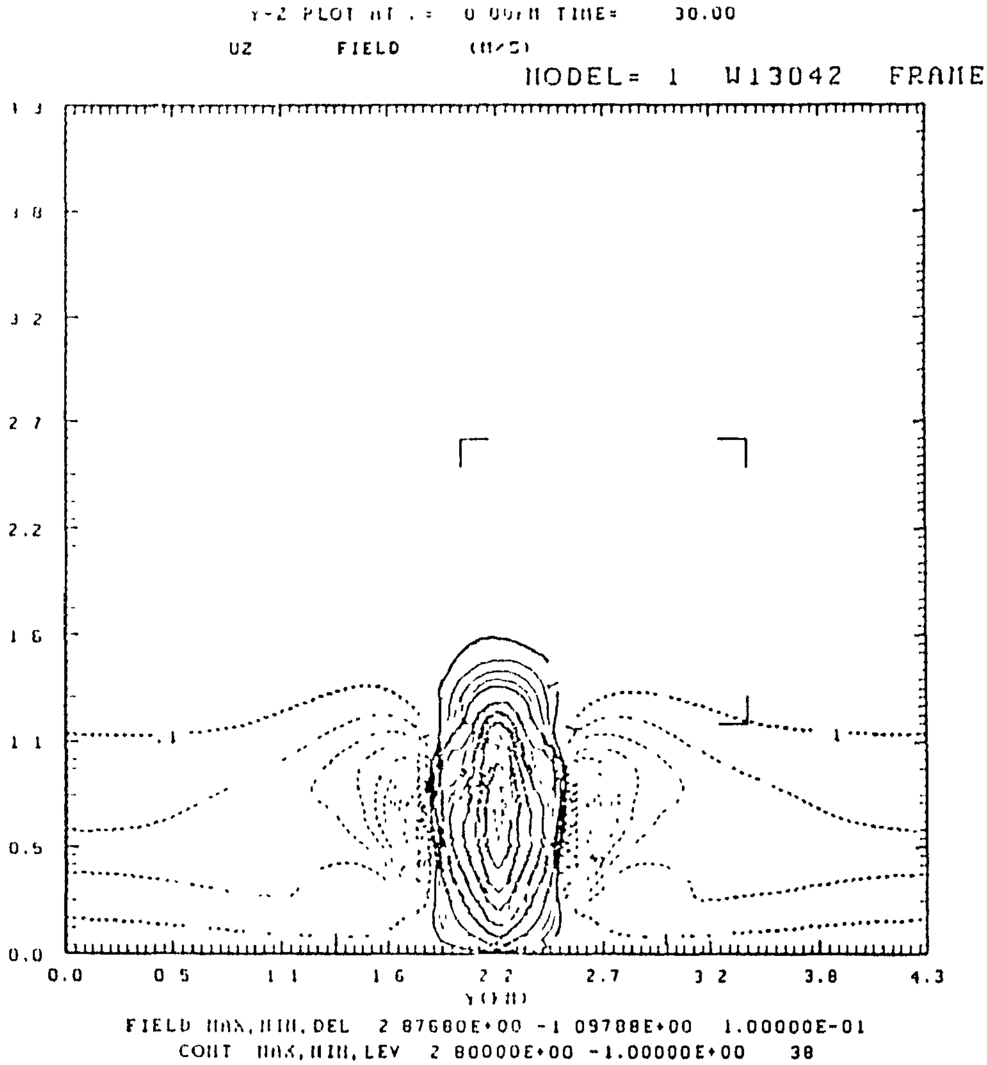

Figure 2: Vertical wind field at $t = 30min$.

The cloud area, given by the number of grid points in the inner domain with a liquid water mixing ratio exceeding $0.1g/kg$, increases to a maximum of 906 at $t = 45min$.. Thereafter, the cloud area decreases and the dissipation of the cloud is almost complete by $t = 54min$.. The life cycle of the cloud is therefore $\approx 20min$..

In terms of the peak vertical velocities and liquid water content, the simulated cloud shows values typically found in observed small cumuli. The

Table 1: Characteristics of cloud evolution

Time ($min.$)	**Cloud top** (m)	**Cloud area** [4]	**Max. q_c** (g/Kg)	**Maximum updraft** (m/s)	**Maximum downdraft** (m/s)
38	1 665	282	0 41	2 39	-1 17
40	1 740	465	0 59	2 26	-1 74
42	1 845	680	0 78	2 46	-2 31
43	1 905	791	0 88	2 99	-2.53
44	1 950	875	0 99	3 23	-3 42
45	1 980	906	1 11	3 34	-3 57
46	2 040	867	1 20	3 50	-3.93
47	2 100	823	1 20	5 10	-3 66
48	2 130	782	1.29	5 02	-3 40
49	2 190	694	1 43	3 90	-3 79
50	2 235	551	1 34	3 61	-3 64

respective maximum cloud water content, updraft and downdraft speeds are $1.43 g/kg$ (at $49min.$), $5.10 m/s$ (at $47min.$), and $-3.93 m/s$ (at $46min.$).

The general cloud structure is shown in figures 3,4 and 5 which depict a time sequence of q_c contours from $t = 38$ to $50min.$. From a rather symmetrical distribution of q_c at $38min.$, a descending arm becomes noticeable on the upshear side at $42min.$ A bubble-like structure begins to develop on the downshear side at $44min.$ Complex evolution of this structure follows and a highly asymmetric cloud results after $46min.$. It should be noted that the cloud structure is more complex or convoluted on the downshear side.

In contrast to conditions at the cloud edges and the cloud top, the gradient of q_c in the cloud core is relatively small. The value of q_c increases vertically by $\approx 0.1 g/kg$ *per* $50m$. A much stronger gradient is found at the cloud-

[4]Area is given in number of grid boxes($15m$ by $15m$) with $q_c > 0.1$

environment interface, especially at the cloud top where q_c passes from its maximum value to near zero in a distance of $30m$. In certain areas of the cloud, for example on its upshear side at $t = 46min.$, the gradient of q_c varies strongly even at some distance inside the cloud. As will be shown in section 3.3.1, these areas correspond to extended regions of mixing or so called mixing zones.

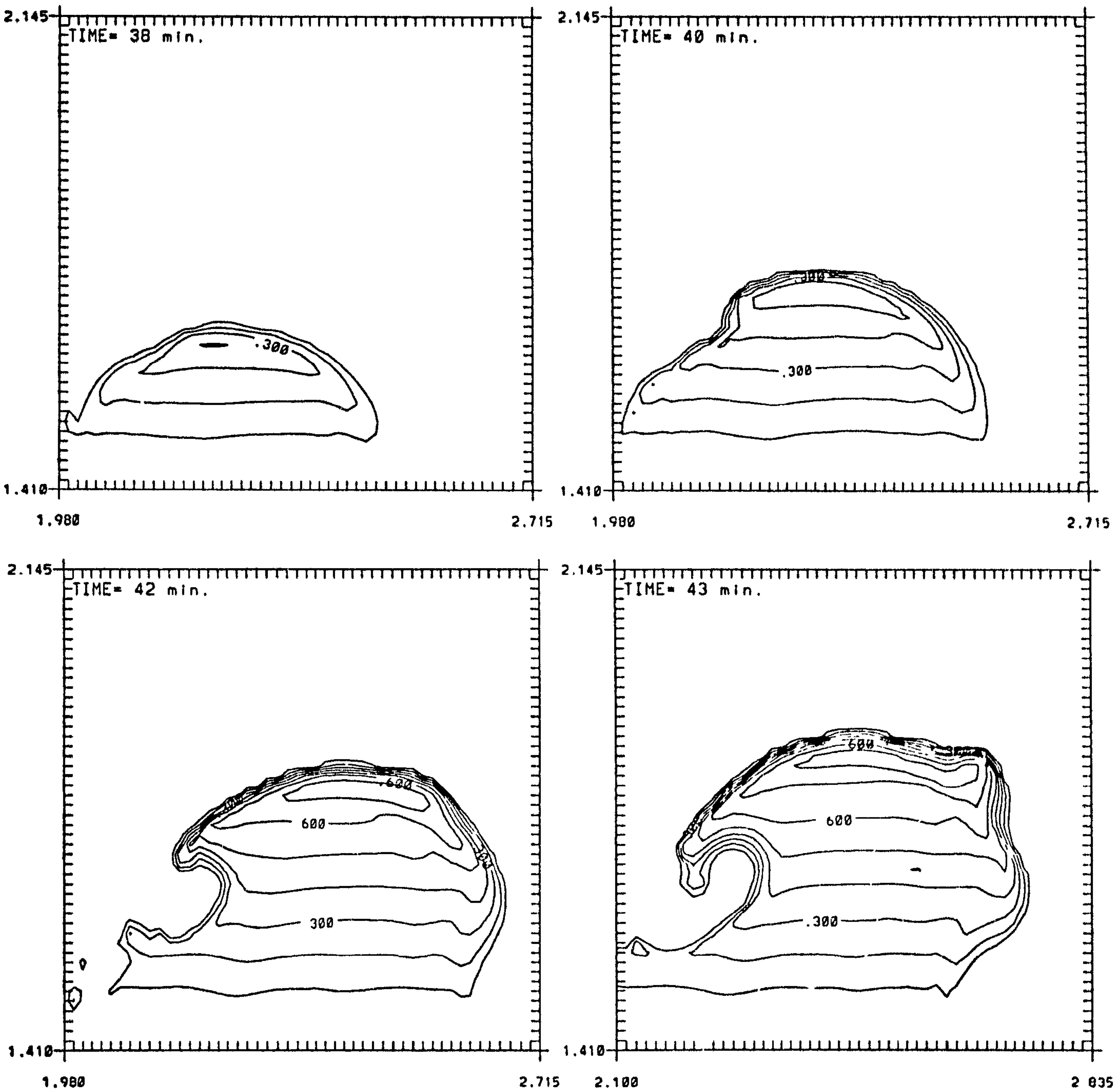

Figure 3: Cloud water mixing ratio, q_c, for $t = 38, 40, 42, 43 min.$, contour interval $0.1 g/kg$.

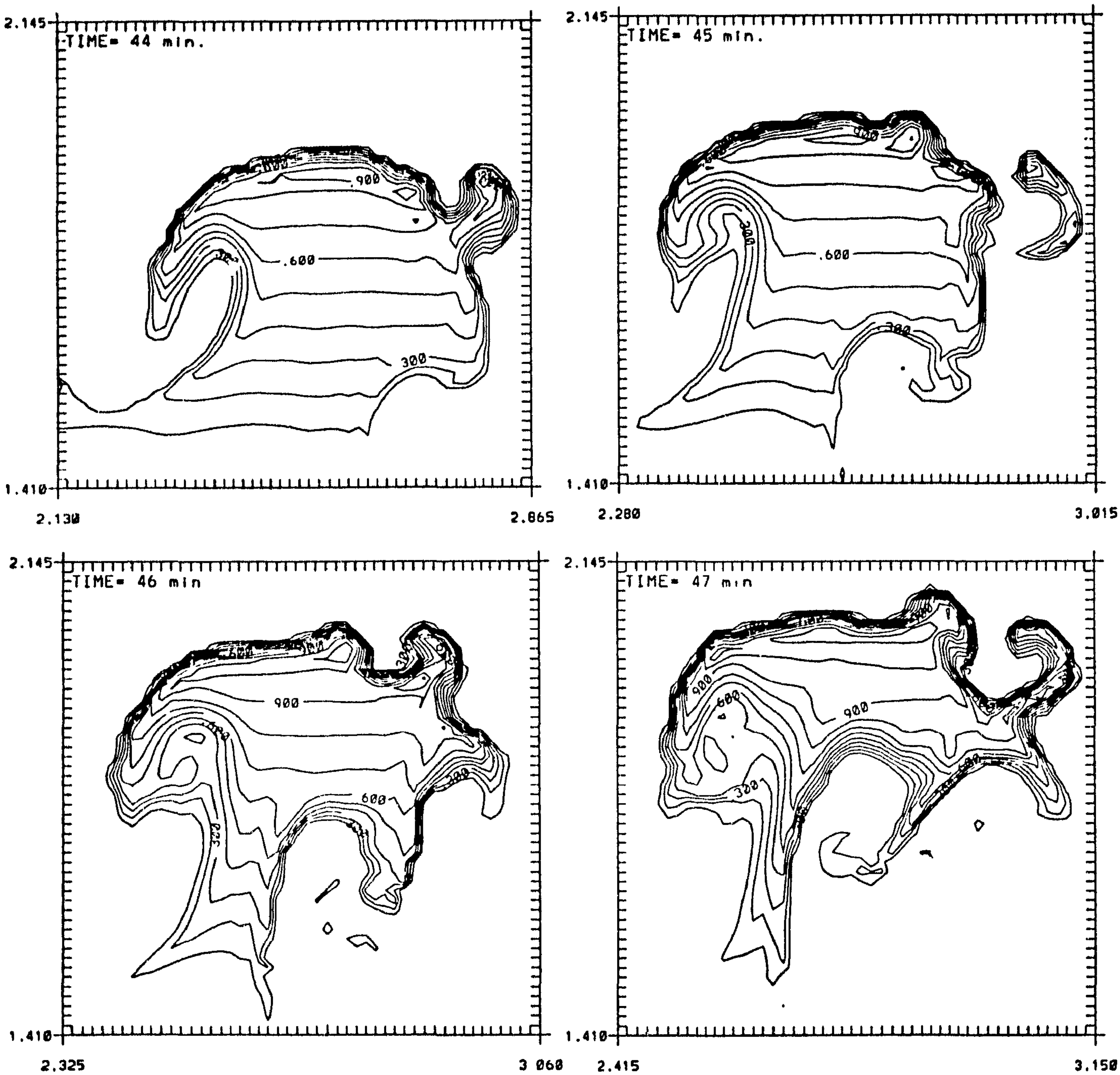

Figure 4: As in figure 3 but for $t = 44, 45, 46, 47 min.$.

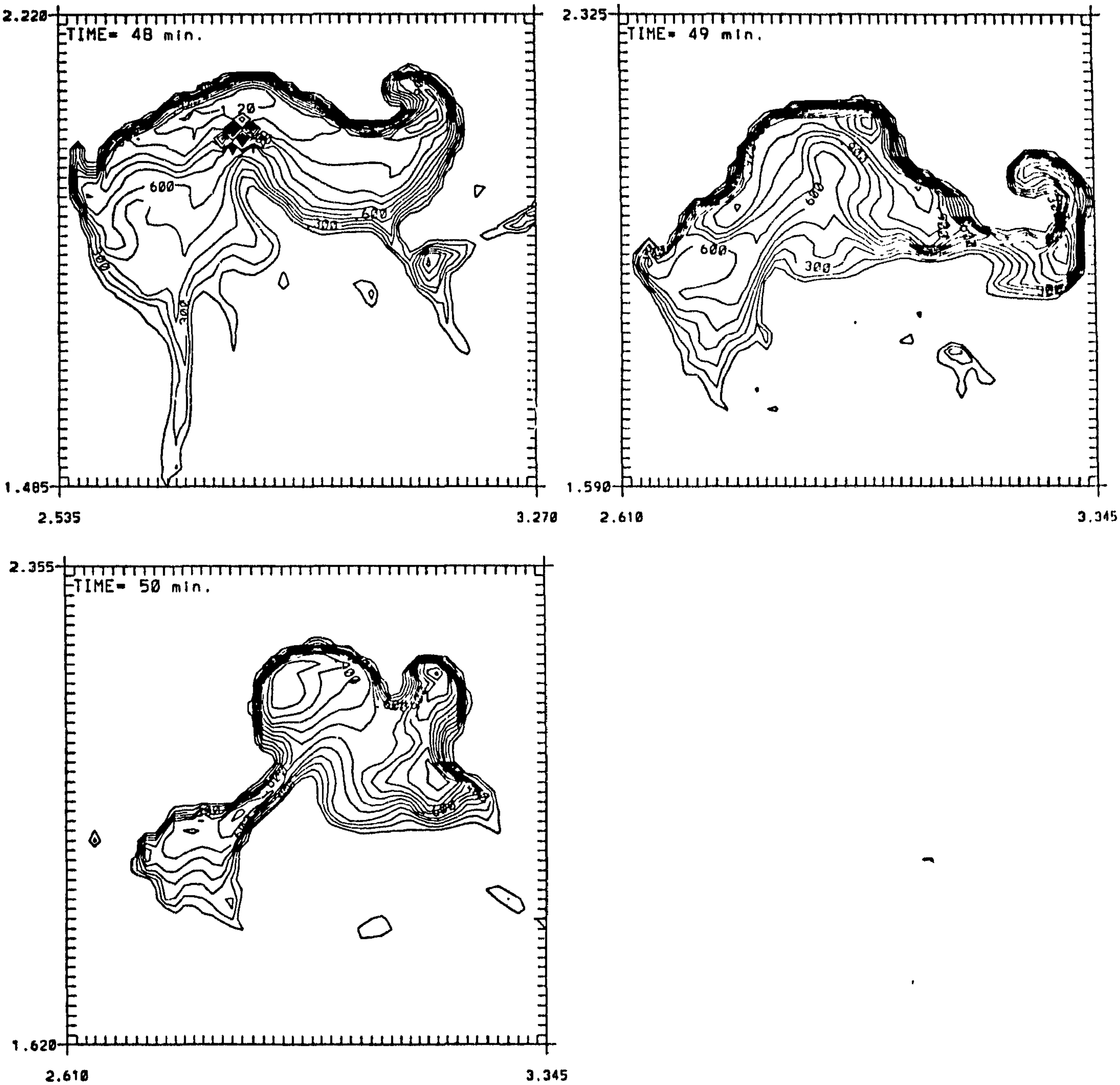

Figure 5: As in figure 3 but for $t = 48, 49, 50min.$.

3.2 Presentation of Microphysical model results

In the next sections, the evolution of the cloud dropsize spectra and its relation to the cloud circulation will be examined using plots of the distribution of the weight functions against b^2 (so called the b^2 distributions) and the corresponding vector velocity fields for a subsection of the simulation domain. An example of the former is given in figure 6 and an example of the latter in figure 7. For clarity, each figure depicts the data at 20×20 grid points, whose exact location relative to the whole cloud can be obtained by referring to figures 3 to 5. A magnified view of the b^2 distribution at a grid point is shown in figure 8 and can be interpreted physically as follows. As explained in section 2.2.2, each EDP is associated with a fixed b^2 and represents those droplets that have experienced the same amount of diffusional growth. Since each cloud dropsize spectrum is a weighed combination of EDP's, the weight function ψ gives the fractional contribution of each EDP to the total spectrum. Consequently, $\psi(b^2)$ describes the distribution of the fraction of droplets in a spectrum that have experienced the same amount of diffusional growth. For example, $\psi(b^2 = 0)$ denotes the fraction of droplets in the spectrum which is newly activated, and $\psi(b_a^2)$ represents the fraction that has grown adiabatically from cloud base.

A vertical bar is also drawn in the figure. The location of the intersection of the vertical bars with the x–axes indicates the adiabatic b–values, b_a. The position of the horizontal mark along this bar is equal to the value

q_c/q_c^a (liquid water mixing ratio divided by the adiabatic liquid water mixing ratio), 0 being at the bottom of the bar and 1 at the top. This ratio serves to identify regions where mixing has occurred and acts as a tracer for diluted grid volumes. A grid volume will be shaded when this ratio $\leq .98$.

The number at the upper right-hand corner of figure 8 is the parameter β, denoting the fraction of the grid volume with cloudy air. The rest of the grid volume being cloud-free. It also serves as an indicator for mixing when $\beta < 1$. However, $\beta = 1$ means that all the grid volume is cloudy, or equivalently, all nuclei are activated, and does not mean that mixing has not occurred. In this case, reference has to be made to the ratio q_c/q_c^a to determine whether mixing has actually taken place at that grid volume. Physically, the situation that $\beta = 1$ and $q_c/q_c^a < 1$ occurs when mixing is followed by lifting and reactivation of all the nuclei in the clear air.

Some errors can be introduced in calculating the adiabatic cloud water mixing ratio as a function of height. In our analysis, this value is calculated by lifting an air parcel with the temperature, pressure, and water vapor mixing ratio of the initial conditions at the surface. The calculated LCL is then $1440m$. In the simulation, however, surface heating occurs and the surface conditions are not horizontally uniform, resulting in a horizontal variation of the LCL of about $30m$ (between $1425m$ and $1455m$). As a consequence, the calculated q_c^a is less than the actual q_c^a where the simulated cloud base is locally lower than $1440m$, resulting in areas where $q_c^a > 1$ on the right portion of the cloud in figure 6. Similarly, the calculated q_c^a exceeds the actual q_c^a where the simulated cloud base is locally higher than $1440m$. Some of the shaded areas near the cloud base in figure 6 may result from this misinterpretation. In our simulation, regions where this error are most likely to occur are near the cloud base where locally the cloud water content is small and a small error in q_c^a can cause a large variation in the ratio q_c/q_c^a. For this reason, we will not analyze the spectra near the cloud base.

It should be mentioned that the b^2 distributions possess certain advantages over the traditionally used dropsize distribution. Figure 9 shows the size distributions $h(r)$, the number of droplets of size r per unit mass of air, covering the same region as in figure 6. By comparing with the b^2 distribution in figure 6, it is evident that the behavior of the two distributions are qualitatively similar. However, only the b^2 distribution can lead to an easy interpretation of the fractions of droplets which have been newly activated or which have undergone adiabatic growth from the cloud base. For this reason, only the b^2 distributions will be presented hereafter.

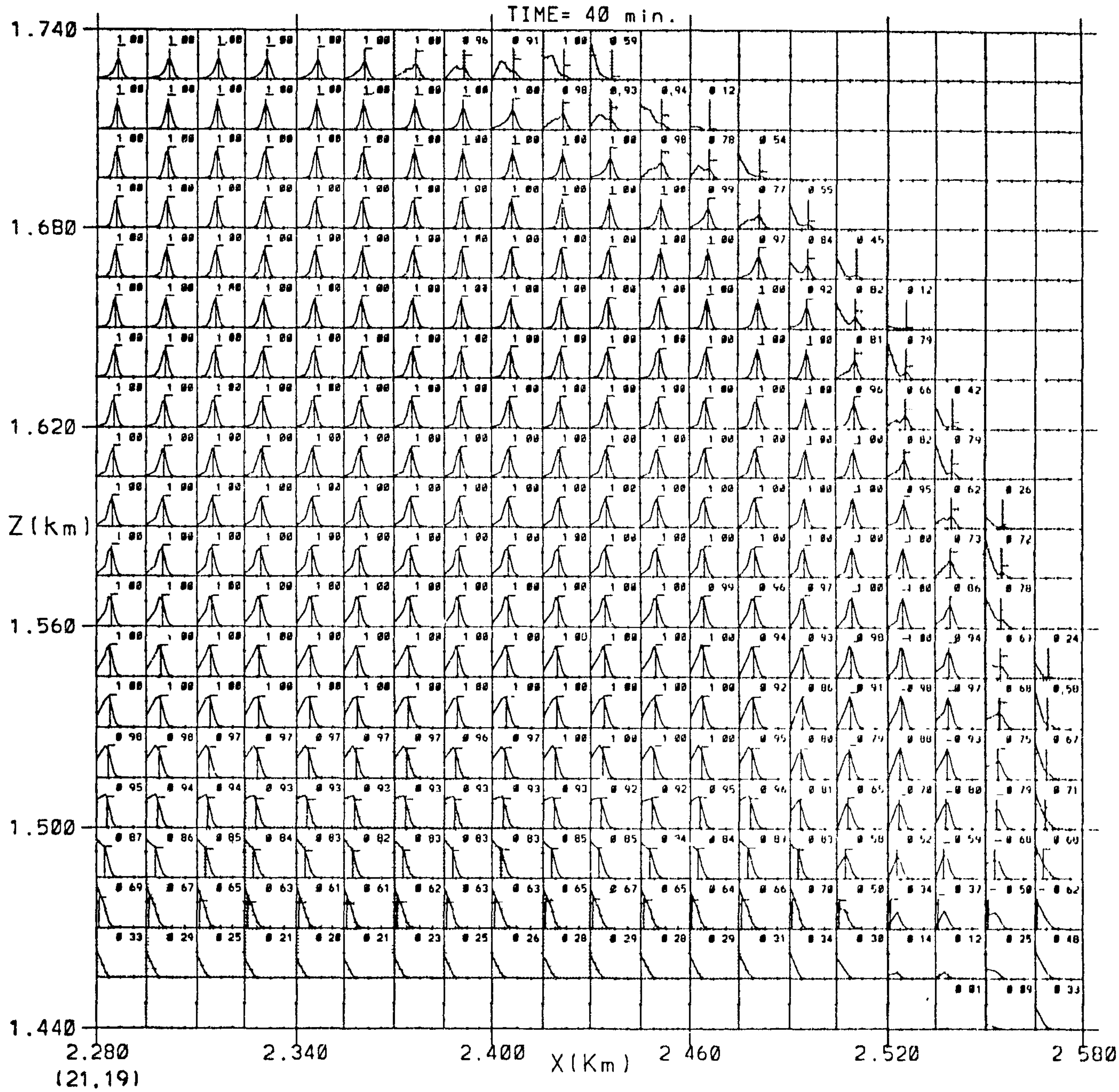

Figure 6: B^2–distributions at $t = 40min.$.

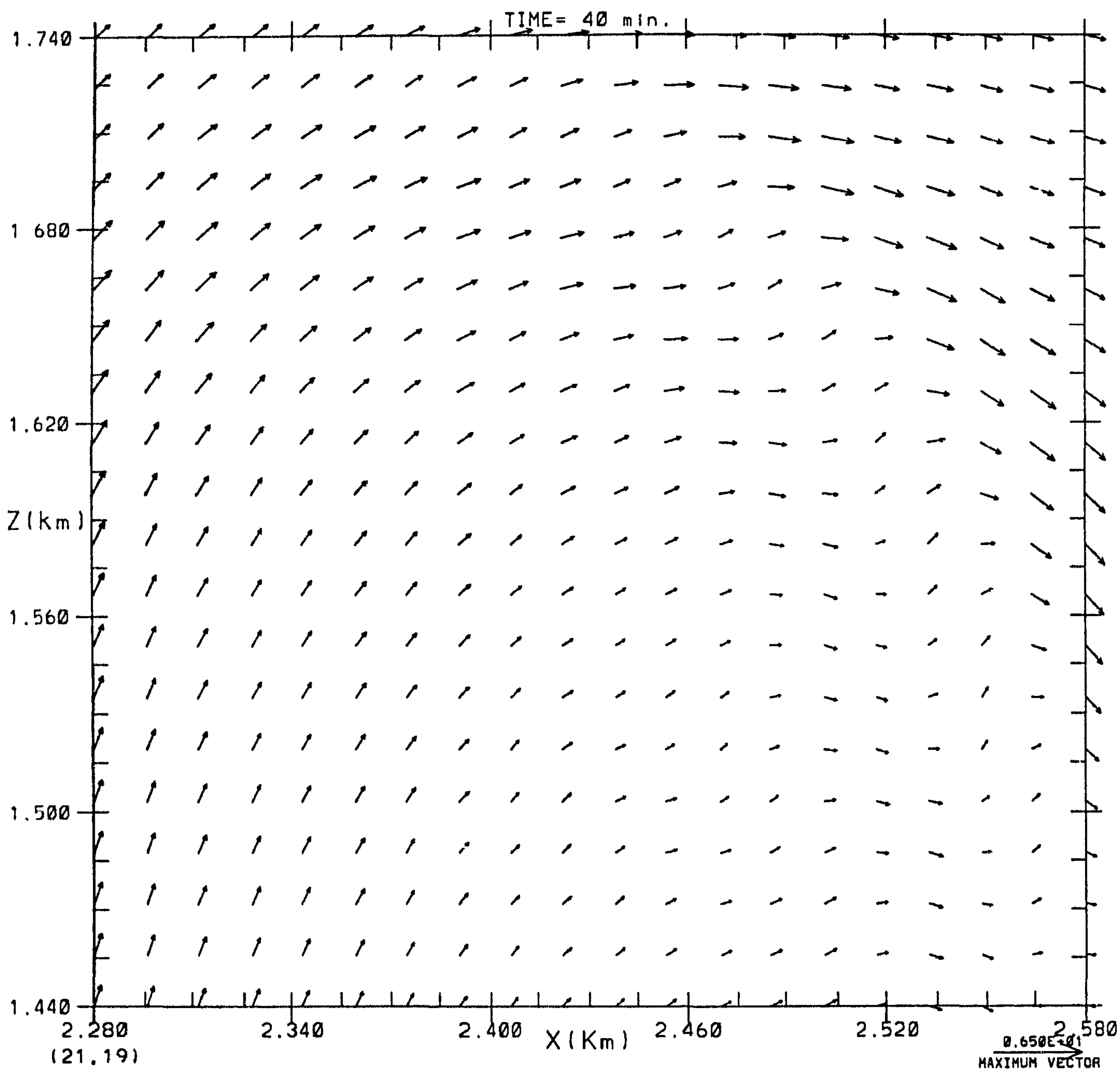

Figure 7: Velocity field for domain of figure 6.

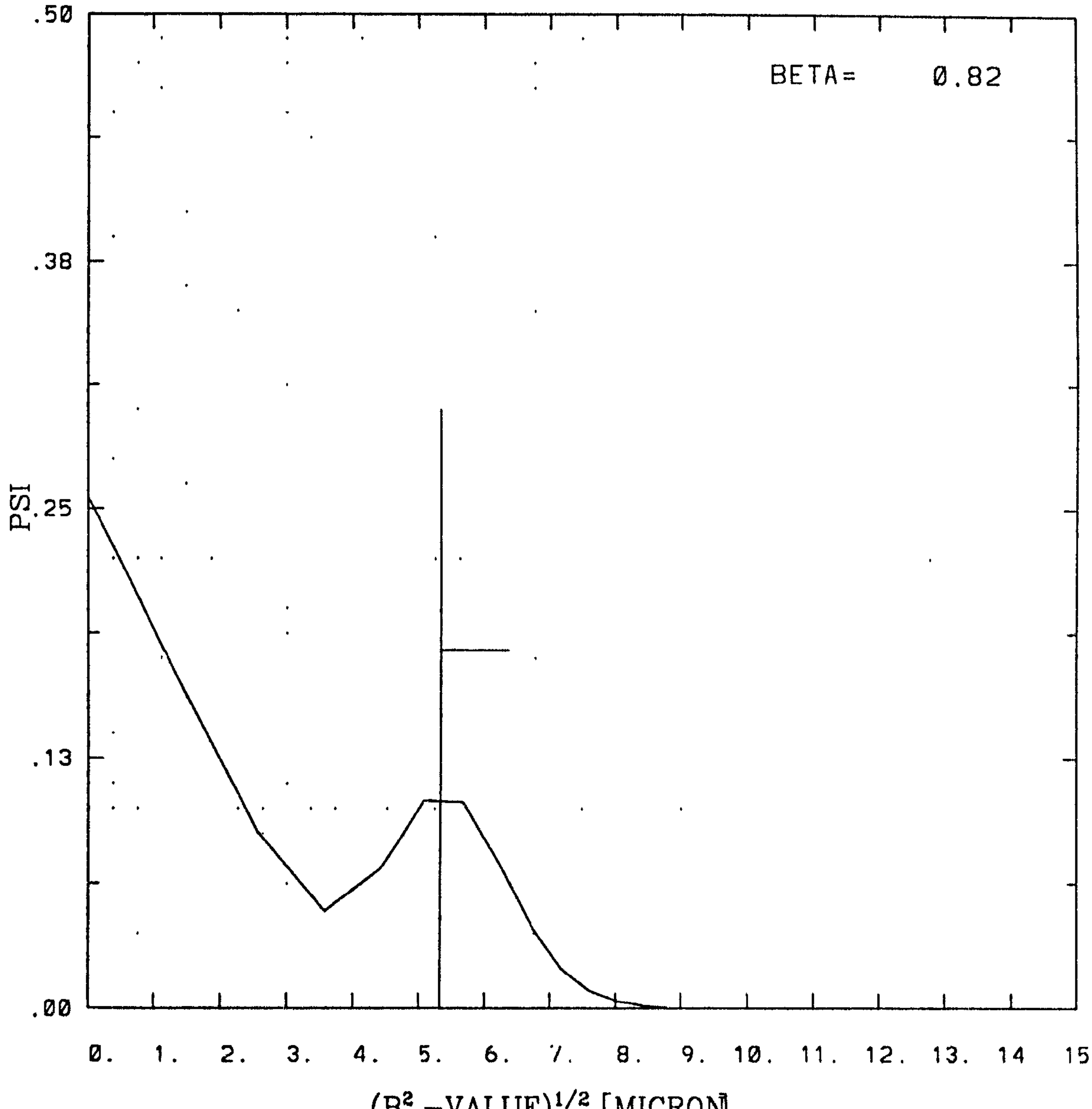

Figure 8: Magnified b^2-distribution from figure 6 (x= 2.505 km, z= 1.65 km).

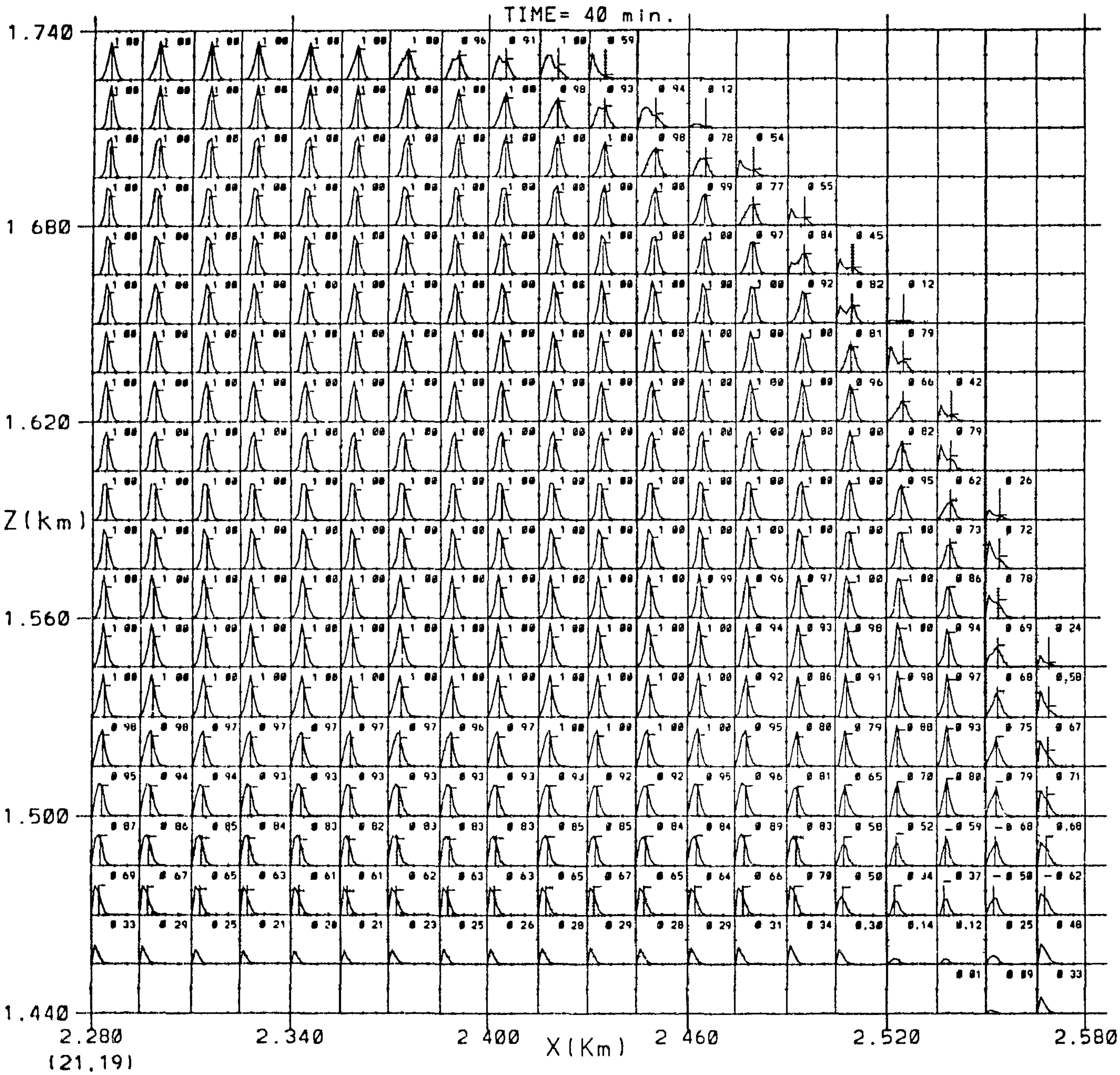

Figure 9: Size distributions at $t = 40min.$.

3.3 Evolution of cloud structure and entrainment sites

Before a detailed discussion of entrainment sites and the effect of mixing on the cloud dropsize distributions, it is necessary to clarify the meaning of the terms entrainment and mixing. The definitions of these terms have changed over the years. At the beginning there was no clear distinction between cloud mixing and cloud entrainment, both referring to the modification of the properties of a certain cloud volume by the exchange of air with the environment. With the need to understand the evolution of the cloud dropsize distributions, research has gradually shifted to the mechanism, the rate and the scale of exchange of air between parcels of differing compositions.

Following the scenario of turbulent mixing advanced by Broadwell and Breidenthal (1982) and Baker et al (1984) (see section 1.1), the term entrainment, or "bulk entrainment" is often used to describe the initial large scale breakup of the interface between cloudy and clear air. Entrainment sites therefore refer to areas where the cloud scale circulation is not parallel to the cloud boundary and where the cloud structure is actively being modified. As a result, the interfacial area increases. Entrainment is followed by the breakup of the entrained volumes into smaller and smaller units, each of which essentially conserves its composition, but the entrained volume as a whole is marked by an increasingly intimate intermingling of cloudy and clear air filaments. The term mixing is often used to denote this process or sometimes applied more specifically to the homogenization of the mixture which occurs when filaments are of the size of the Kolmogorov scale.

In the analysis of observations and in numerical modeling, however, the criteria set out above cannot be used directly to diagnose mixing. The reason is that numerical models and measuring instruments are limited by a finite resolution or sampling rate, which imposes a minimum scale much greater than the Kolmogorov scale. Consequently, it is impossible to determine directly if a diagnosed diluted cloudy volume has in fact a homogeneous or a patchy composition. For practical reasons therefore, mixing can only be diagnosed by a change in certain properties of the cloudy air *averaged* over the smallest grid volume. The property used in this thesis is the ratio q_c/q_c^a.

In the dynamical model, bulk entrainment is directly resolved by the model. The mixing process is dependent on the subgrid-scale turbulence parameterization (see section 2.1). The necessary conditions for mixing can be inferred from the turbulence term in the cloud water equation (10):

$$\nabla \cdot (\overline{\rho} K_m \nabla q_c) = \nabla \overline{\rho} K_m \cdot \nabla q_c + \overline{\rho} K_m \nabla^2 q_c. \qquad (30)$$

It is evident that mixing will be strong in regions where the product of the eddy mixing coefficient, $\overline{\rho} K_m$, and the Laplacian of q_c is large and/or where both the gradient vectors for $\overline{\rho} K_m$ and q_c are large and not perpendicular. These conditions are generally met at the interface between the cloud and the environment and result in a layer $\approx 30m$ thick of partially diluted air which separates the adiabatic cloud core from the environment. If there is strong local wind shears implying non-zero K_m inside the cloud,the area affected by mixing may be greater than the small layer of diluted air at the interface. When the area affected by mixing occurs in a layer more than $30m$ deep, it is referred to as a mixing zone.

We now proceed to study the evolution of the cloud's structure and identify sites where entrainment and mixing occur. We concentrate first on the upshear side, and then on the downshear side of the cloud. For an overall view of the development of the cloud, we display in figures 10 to 20 the time evolution of the vector velocity field for the entire inner domain as well as the $0.1g/kg$ contour for q_c. The area where mixing occurs is shaded. Figure 21 depicts the condensation rate at $47min.$. Figures 22 to 24 display the eddy mixing coefficient fields at 45, 46, and 47 $min.$ respectively. These plots are useful in a detailed discussion of the mixing zones and entrainment sites below.

3.3.1 Upshear side

Entrainment site

Figures 25 to 36 show the b^2–distributions and the vector velocity for the upper upshear portion of the cloud from $t = 42$ to $47min.$ (refer to figs. 12 to 17 for the exact location). The main feature which modifies the shape of this portion of the cloud is a persistent vortex circulation which develops as a result of the interaction between the convective circulation, as it grows beyond the boundary layer, and the initial horizontal wind field (figures 10, 11 and 12). The center of the vortex circulation is marked by an X symbol in the b^2-distribution plots. Note that its position is situated inside the cloud at a relatively constant distance from the cloud boundary (figures 25, 27, 29, 31, 33 and 35). The lower branch of this circulation modifies the cloud structure by creating the indentation which first became visible at $t = 42min.$ (fig. 25). Close to the vortex center, cloudy air is being recirculated. At the entrainment site marked by the indentation, air of different origins is brought into contact with the cloudy air. For example, near (x= 2.22 km, z= 1.65 km) the entrained air comes both from near the cloud top altitude and from the same level further upstream (figures 12 and 26). It must be pointed out that in a two-dimensional simulation, entrainment at the upshear side may be exaggerated as Heymsfield et al. (1978) have suggested that the cloud updraft acts as an obstacle to the horizontal wind which is constrained to flow around the upshear portion of the cloud, thereby protecting that region from entrainment. This air flowing around the cloud, however, cannot be simulated in a two-dimensional model.

The indentation in the cloud deepens from $t = 42min.$ to $t = 45min.$ and a narrow, $\approx 60m$ wide, arm of cloudy air was created (figures 12 to 15). Since this arm is bounded by two cloud-environment interfaces and as mentioned previously, the layer of cloudy air partially diluted by mixing along an interface is $\approx 30m$ wide, the entire arm is partially diluted. This phenomenon would apply to any cloud structure with a width less than $60m$ and is aptly illustrated in the plots at $t = 43, 44, 45min.$ (figures 12 to 15, 27, 29, and 31) where the arm of cloudy air is entirely shaded, the ratio q_c/q_c^a is small with an average value of ≈ 0.4, and β in many grid volumes is significantly below 1 indicating a very patchy composition. The arm structure is completely dissipated at $t = 46min.$ (fig. 33) as a result of mixing and the subsiding motion in the descending branch of the vortex circulation (figs. 28, 30, and 32).

Extension of the mixing zone

The shaded area increases substantially from $t = 42min.$ to $t = 47min.$ (figs. 12 to 17). On the upshear side, the mixing zone propagates upward from the entrainment site and at $t = 47min.$, the region affected by mixing accounts for close to 30% of the total cloud area. The deep penetration of the mixing zone is consistent with a non-zero K_m field inside the cloud, particularly evident directly under the vortex center(marked by an X) in figures 22,23 and 24 at $t = 45, 46, 47min.$.

Erosion of the cloud base

Mixing also affects the erosion of the cloud base. The cloud tilts downshear as it grows and the strong downdrafts which develop on its upshear flank transport subsaturated clear air into the exposed cloud base (figures 14,15 and 16). Strong mixing occurs with a rapid erosion of the exposed area. As the cloud propagates with the flow and as the cloud base is being eroded, the amount of moist air originating in the boundary layer reaching the cloud base decreases. At $t = 47min.$ (fig. 17), the cloud is entirely encircled by air with low relative humidity from above the boundary layer.

3.3.2 Downshear side

Entrainment sites

As mentioned earlier, the structure on the downshear side of the cloud is more complex than the upshear side. Here, the main circulation features which modify the cloud structure and lead to entrainment, are the periodic formation of bubble like structures near the cloud top, the accompanying penetrative downdrafts, as well as vortices which form near the middle and lower portion of the downshear edge.

The velocity field at $t = 40, 42, 43min.$ (figures 11,12 and 13) indicates that just inside the downshear boundary of the cloud, the air rises before descending along the exterior of the cloud edge. At $t = 43min.$ this rising motion intensifies, leading to the formation of a bubble–like structure around x= 2.805 km, z> 1.785 km at $t = 44min.$ (figs. 37 and 38). Klaassen and Clark (1985) obtained similar structures near the top of their simulated cloud. They attributed their formation to the baroclinic production of vorticity at the cloud environment surface arising from horizontal buoyancy gradients.

The formation of the bubble–like structures are accompanied by the development of slanted penetrative downdrafts located in an immediate upwind position. Figs. 39 and 40 show that at $t = 45min.$, the descending air associated with these downdrafts undergoes acceleration and separates the bubble from the main portion of the cloud. The bubble then dissipates rapidly once it is encircled by clear air. The exact mechanism for the formation of the downdrafts is unknown. Evaporative cooling caused by mixing and penetration of the cloud into a stable environment can create a layer of negatively buoyant air at the cloud top which may play a role in downdraft formation. In the simulation of Klaassen and Clark (1985) penetrative downdrafts still formed when the eddy mixing coefficient was set to zero indicating that mixing played a secondary role in their formation. The scenarios of bubble formation, subsequent separation from the main cloud and eventual dissipation repeats itself at a similar location along the cloud's upper downshear boundary until the cloud decays (see figs. 41,42, and 56).

Another significant feature is the descending branch of the moist convective cell clearly visible along the downshear flank at 40, 42, and 43 min. (figures 11,12 and 13). At $t = 44min.$ (figs. 14 and 44), this downdraft interacts with the main updraft to form a vortex circulation in the lower portion of the cloud. The vortex contributes to the erosion of the cloud base and the formation of a mixing zone on the lower downshear side (figure 43). One minute later, in response to the descending branch of the vortex, a diluted arm of cloudy air becomes visible from x= 2.73 to 2.85 km (figs. 15 and 46). At $t = 46min.$ (figs. 16 and 47- 50), the lower vortex circulation is less defined and another vortex has developed higher in the cloud at z = 1.65 km, again creating a mixing zone and an arm of cloudy air. At $t = 47min.$ (figs. 52 and 53) a spiral has formed as part of the diluted arm is being uplifted creating an area with small values of q_c/q_c^a and large values of β. Note that by this time, only $\approx$ 30% of cloud area, associated mostly with the downshear cloud core, has not been affected by mixing (fig. 17). After $t = 47min.$ (fig. 17), the main updraft which originates from the boundary layer no longer separates the convective circulations of the upshear and the downshear sides. The reason is that the cloud circulation is no longer attached to the boundary layer convective circulation. As a result, clear air from the upshear side is observed to flow along the base of the cloud, and large areas of diluted cloudy air on the upshear side propagate toward the downshear side (note the region from x= 2.82 to 2.97 km and z= 1.86 to 2.04 km in figs. 54,55,56,and 57). After $t = 49min.$, almost the entire cloud is partially diluted (figures 58 to 63); most of the diluted cloudy air originates from the mixing zone situated on the upshear flank of the cloud.

Extension of mixing zones

The circulation on the downshear side did not permit the creation of any deep mixing zones. Instead, the shape of the cloud is continuously being deformed and narrow structures like the bubbles at the cloud top and the arms in the lower part of the cloud are formed. These narrow structures are subject to severe mixing and dissipate rapidly because of the high interfacial area. As a result, total evaporation of cloud droplets often occurs on the downshear side. Figure 21 shows the condensation rate at $t = 47min$. Note that the area coverage and the intensity of evaporation (negative areas) are much larger on the downshear side than the upshear side. It is evident that the circulation here did not permit the diluted cloudy air to be recycled inside the cloud structure, a situation quite different from that of the upshear side with the presence of a long-lasting vortex centered inside the cloud.

3.4 Evolution of cloud dropsize distributions

Some observations of the characteristics of cloud dropsize distribution can be made. In regions not previously affected by mixing (e.g. the non-shaded areas in fig. 51), the b^2 distributions are narrow and centered around the adiabatic b^2-value(b_a). These droplets have therefore essentially undergone adiabatic growth from the cloud base. At the cloud environment interface and in mixing zones the b^2 distributions indicate significant differences. In our discussion below, we shall focus on the time period $t < 18min$. because the cloud is completely diluted at later times and a direct comparison of the spectra in mixing and unmixed zones cannot be made. Also the most extensive long-lasting mixing zone is situated on the upshear side of the cloud. We shall concentrate our analysis in this region.

The first characteristic noted is the presence of bimodal spectra in areas where mixing has occurred (see e.g. the shaded areas in fig. 31). These spectra can be found both within the cloud–environment interface (e.g. x= 2.43 km, z= 1.935 km) and in mixing zones (e.g. x= 2.37 km, z= 1.80 km). Two modes can be observed; the primary mode is centered around b_a and the secondary mode centered around an intermediate value between 0 and b_a. In the literature, bimodal spectra are often attributed to activation of new droplets when the supersaturation in an air parcel exceeds the peak value experienced near cloud base (Paluch and Knight, 1984). In this study, however, they are a direct consequence of the assumption of extreme inhomogeneous mixing described in section 2.2.1. As an example, consider an initially unmixed cloudy grid volume with a droplet concentration of $1000cm^{-3}$ undergoing mixing with clear air. Let us suppose that enough mixing occurs to reduce the average concentration of droplets in the grid volume by half, to $500cm^{-3}$. Because of extreme inhomogeneous mixing, the microphysical model interprets this to mean that 50% of the grid volume is composed of clear air and 50% of cloudy air having a droplet concentration equal to that of the initially unmixed volume. If lifting follows so that $\Delta q > 0$, activation of the nuclei in clear air and diffusional growth will occur in the manner described in section 2.2.2. If enough lifting takes place so that all the nuclei were activated, the average droplet concentration in the grid volume will again reach the local concentration in the cloudy air. The newly activated nuclei accounts for the secondary mode of the distributions.

To clarify the above description, we shall consider the b^2 distributions along a loop A, B, C, and D within the upshear mixing zone in figure 31. This path approximates a cycle around the vortex center. Starting at point A and travelling horizontally towards point B we can see that β and the ratio q_c/q_c^a decrease. On passing point B, these values increase and are close to 1 at the right boundary of the mixing zone. Similar variation can be found along any horizontal path through the mixing zone. The fact that the minimum values for q_c/q_c^a and β occurs at some distance from the right cloud edge signifies that mixing originates and propagates from the entrainment site situated at a lower level (near x= 2.43 km and z= 1 755 km).

Severe mixing, marked by a low ratio of q_c/q_c^a, is taking place at B and reduces the magnitude of the primary mode of the distribution when averaged over the grid volume. High values for $\psi(b^2 = 0)$ and β can be detected from B to C. This part of the loop lies within a zone of uplifting and therefore new nucleation. Close to point C, β increases to 1 as all nuclei are activated. The ratio q_c/q_c^a also increases because of condensation and the increasing distance from the entrainment site. It is noted that the secondary mode grows towards larger b values and the primary mode increases in amplitude.

Little change in the distributions is detected from point C to point D. This segment of the loop is located far from the entrainment site with little lifting and small horizontal variation in the amount of mixing. The processes taking place from D to A is just the reverse of those from B to C, namely evaporation and the approach toward the entrainment site with an increase in the amount of mixing. Consequently, the primary mode decreases in amplitude while the secondary mode grows towards smaller b values.

Bimodal spectra are thus created when mixed air is being lifted. The origin of the bimodal spectra is located to the right of the vortex center. The vortex circulation then recirculates these spectra throughout the mixing zone.

Bimodal spectra are also present elsewhere in the cloud where a similar scenario occurs. An example for this is the spectra in the downshear mixing zone in figures 47 (x= 2.91 to 3.0 km; z= 1.8 to 1.86 km)) and 52 (x= 2.76 to 2.85 km, z= 1.83 to 1.89 km). However, not many bimodal spectra can be found on the downshear side because the mixing zones are less extensive there.

From $t = 48 min.$ onward (figs. 54 to 63), the b^2 distributions are more varied and complex in shape. Most of them are bimodal, but with a few monomodal distributions centered on b_a (fig. 60 x= 3.075 to 3.12 km; z= 1.98 to 2.07 km). Some monomodal distributions centered on a b^2 value between 0 and b_a can be seen on the far right in figure 54 (x= 2.76 to 2.85 km; z= 1.935 km). These result from the lifting of an area which had undergone very severe mixing. A few trimodal distributions can also be found. Examples are the spectra near the cloud top in figure 59 (x= 2.85 to 3.03 km; z= 2.16 km) or the spectra in the middle left of figure 61 (x= 2.76 to 2.85 km; z= 1.935 km). These spectra result from the same process of extreme inhomogeneous mixing followed by lifting but occur in cloudy air containing initially bimodal instead of monomodal distributions.

Another parameter useful in characterizing the distribution is the average radius $\overline{R}$ displayed in figs. 64 and 65, which can be readily calculated from the b^2 distribution. In the unmixed cloud core, the average radius increases with height and attains its maximum value near the cloud top (figure 64 at $t = 44min.$). Below the cloud top the gradient of radius decreases with height since smaller droplets increase in size faster than bigger ones. Horizontally, $\overline{R}$ remains nearly uniform. The small variations in unmixed zones is attributable to the variation in the cloud base altitude.

The maximum $\overline{R}$ throughout the simulation is $6.71\mu m$ and occurs at $t = 49min.$. The corresponding grid volume is highlighted in figure 59. Unsurprisingly it is situated near the cloud top in a small unmixed zone and is therefore monomodal.

In mixing zones, the variations in the average radius is more complex. $\overline{R}$ decreases as a result of evaporation and activation where the diluted parcels are being lifted. As is indicated in figure 64, at $t = 46min.$ $\overline{R}$ in the upshear mixing zone is smaller than that of the unmixed adiabatic cloud core at the same level.

The time evolution of the standard deviation of the distribution σ from $t = 43min.$ to $t = 50min.$ is depicted in figures 66 and 67. At $t = 43$ and $44min.$ σ is relatively uniform and is $\approx 1\mu m$ in the adiabatic cloud core.

Where mixing has occurred, either in mixing zones or at the cloud environment interface, $\sigma > 1\mu m$. The broadest spectra occur near the cloud top. They are bimodal with high $\psi(b^2 = 0)$ values implying a high concentration of small droplets. The maximum value for σ throughout the simulation occurs at $t = 50min.$. Its value is $2.8\mu m$ and the corresponding grid volume is highlighted in figure 63.

Figure 68 shows contour lines of R_g, the equivalent radius of the mean mass of the mass density function(see Rogers and Yau 1989, p. 140 for definition), at $t = 46min.$. The mass density function gives emphasis to large droplets, and is used here in an attempt to evaluate the evolution of the primary mode of the cloud droplet spectra in mixed regions. The values of R_g do not vary much in all of the cloud; with a low value of $\approx 5.5\mu m$ and a high value of $7.6\mu m$. The maximum values are located at the cloud base. They then decrease in the first $\approx 120m$ and increase thereafter up to the cloud top. The R_g of the nucleation spectrum is $7.46\mu m$, a value which is found at the cloud base and in certain areas where severe mixing followed by lifting results in spectra similar to those found at the cloud base.

The physical explanation for the distribution of R_g is as follows. At nucleation, the vast majority of droplets have a radius of $1\mu m$ and they make a negligible contribution to the mean mass of the mass distribution, which is mostly influenced by droplets $> 12\mu m$ even though their concentrations are very low($\approx 10^{-2}mg^{-1}$). As lifting and nucleation proceeds, the total concentration of the droplets increases and the $1\mu m$ droplets are growing to larger sizes. When these droplets reach the sizes of $3, 4, 5\mu m$, they begin to contribute to the mean mass of the mass distribution. R_g therefore initially decreases with altitude. However, at a height $> 120m$ above the cloud base, the concentration of droplets $> 6\mu m$ is high enough to cause an increase in R_g with altitude.

It should be pointed out that in certain areas within the mixing zones, a process opposite to that just described occurs. Evaporation resulting from mixing causes an increase in R_g(fig. 68 x= 2.52 to 2.565, z=1.71 to 1.92). To determine if this increase is also due to an increase in the concentration of larger droplets, we plotted in figures 69, 70, 71 and 72 the horizontal variation of $R_g, \overline{R}, \sigma, q_c/q_c^a$ and the total concentration of droplets $\geq 12\mu m$(c curve) at different altitudes at $t = 46min$. It can be seen that many features described above are clearly shown in these figures. For example, the r curve($\overline{R}$) is well correlated with the q-curve(q_c/q_c^a), and the s curve(σ) is negatively correlated with it. The m-curve(R_g) does not vary much but is often slightly higher in regions of low q_c/q_c^a (see the curves at 1800, 1845m). Furthermore, the c-curve is well correlated with the q curve, but not with the m-curve. This eliminates the possibility that the increase in R_g is caused by an increase in the concentration of large droplets. We should emphasize that the concentration of the largest droplets in mixing zones was never higher than that in the adiabatic cloud core at the same altitude.

4 Conclusion

In this thesis we performed a numerical simulation of the development of a small non- precipitating continental cumulus cloud in a sheared environment. A dynamical cloud model is used in conjunction with a microphysical model to predict the evolution of cloud dropsize distributions and to yield answers to the following questions:

1. How and where does entrainment and mixing occur?
2. Is there any differences between upshear and downshear sides of cloud in terms of entrainment and mixing?
3. How are cloud dropsize distributions modified by extreme inhomogeneous mixing?

A detailed analysis of the modeling results allow us to draw the following conclusions:

1. The vortex circulations and penetrative downdrafts serve to deform the shape of the cloud and lead to entrainment of clear air into the cloud structure. The entrained air has its origin both from the cloud top level and from the sides.
2. On the upshear side of the cloud, the convective circulation is dominated by a long–lasting vortex with its center situated inside the cloud

boundary. This circulation initiates entrainment and results in the creation of a mixing zone which propagates from the entrainment site to cover more and more of the cloud volume.

On the downshear side, no deep mixing zones appear before $t = 48min.$. The circulation is dominated by subsiding motion, a high turbulence level, multiple vortices with centers outside the cloud boundary, penetrative downdrafts, and periodically forming bubble like structures. In comparison with the picture on the upshear side, we observe a more fragmented cloud structure and often total dissipation of the cloudy air rather than partial dilution. Non-diluted cloudy air exists on the downshear side for a longer time.

3. Extreme inhomogeneous mixing leads to multimodal distributions. This results when the mixed air is lifted and condensation nuclei present in clear air filaments in the grid volumes are activated. Bimodal spectra are commonly found at the cloud-environment interface and in mixing zones on the upshear side of the cloud. The effects of mixing on the droplet size spectra are assessed by comparing the distributions in undiluted cores with those in mixing zones. It was found that mixing results in a smaller average radius, the largest $\overline{R}$ being found near the cloud top in non-diluted cloud regions, a larger standard deviations with the largest σ near cloud top in diluted regions, and larger values of the equivalent radius of the mean mass of the mass distribution func-

tion in certain areas. However, it was shown that these larger values in R_g do not imply an increase in the concentration of large droplets.

This thesis represents a first effort to investigate the effects of mixing on the evolution of the cloud dropsize spectra. It is recognized that some of the underlying assumptions may limit the generality of the results presented here. In particular, the assumption of extreme inhomogeneous mixing and its consequence of a constant local concentration, can exert important influences on spectral evolution. As was mentioned in BG, the assumption is especially questionable for old cloud volumes where there might have been enough time to complete the mixing process. In addition, the imposition of a constant local concentration makes it impossible for Baker et al.'s (1980) or Telford and Chai's (1980) theoretical scenarios of production of large droplets to occur.

Another assumption that requires further study is the partition between homogeneous and inhomogeneous evaporation for diluted grid volumes in the microphysical model. In the experiment analyzed in the thesis, the parameter δ is set to β. However, additional experiments performed, with $\delta = 0$ and $\delta = 1$ have shown that the way of partitioning does have a quantitative impact on spectral evolution, so that a more rigorous formulation would be necessary.

Finally, the microphysical model represents a first attempt to describe the sub-grid scale structure of the composition of the air in the grid volume by dividing it into cloudy and cloud-free portions. For consistency, similar treatments need to be extended to describe the effects of the sub grid scale structures of thermodynamic variables like temperature or relative humidity on spectral evolution.

References

[1] Arakawa, A., 1966: Computational design for long-term numerical integration of the equations of fluid motions: Two dimensional incompressible flow. *J. Comput. Phys.*, **1**, 119-143.

[2] Austin, P. H., M. B. Baker, A. Blyth and J. B. Jensen, 1985: Small scale variability in warm continental cumulus clouds. *J. Atmos. Sci.*, **42**, 1123–1138.

[3] Baker, M. B., R. G. Corbin and J. Latham, 1980: The influence of entrainment on the evolution of cloud–droplet spectra: I, a model of inhomogeneous mixing. *Quart. J. R. Met. Soc.* , **106**, 581–598.

[4] Baker, M. B., R. E. Breidenthal, T. W. Choularton and J. Latham, 1984: The effects of turbulent mixing in clouds. *J. Atmos. Sci.*,**41**, 299–304.

[5] Blyth, A. M., and J. Latham, 1985: An airborne study of vertical structure and microphysical variability within a small cumulus. *Quart. J. R. Met. Soc.* , **111**, 773–792.

[6] Bower, K. N., T. W. Choularton, 1988: The effects of entrainment on the growth of droplets in continental cumulus clouds. *Quart. J. R. Met. Soc.* , **114**, 1411–1431.

[7] Brenguier, J. L., 1990: Parmeterization of the condensation process in a small nonprecipitating cumuli. *J. Atmos. Sci.*, **47**, 1127–1148.

[8] Brenguier, J. L., 1991: Parmeterization of the condensation process: A theoretical approach. *J. Atmos. Sci.*, **48**, 264–282.

[9] Brenguier, J. L., and W. W. Grabowski, 1992: Cumulus entrainment and cloud droplet spectra: A numerical model within a two–dimensional dynamical framework. *J. Atmos. Sci.*, (*accepted for publication*).

[10] Broadwell, J. E., and R. E. Breidenthal, 1982: A simple model of mixing and chemical reaction in a turbulent shear layer. *J. Fluid Mech.*, **125**, 397–410.

[11] Clark, T. L., 1977: A small-scale dynamic model using a terrain following coordinate transformation. *J. Comput. Phys.*, **24**, 186-215.

[12] Clark, T. L., 1979: Numerical simulations with a three dimensional cloud model: Lateral boundary condition experiments and multicellular severe storm simulations., *J. Atmos. Sci.*, **36**, 2191-2215.

[13] Clark, T. L., and R. D. Farley, 1984: Severe downslope windstorm calculations in two and three spatial dimensions using anelastic interactive grid nesting: A possible mechanism for gustiness. *J. Atmos. Sci.*, **41**, 329-350.

[14] Cooper, W. A., 1989: Effects of variable droplet growth histories on droplet size distributions. Part I: Theory. *J. Atmos. Sci.*, **46**, 1301-1311.

[15] Fitzgerald, J. W. , 1974: Effect of aerosol composition on cloud droplet size distribution: A numerical study. *J. Atmos Sci.*,**31**, 1358-1367.

[16] Grabowski, W. W., 1989: Numerical experiments on the dynamics of the cloud-environment interface: Small cumulus in a shear free environment. *J. Atmos. Sci.*, **46**, 3513-3541.

[17] Heymsfield, A. J., P. N. Johnson and J. E. Dye, 1978: Observations of moist adiabatic ascent in northeast Colorado cumulus congestus clouds. *J. Atmos. Sci.*, **35**, 1689-1703.

[18] Hicks, E., C. Pontikis and A. Rigaud, 1990: Entrainment and mixing processes as related to droplet growth in warm midlatitude and tropical clouds. *J. Atmos Sci.*, **47**, 1589-1618.

[19] Hill, T. A., and T. W. Choularton, 1986. A model of the development of the droplets spectrum in a growing cumulus turret. *Quart. J. Roy Meteor. Soc.*, **112**, 531-551

[20] Jensen, J. B., and M. B. Baker, 1989: A simple model for droplet spectral evolution during turbulent mixing. *J. Atmos. Sci.*, **46**, 2812-2829.

[21] Johnson, D. B., 1982: The role of giant and ultragiant aerosol particles in warm rain initiation. *J. Atmos. Sci.*, **39**, 448-460.

[22] Klaassen, G. P., and T. L. Clark, 1985: Dynamics of the cloud–environment interface and entrainment in small cumuli: Two–dimensional simulations in the absence of ambient shear. *J. Atmos. Sci.*, **42**, 2621–2642

[23] Latham, J., and R. L. Reed, 1977: Laboratory studies of the effects of mixing on the evolution of cloud droplet spectra. *Quart. J. R. Met. Soc.*, **103**, 297–306

[24] Lilly, D. K., 1962: On the numerical simulation of buoyant convection. *Tellus*, **14**, 148–172.

[25] Lilly, D. K., 1965: On the computational stability of numerical solutions of time dependent nonlinear geophysical fluid dynamics problems. *Mon. Wea. Rev.*, **93**, 11–26.

[26] Manton, M. J., 1979: On the broadening of a droplet distribution by turbulence near cloud base. *Quart. J. R. Met. Soc.*, **105**, 899–914.

[27] Paluch, I. R., 1971: A model for cloud droplet growth by condensation in an inhomogeneous medium. *J. Atmos. Sci.*, **28**, 629–639.

[28] Paluch, I. R., and C. A. Knight, 1984: Mixing and evolution of cloud droplet size spectra in a vigorous continental cumulus. *J. Atmos. Sci.*, **41**, 1801–1815.

[29] Paluch, I. R., and D. G. Baumgardner, 1989: Entrainment and fine scale mixing in continental convective clouds. *J. Atmos. Sci.*, **46**, 261–278.

[30] Politovich, M. K., and W. A. Cooper, 1988: Variability of the supersaturation in cumulus clouds. *J. Atmos. Sci.*, **45**, 1651–1664.

[31] Pruppacher, H. R., and J. D. Klett, 1978: *Microphysics of Clouds and Precipitation*, D. Reidel, p. 422.

[32] Reuter, G. W., 1986: A historical review of cumulus entrainment studies. *Bull. Amer. Meteor. Soc.*, **67**, 151–154.

[33] Rogers, R. R., and M. K. Yau, 1988: *A Short Course in Cloud Physics* Third Edition, Pergamon Press , p. 112.

[34] Smagorinsky, J., 1963: General circulation experiments with the primitive equations. I. The basic experiment. *Mon. Wea. Rev.*, **91**, 99-164.

[35] Smolarkiewicz, P. K., 1984: A fully multidimensional positive definite advection transport algorithm with small implicit diffusion. *J. Comput. Phys.*, **54**, 325-362.

[36] Smolarkiewicz, P. K., and W. W. Grabowski, 1990: The multidimensional positive definite advection transport algorithm: Nonoscillatory option. *J. Comput. Phys.*, **86**, 355-375.

[37] Squires, P., 1958: Penetrative downdraughts in cumuli. *Tellus*, **10**, 381-385.

[38] Srivastava, R. C., 1989: Growth of cloud droplets by condensation: A criticism of currently accepted theory and a new approach. *J. Atmos. Sci.*, **46**, 869-887.

[39] Stommel, H., 1947: Entrainment of air into a cumulus cloud. *J. Meteor.*, **4**, 91-94.

[40] Telford, J. W., and P. B. Wagner, 1980: The dynamic and liquid water structure of the small cumulus as determined from its environment. *Pure Appl. Geophys.*, **118**, 935-952.

[41] Telford, J. W., and S. K. Chai, 1980: A new aspect of condensation theory. *Pure Appl. Geophys.*, **118**, 720-742.

[42] Warner, J., 1969a: The microstructure of cumulus cloud. Part I: General features of the droplet spectrum. *J. Atmos. Sci.*, **26**, 1049-1059.

[43] Warner, J., 1969b: The microstructure of cumulus cloud. Part II: The effect on cloud droplet size distribution of the cloud nucleus spectrum and updraft velocity. *J. Atmos. Sci.*, **26**, 1272-1282.

[44] Warner, J., 1973a: The microstructure of cumulus cloud. Part IV: The effect on the droplet spectrum of mixing between cloud and environment. *J. Atmos. Sci.*, **30**, 256-261.

Figures

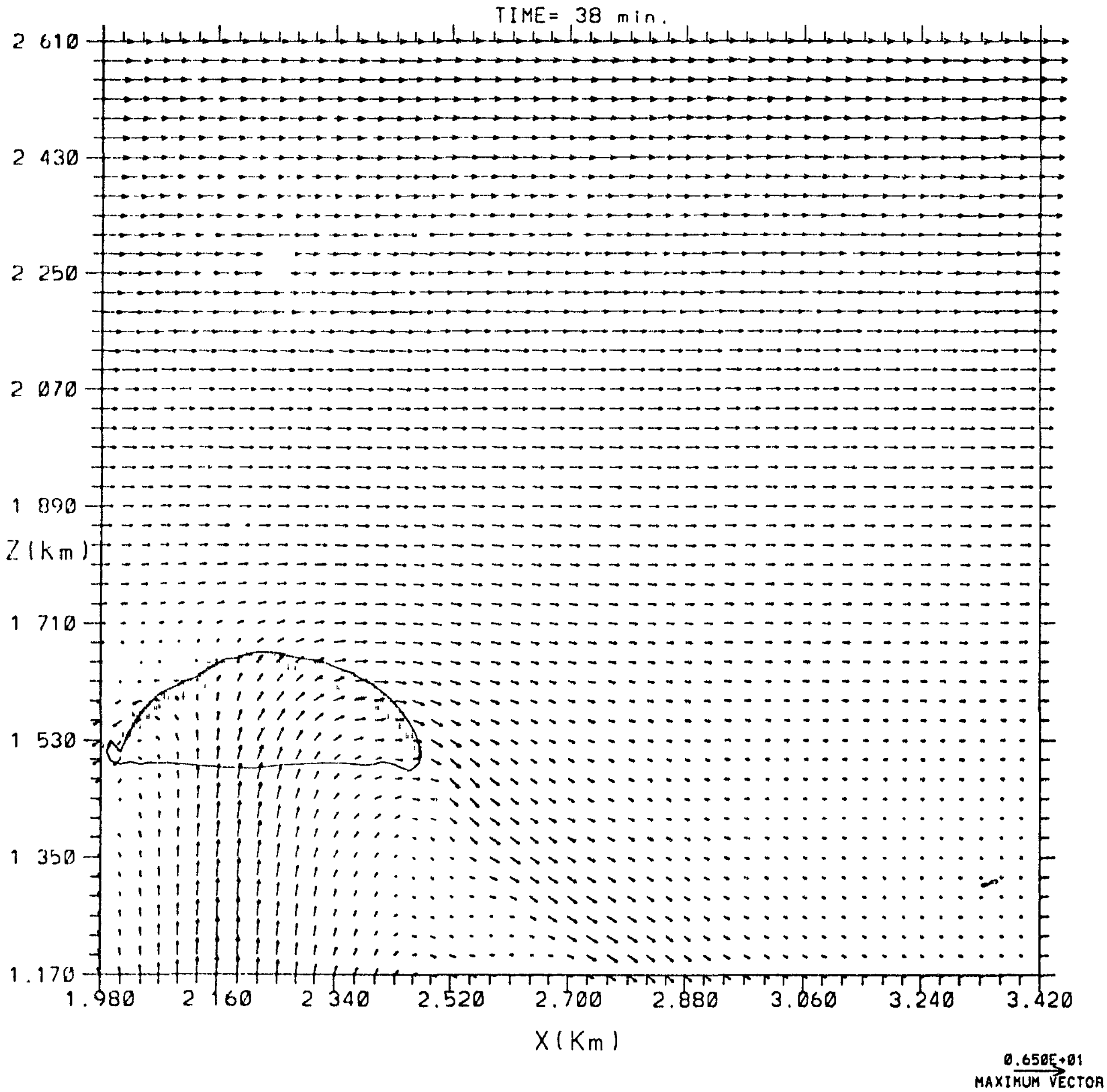

Figure 10: Velocity vectors for entire inner domain at $t = 38min.$, solid line is the $0.1g/kg$ contour line of q_c, shaded area is where $q_c/q_c^a < .98$.

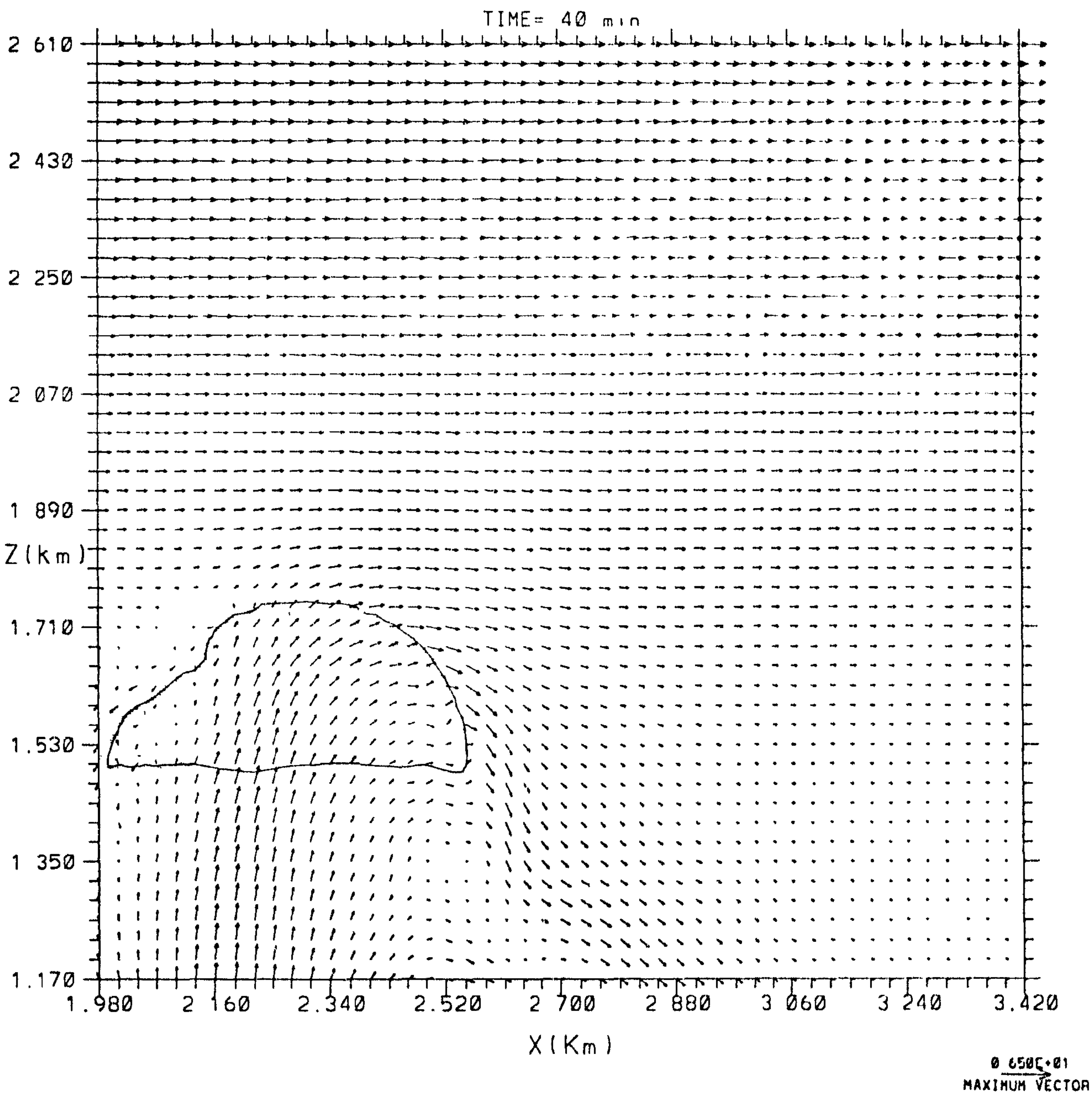

Figure 11: As in figure 10 but for $t = 40min$..

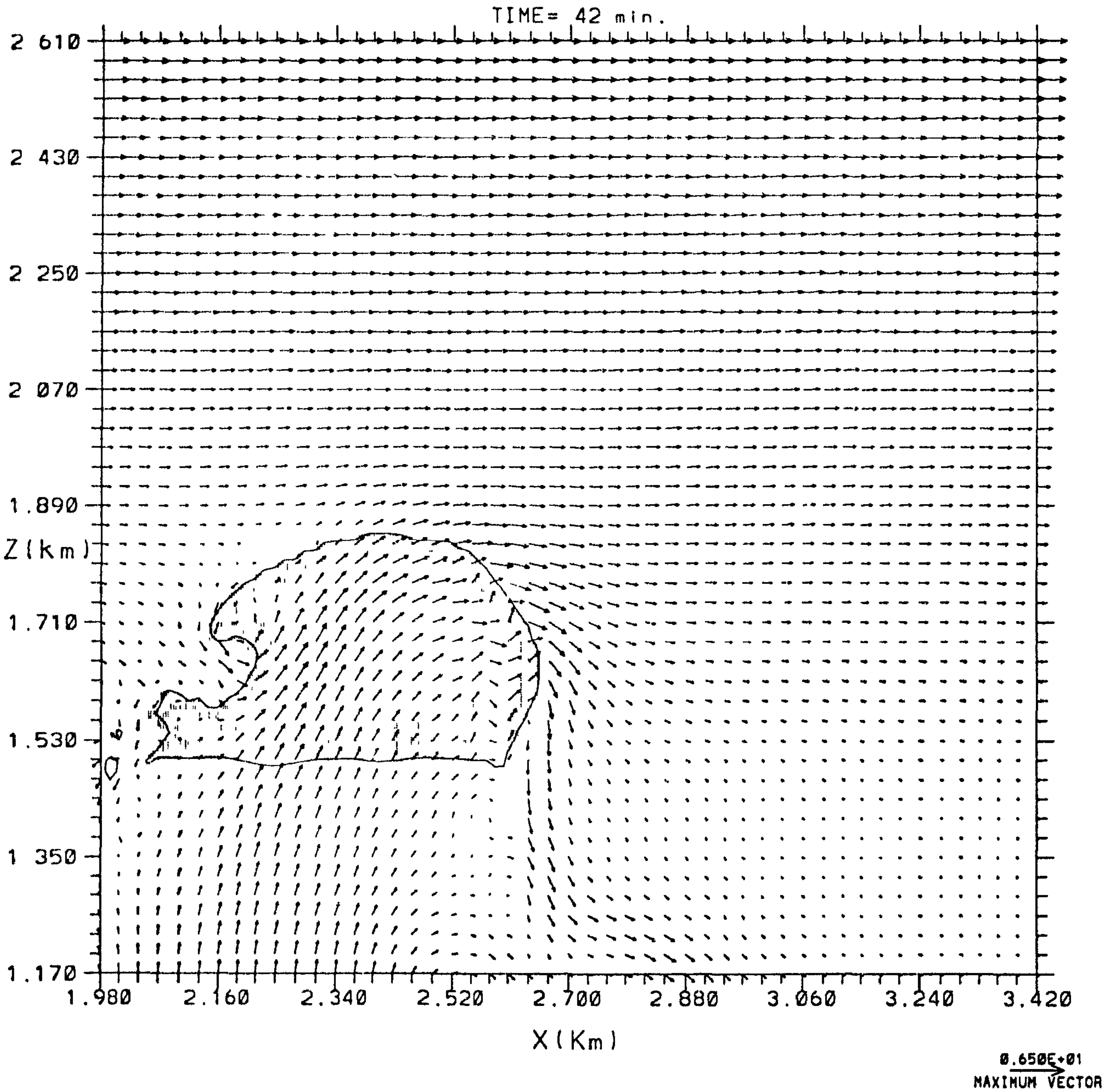

Figure 12: As in figure 10 but for $t = 42min$..

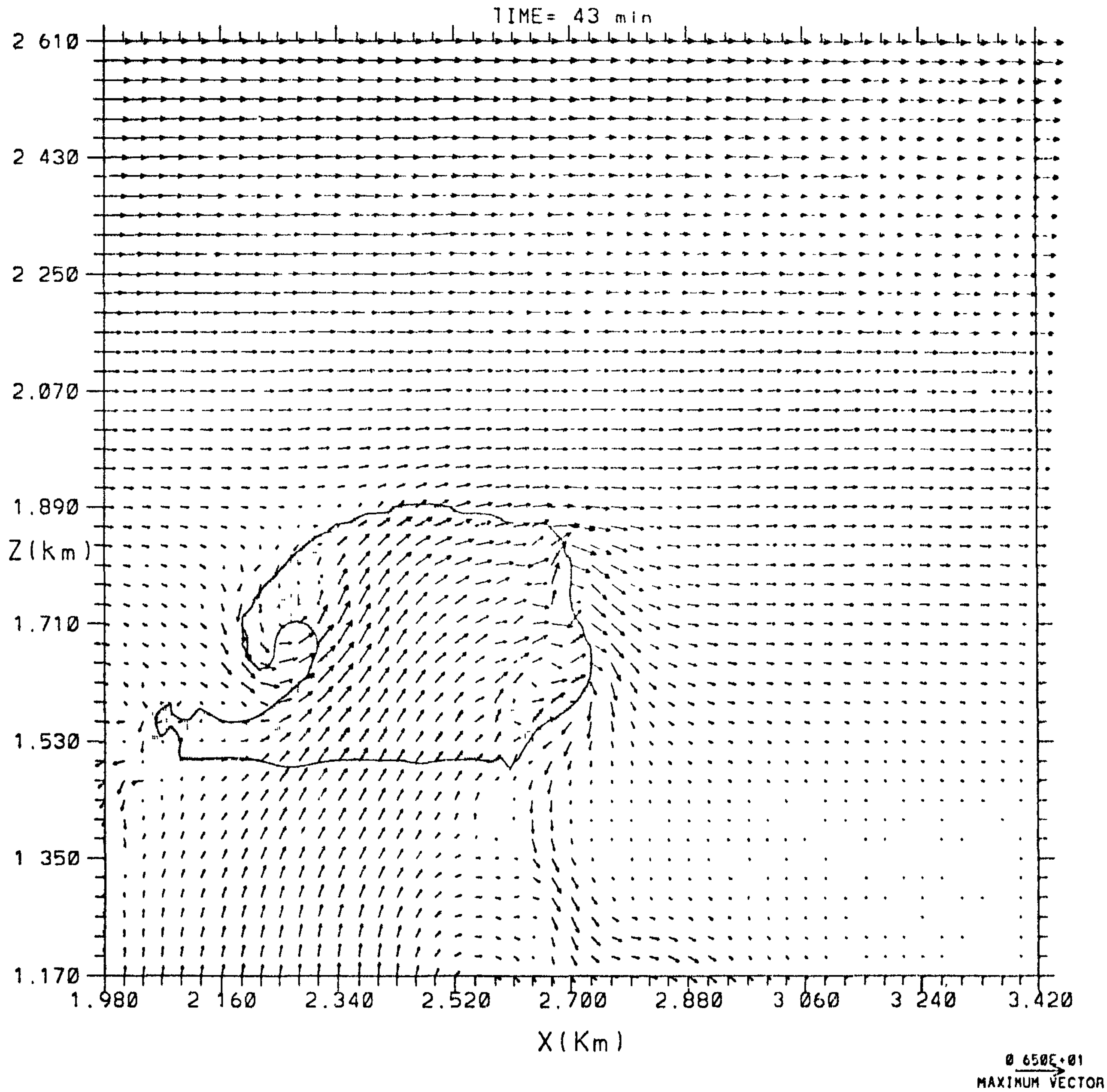

Figure 13: As in figure 10 but for $t = 43min$..

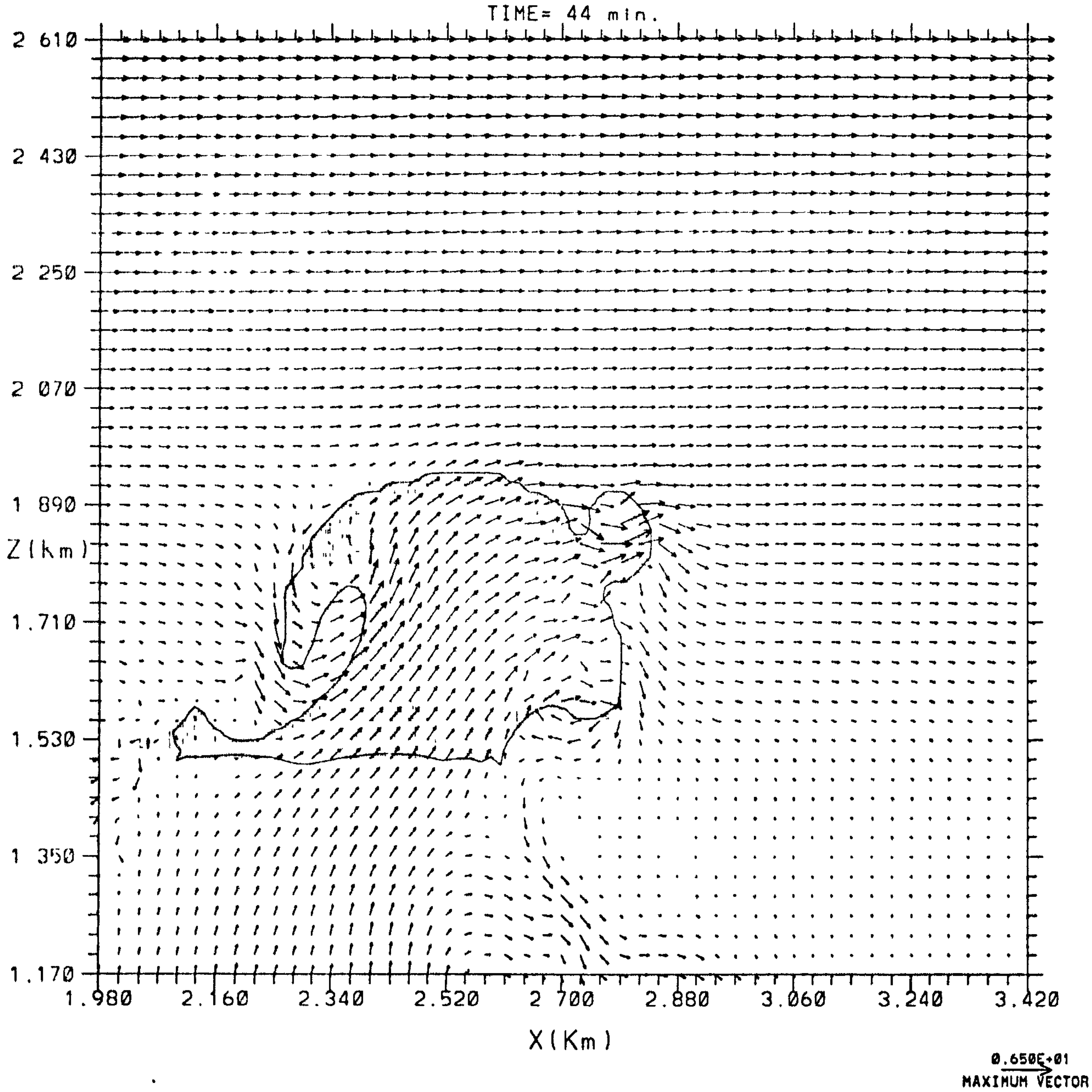

Figure 14: As in figure 10 but for $t = 44min$..

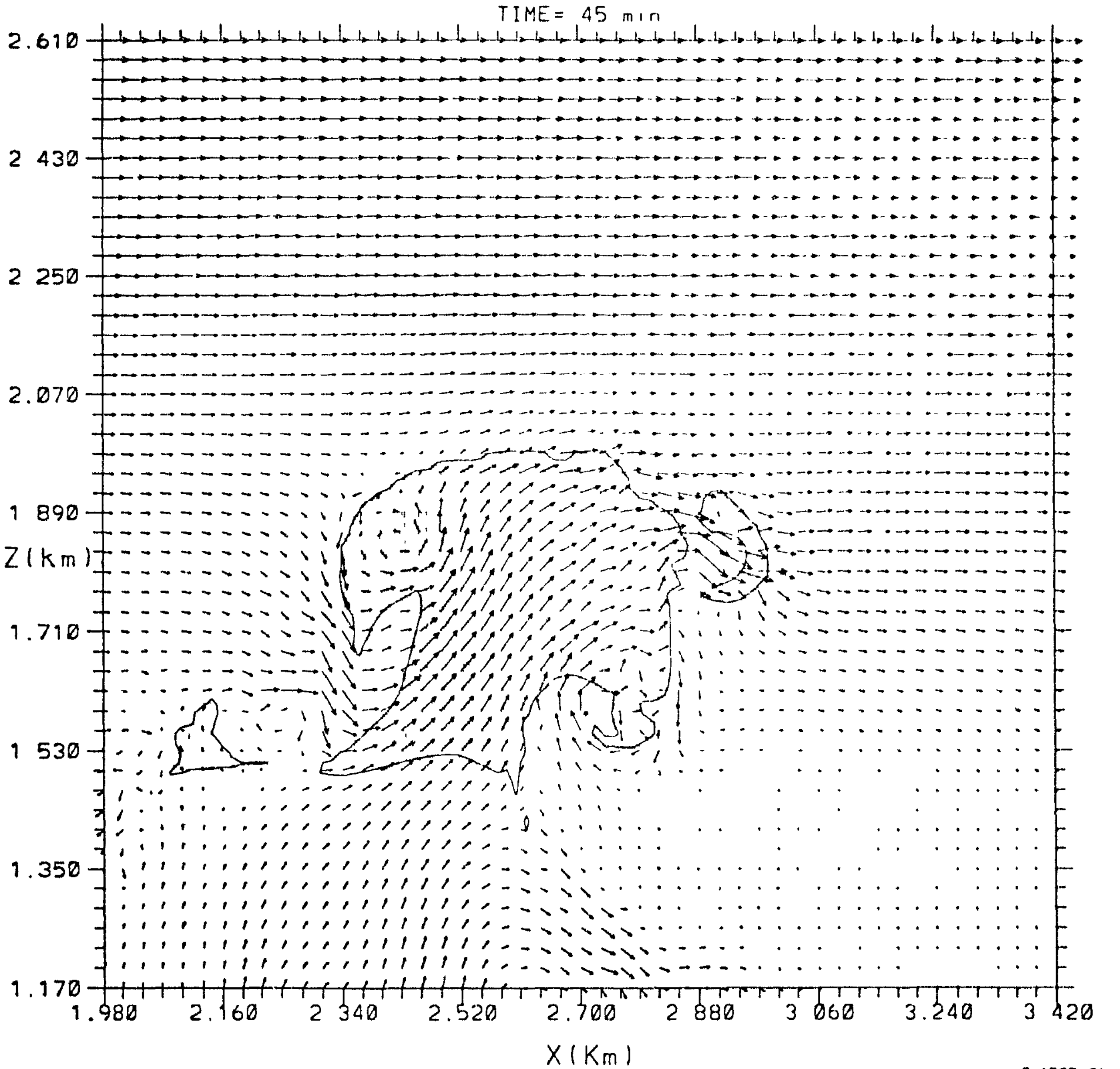

Figure 15: As in figure 10 but for $t = 45min$..

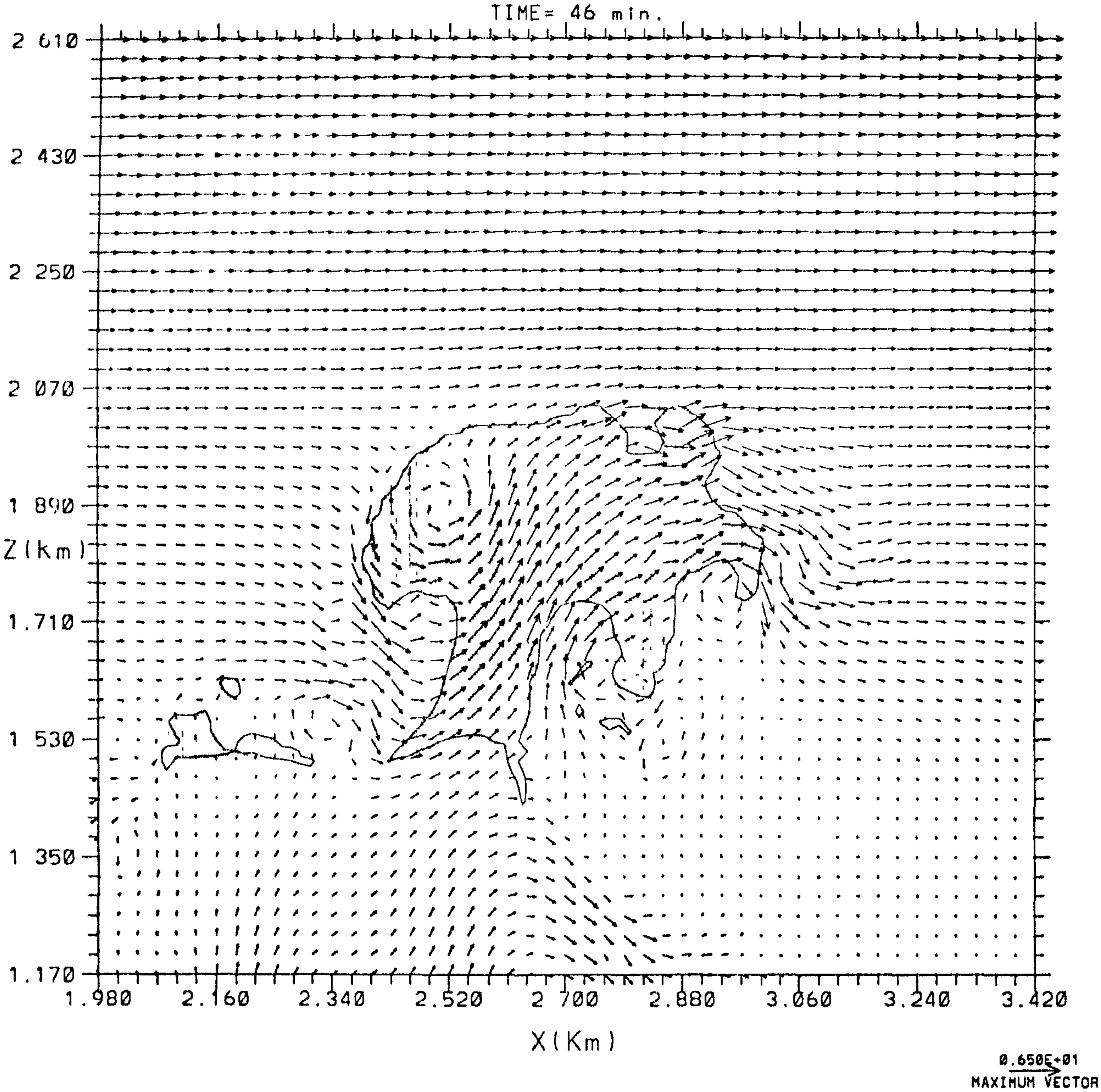

Figure 16: As in figure 10 but for $t = 46min.$.

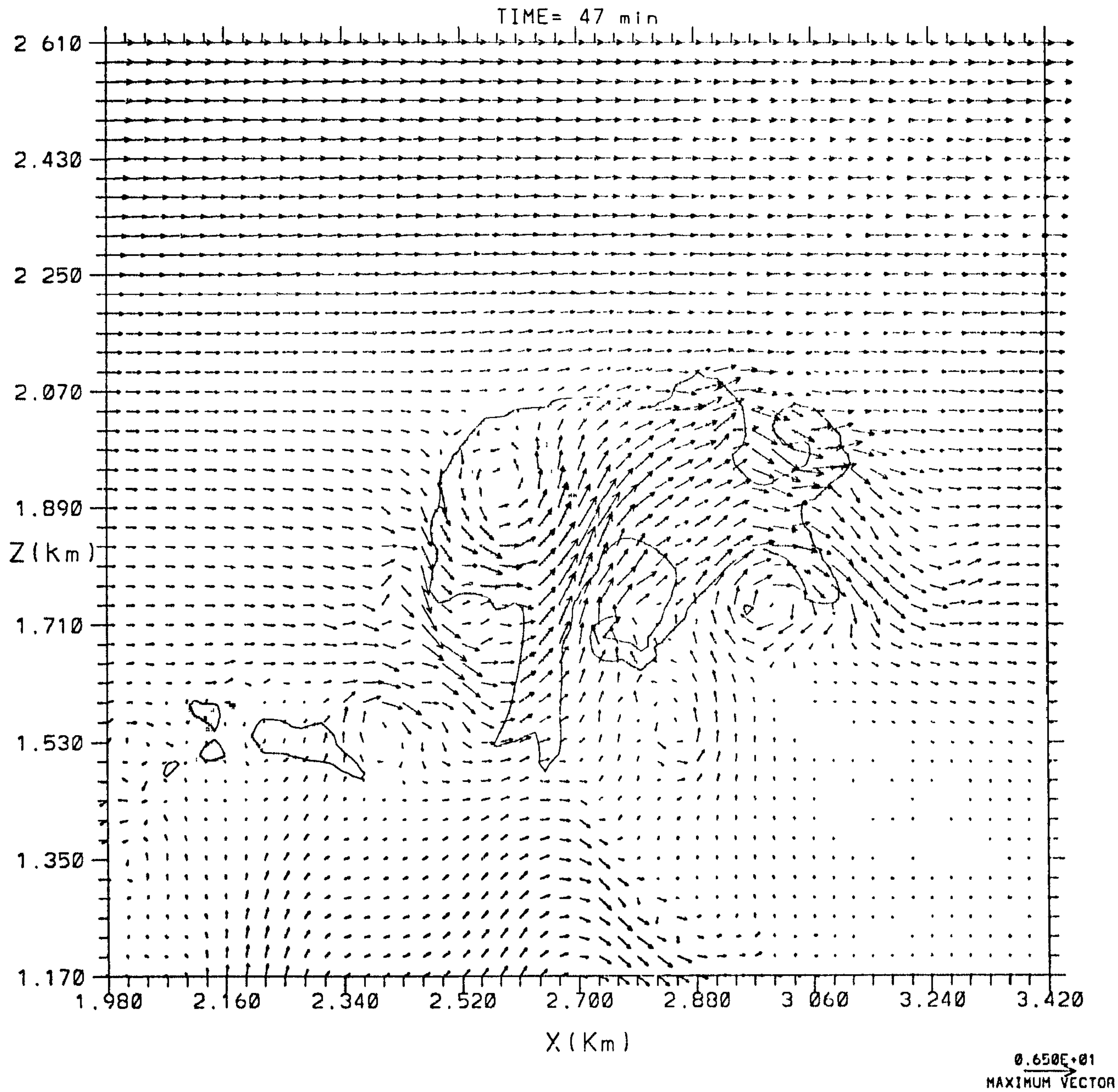

Figure 17: As in figure 10 but for $t = 47min$..

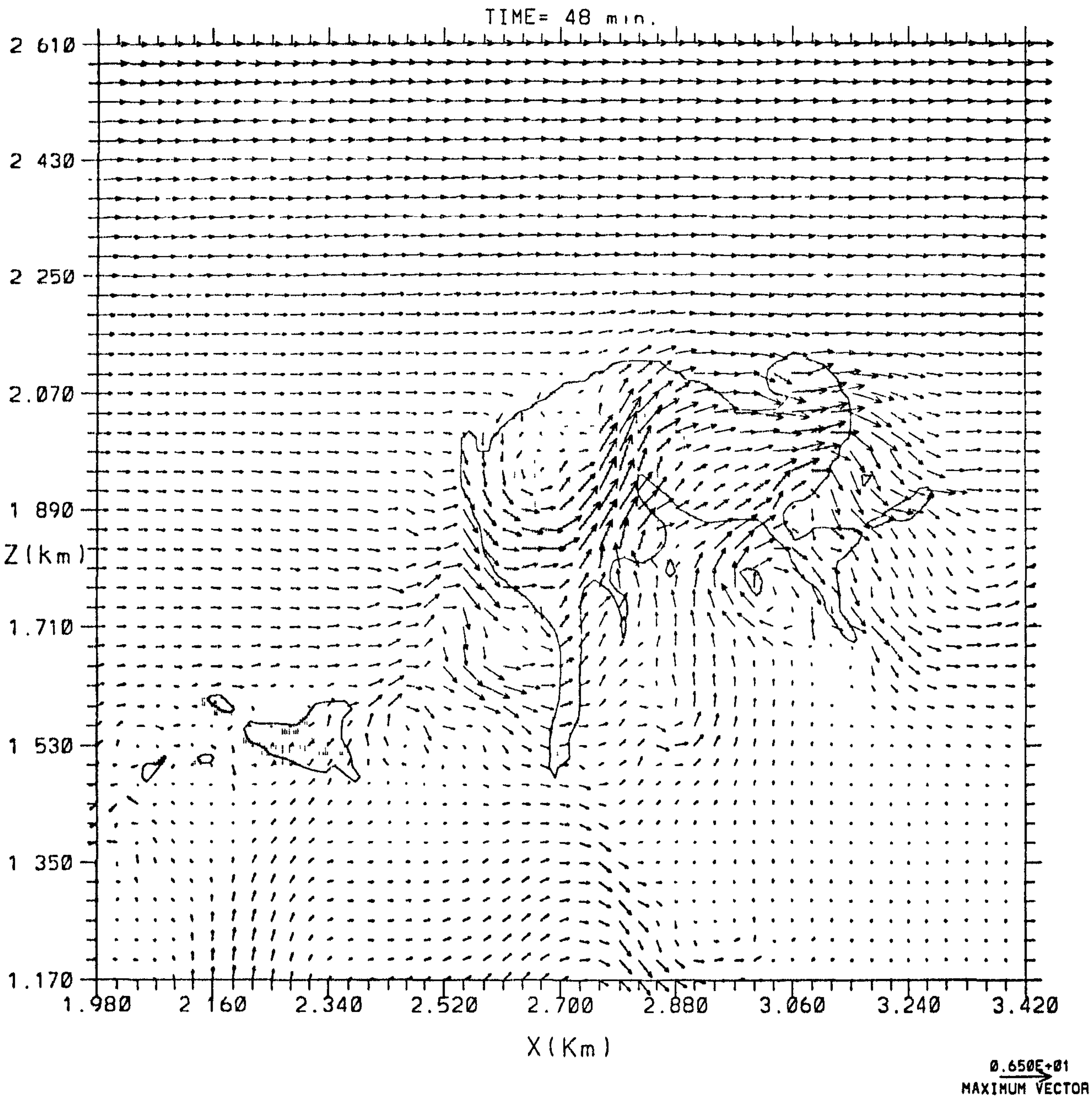

Figure 18: As in figure 10 but for $t = 48min$..

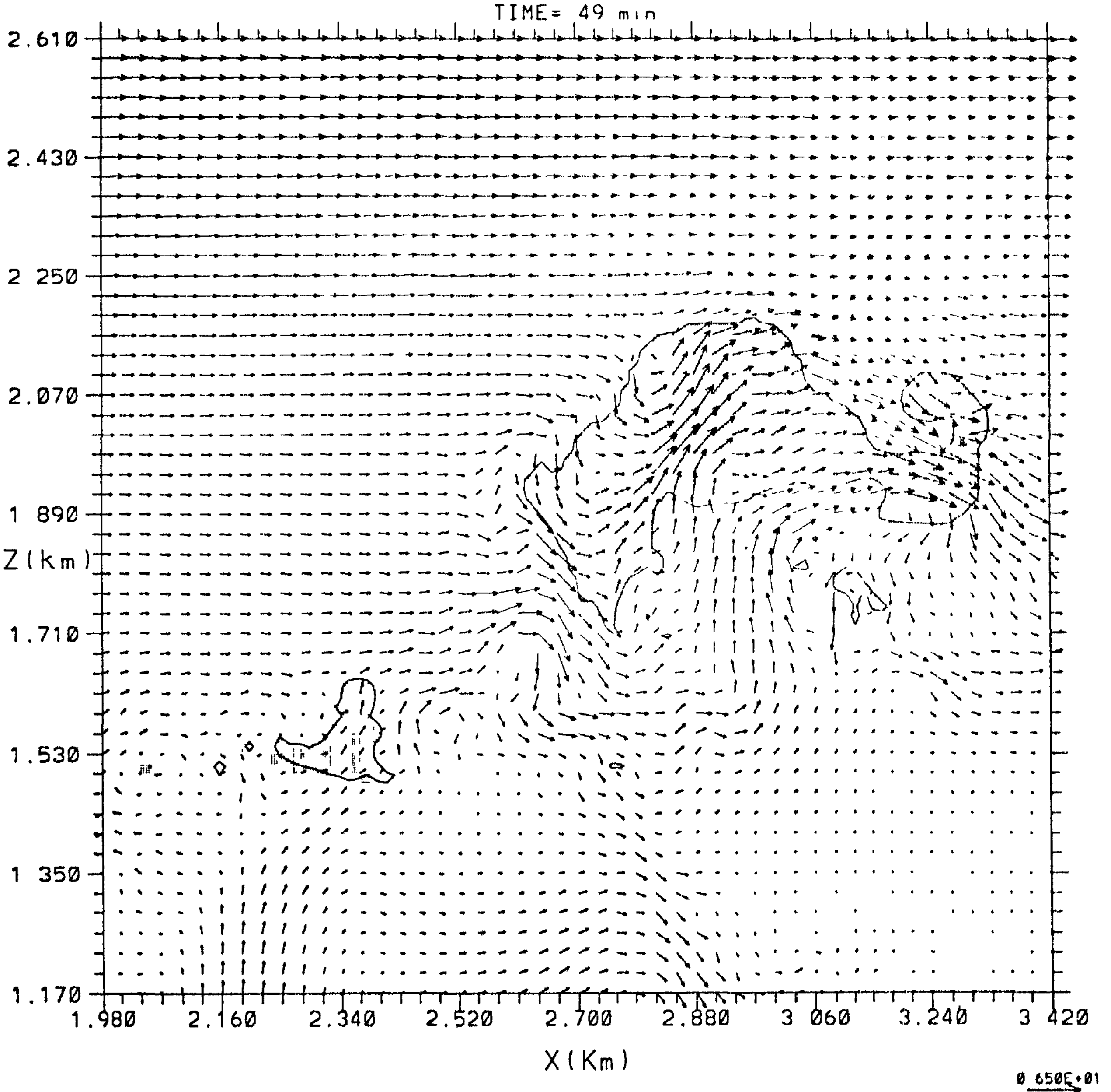

Figure 19: As in figure 10 but for $t = 49min$..

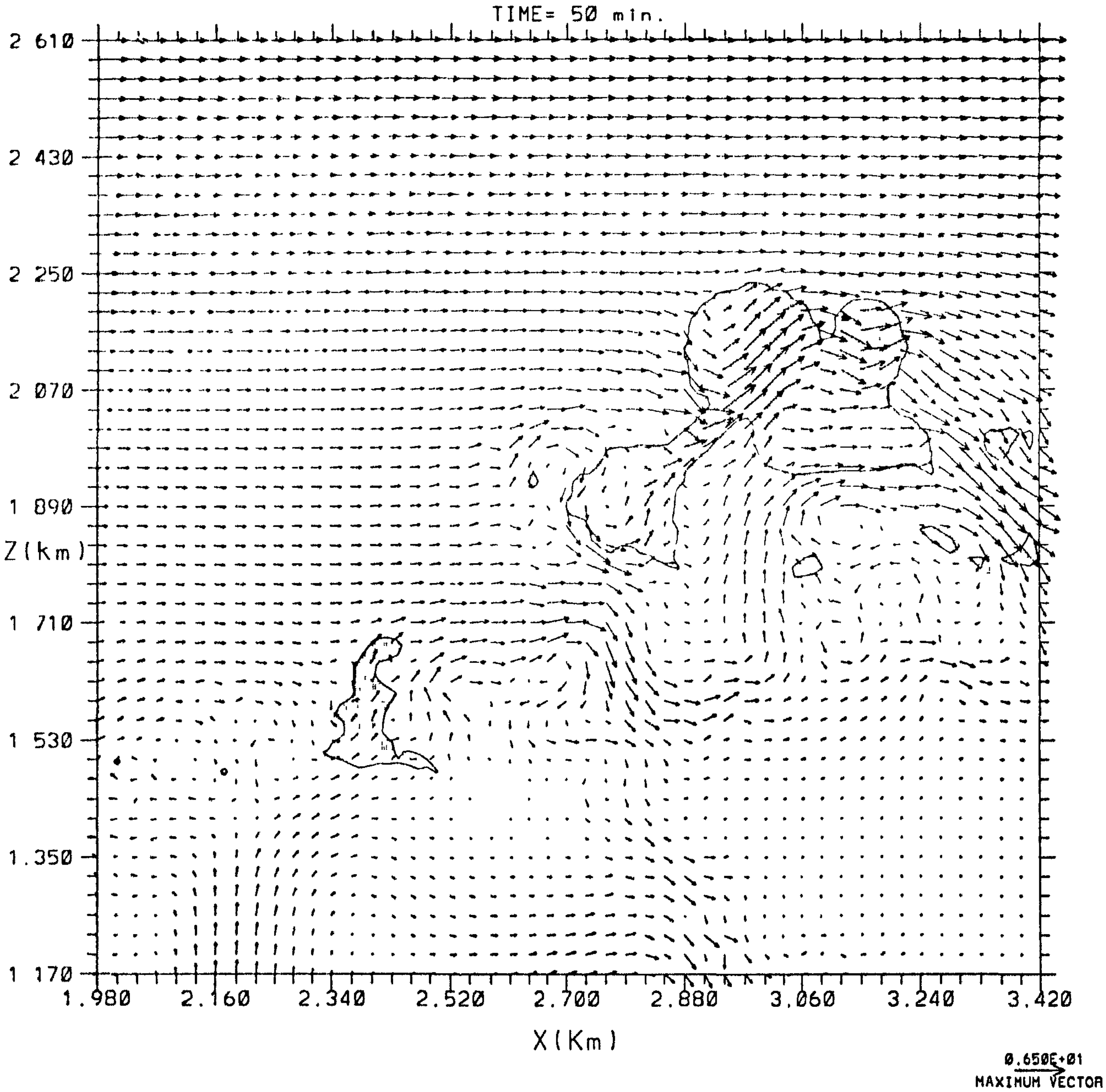

Figure 20: As in figure 10 but for $t = 50min.$.

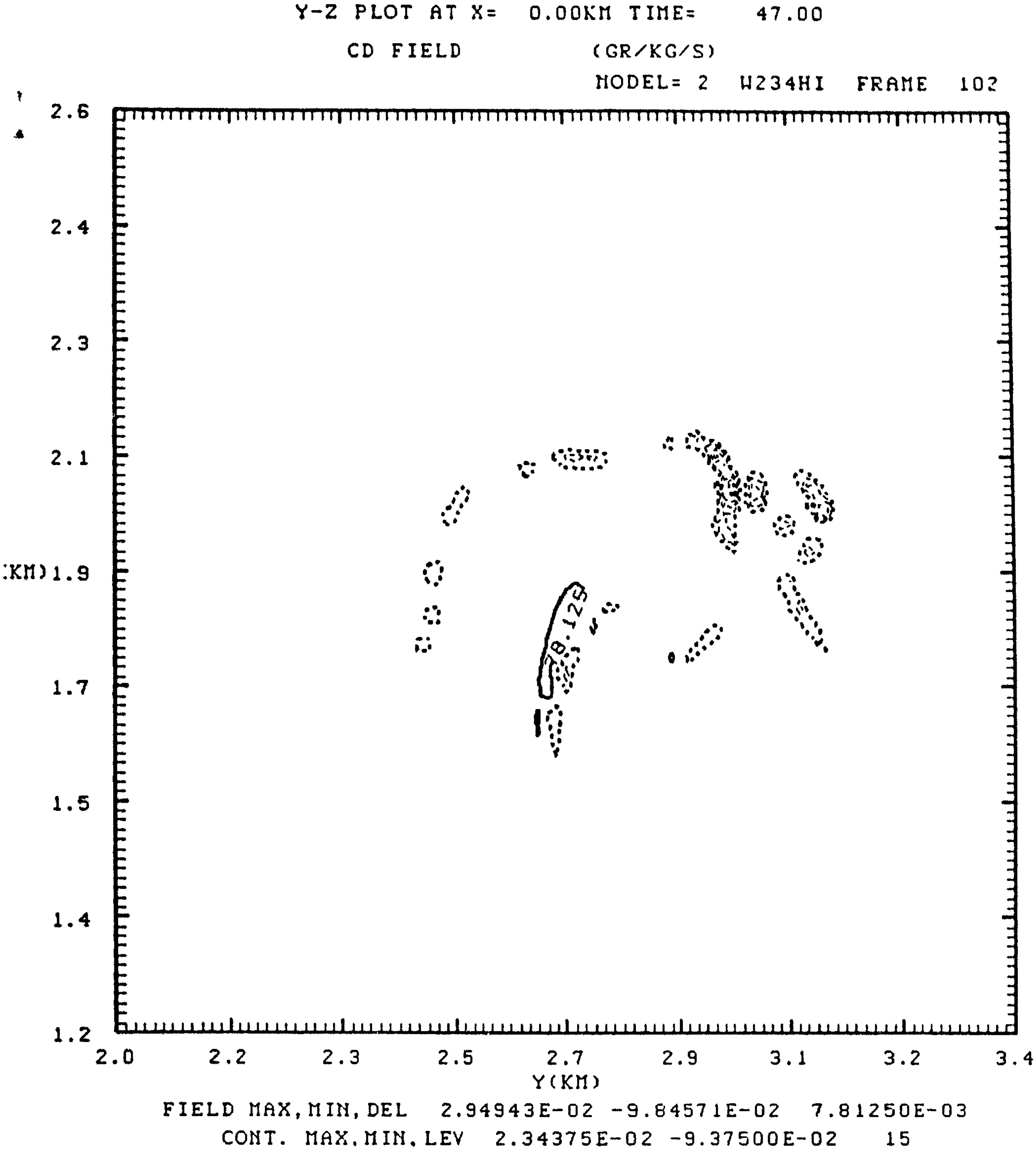

Figure 21: Condensation rate field at $t = 47min.$, units are $g/kg/s$.

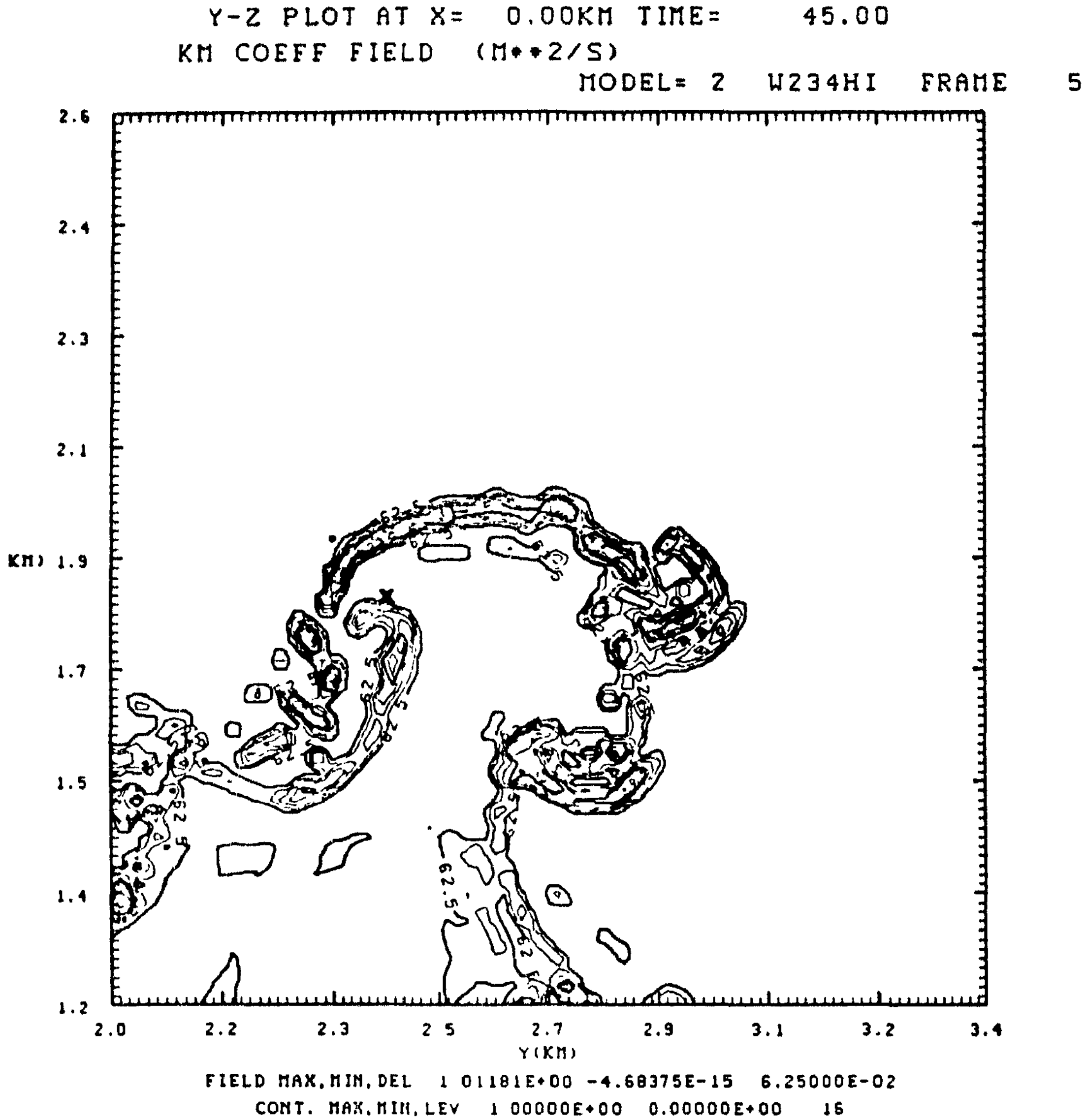

Figure 22: Eddy mixing coefficient field at $t = 45min.$, units are m^2s^{-1} , X indicates upshear vortex center.

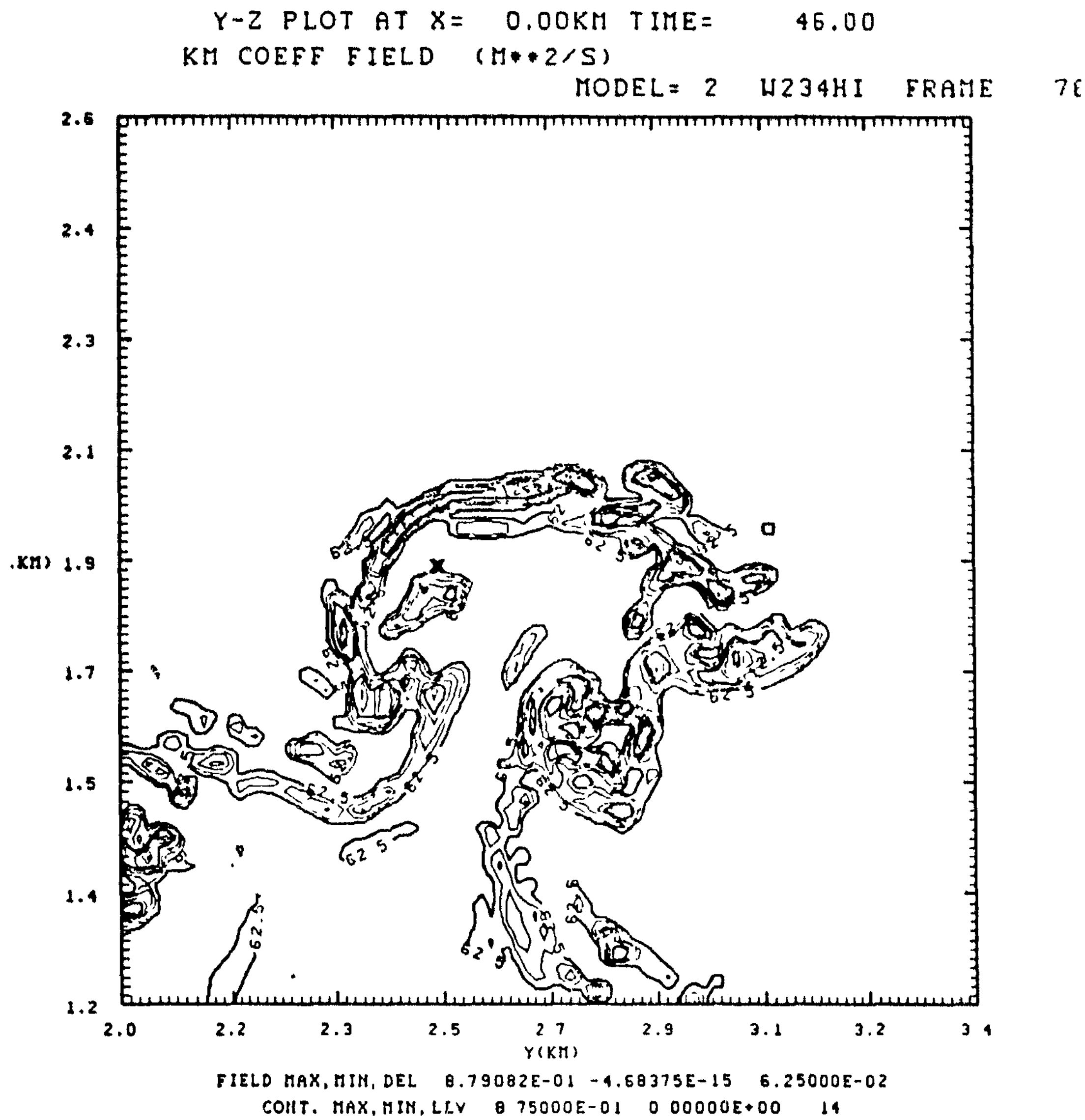

Figure 23: As in figure 22 but for $t = 46min$..

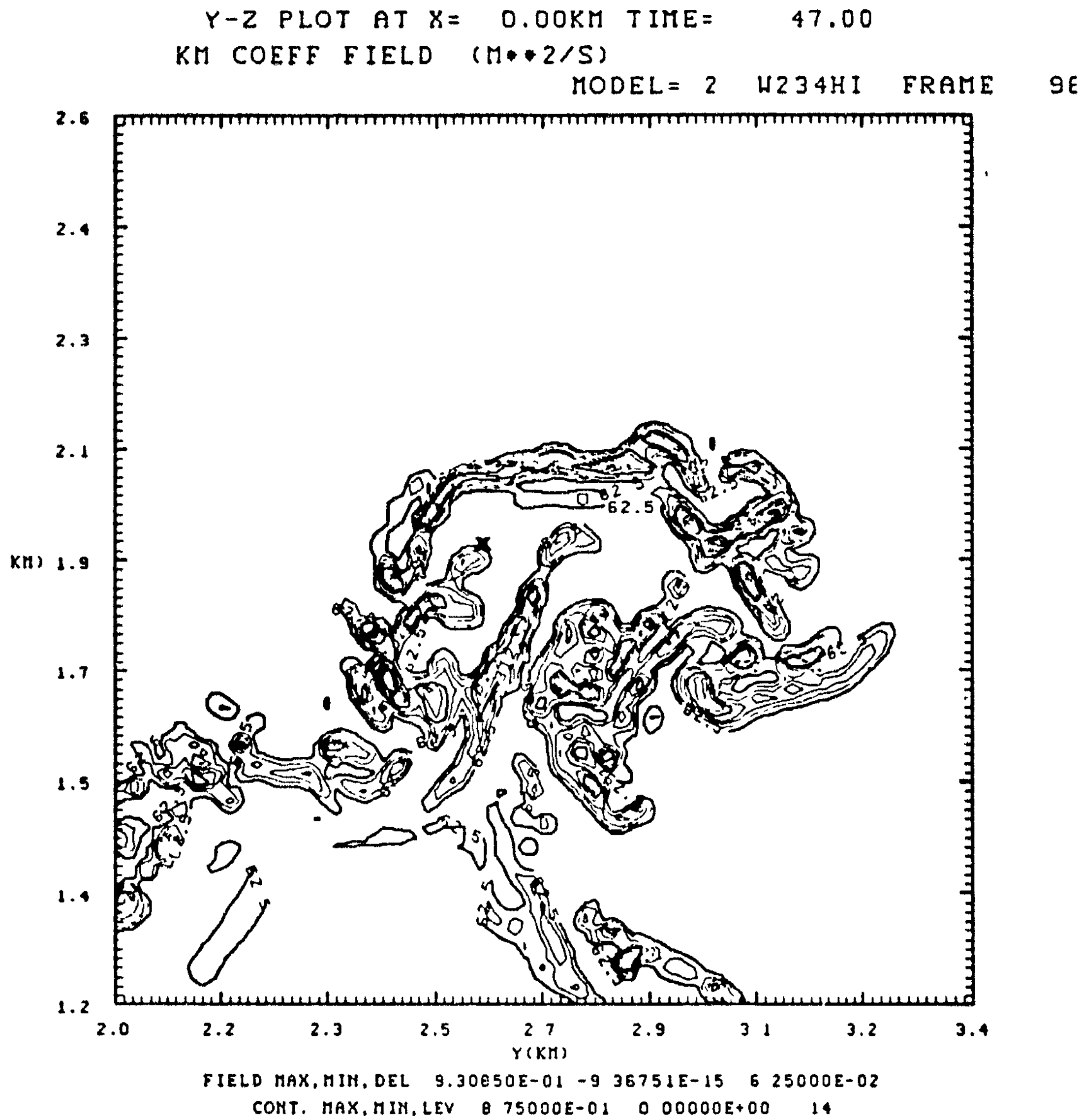

Figure 24: As in figure 22 but for $t = 47min.$.

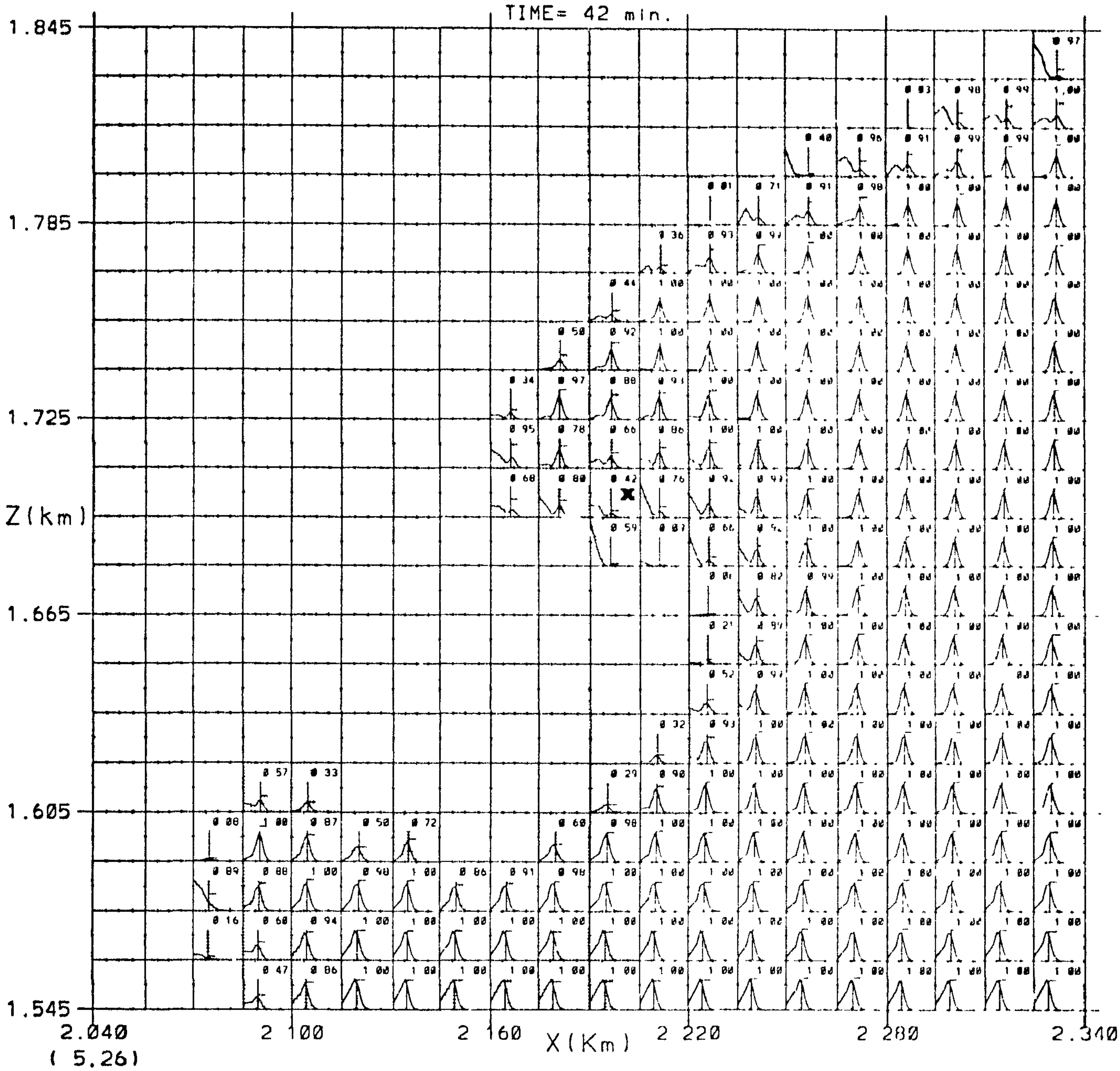

Figure 25: B^2-distributions at $t = 42min.$ for upper upshear portion of cloud.

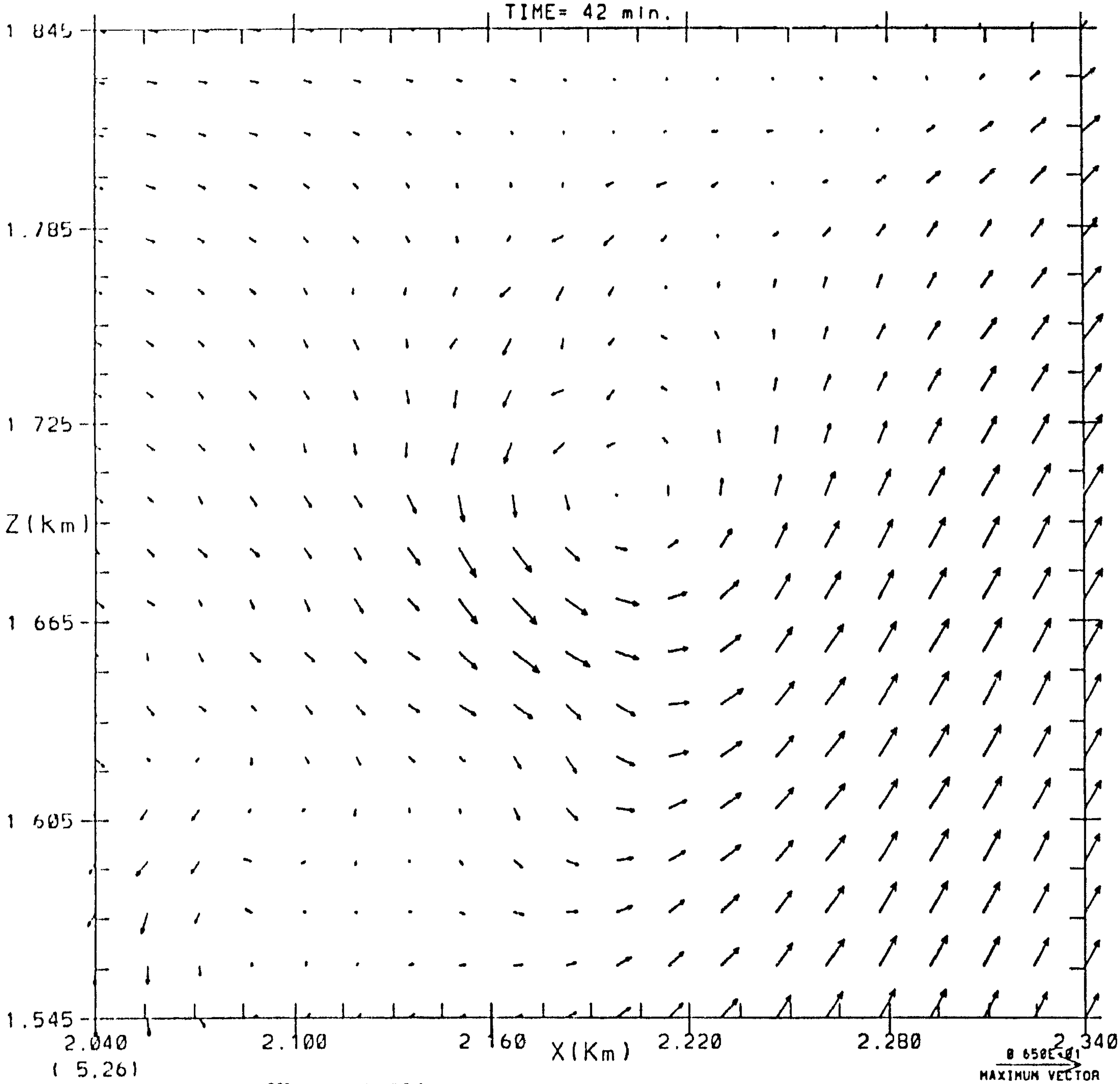

Figure 26: Velocity vectors for domain of figure 25.

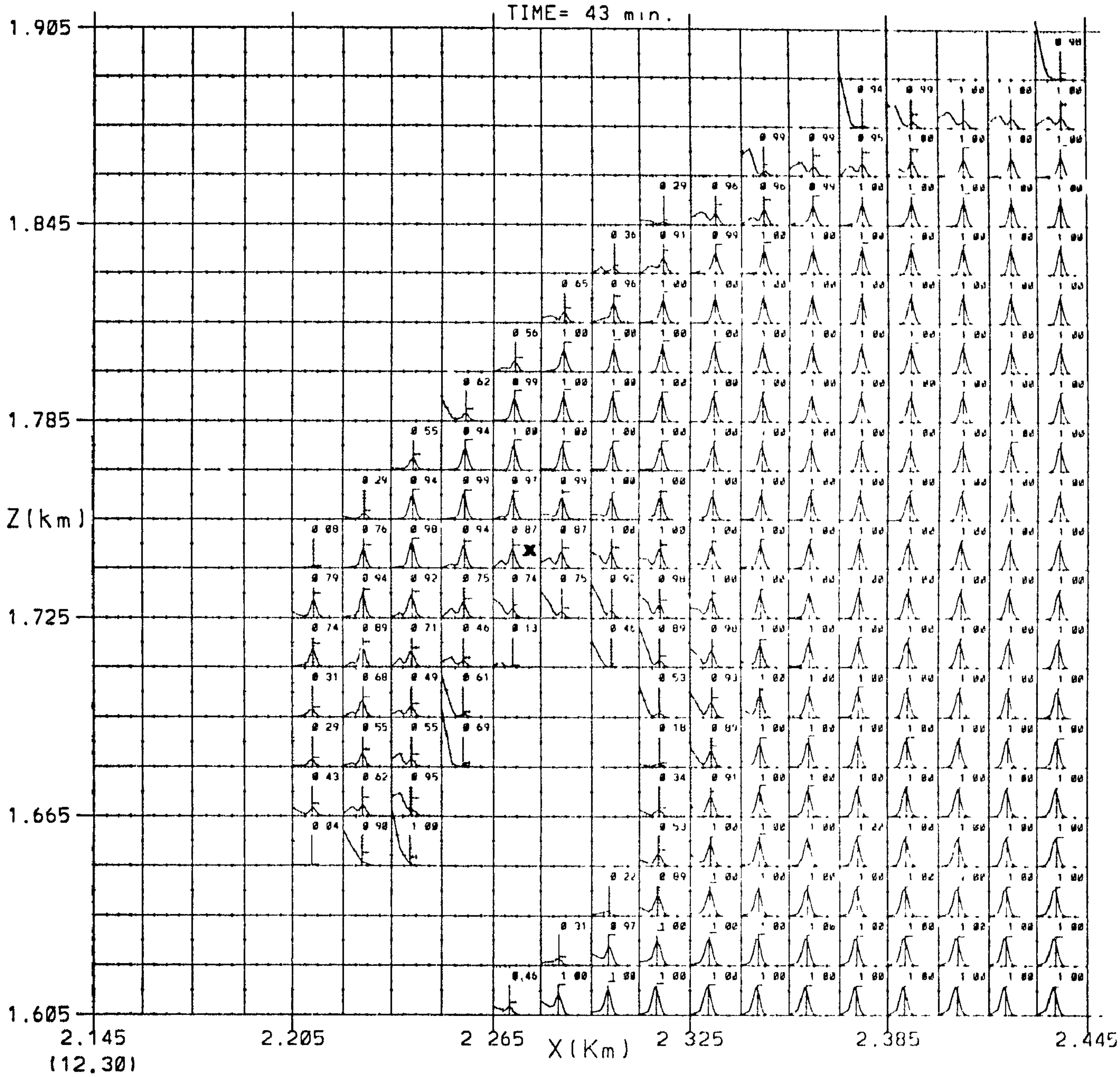

Figure 27: B^2–distributions at $t = 43min.$ for upper upshear portion of cloud.

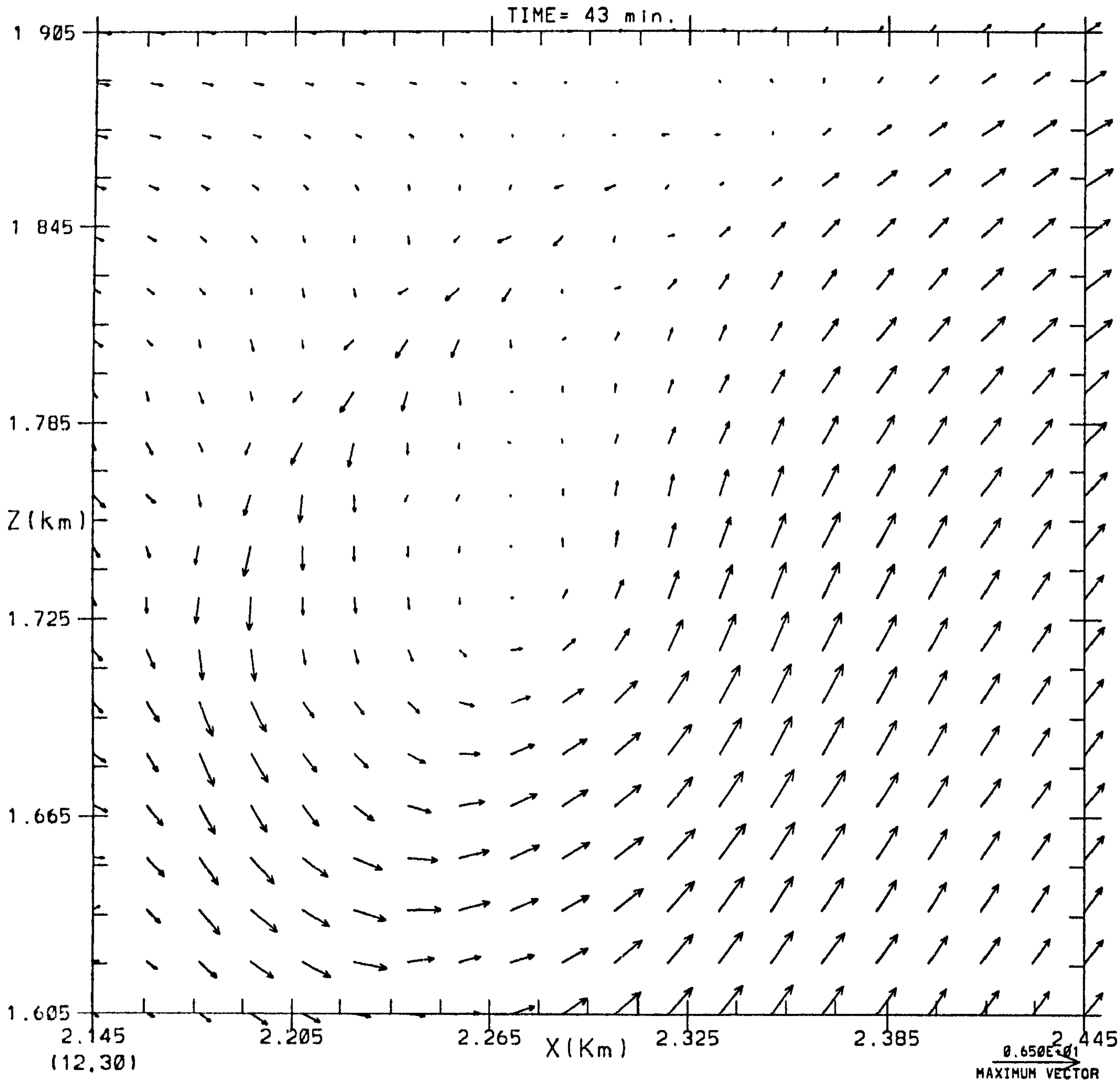

Figure 28: Velocity vectors for domain of figure 27.

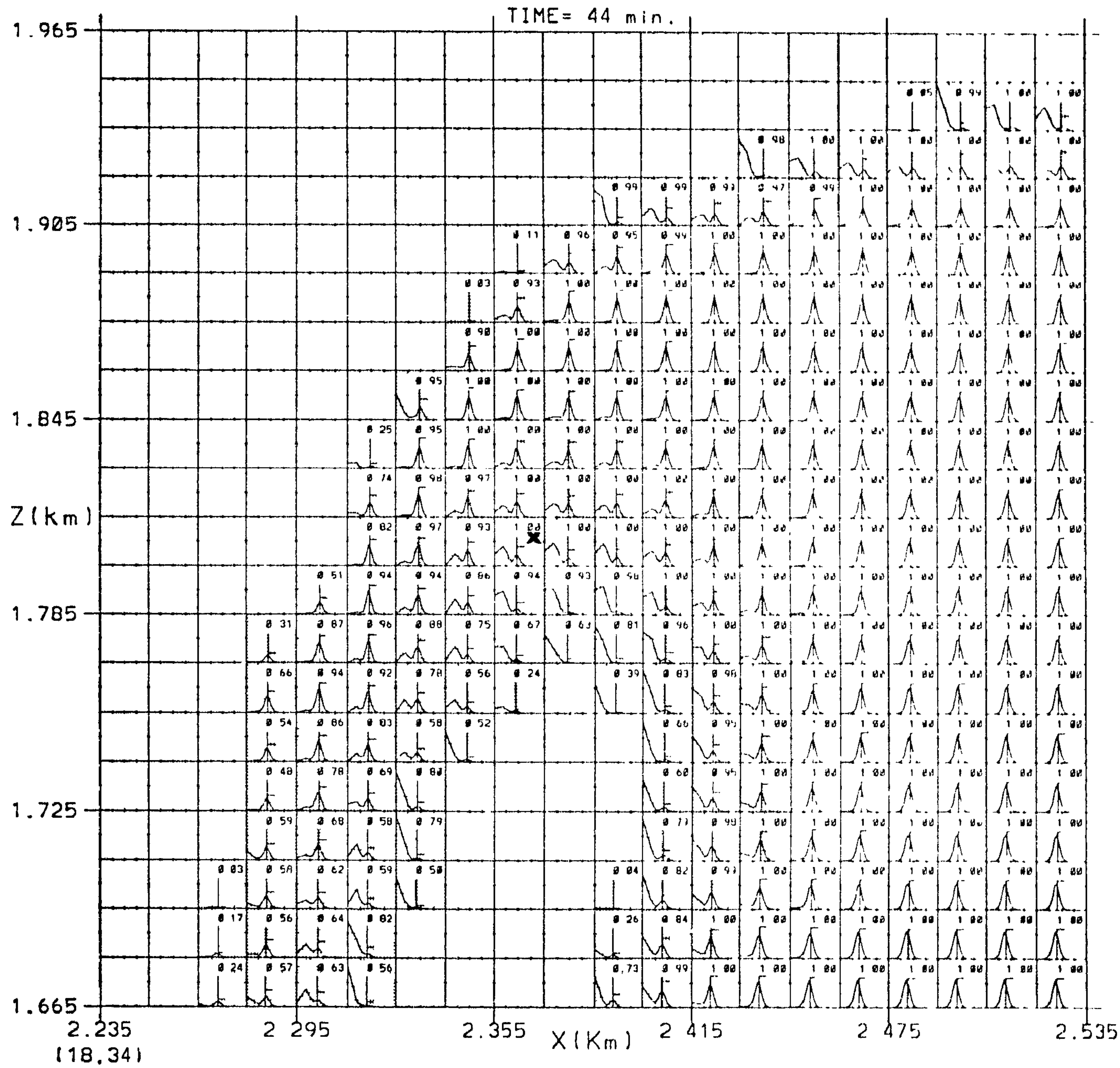

Figure 29: B^2–distributions at $t = 44min.$ for upper upshear portion of cloud.

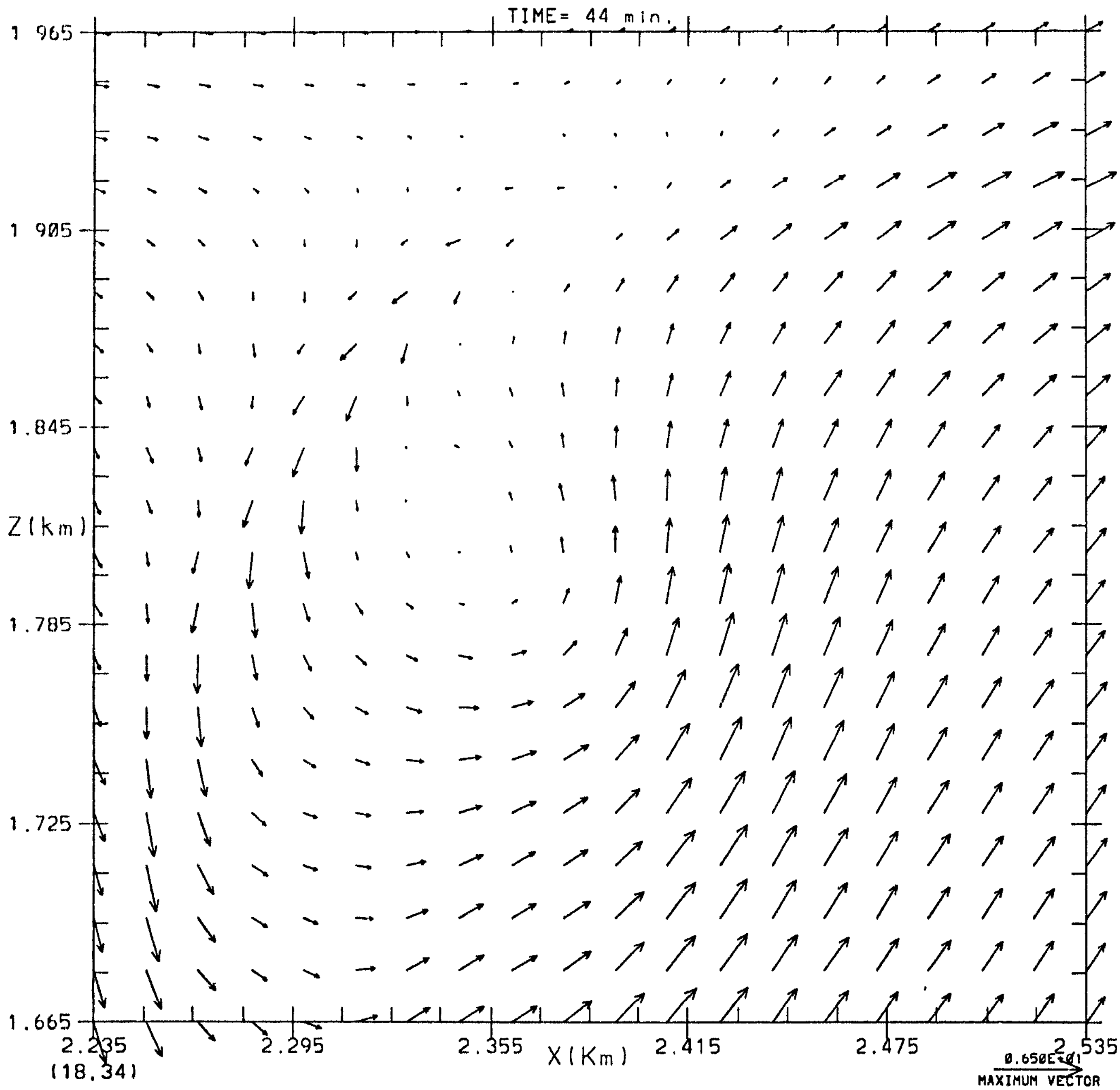

Figure 30: Velocity vectors for domain of figure 29.

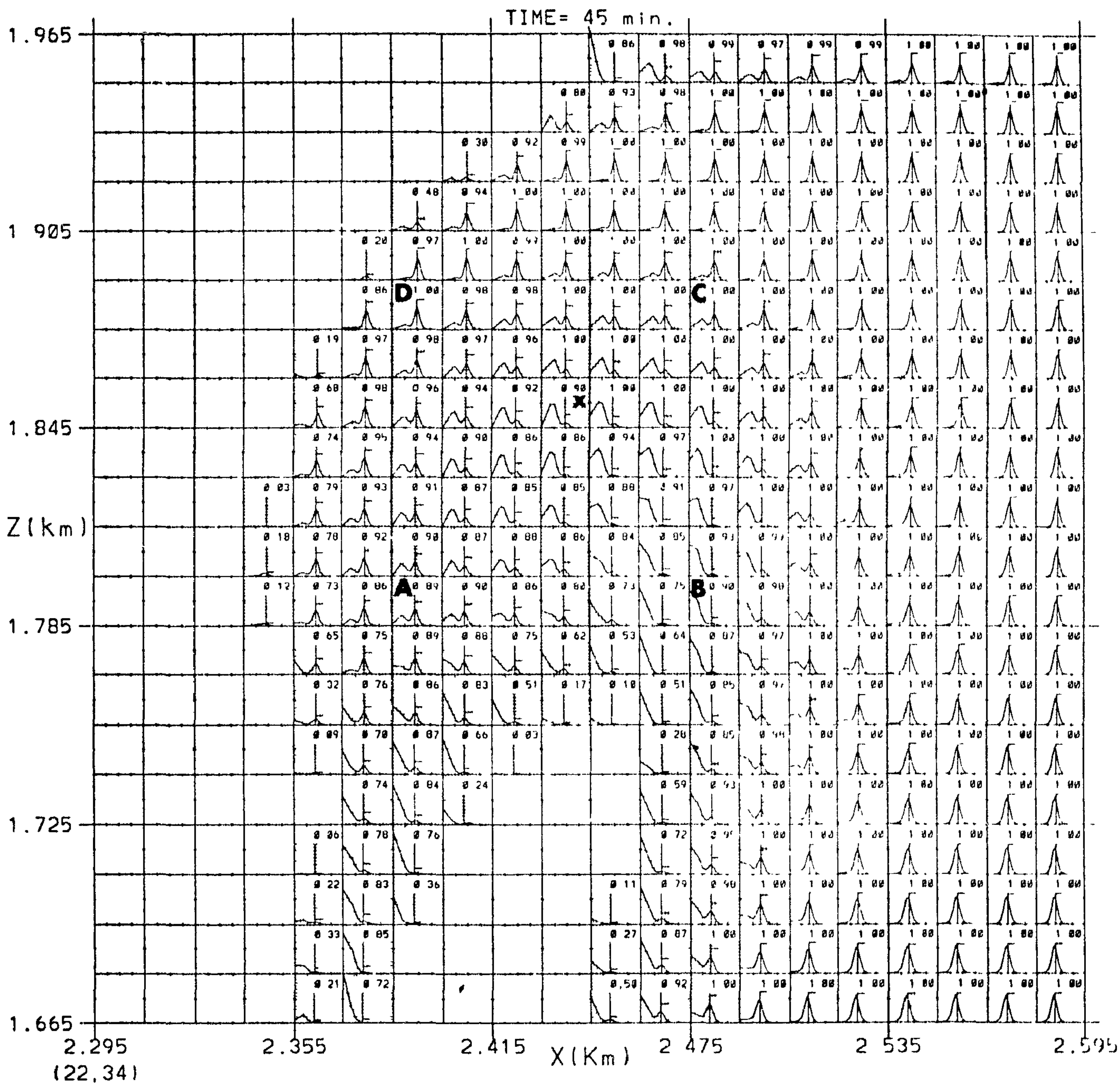

Figure 31: B^2–distributions at $t = 45min.$ for upper upshear portion of cloud.

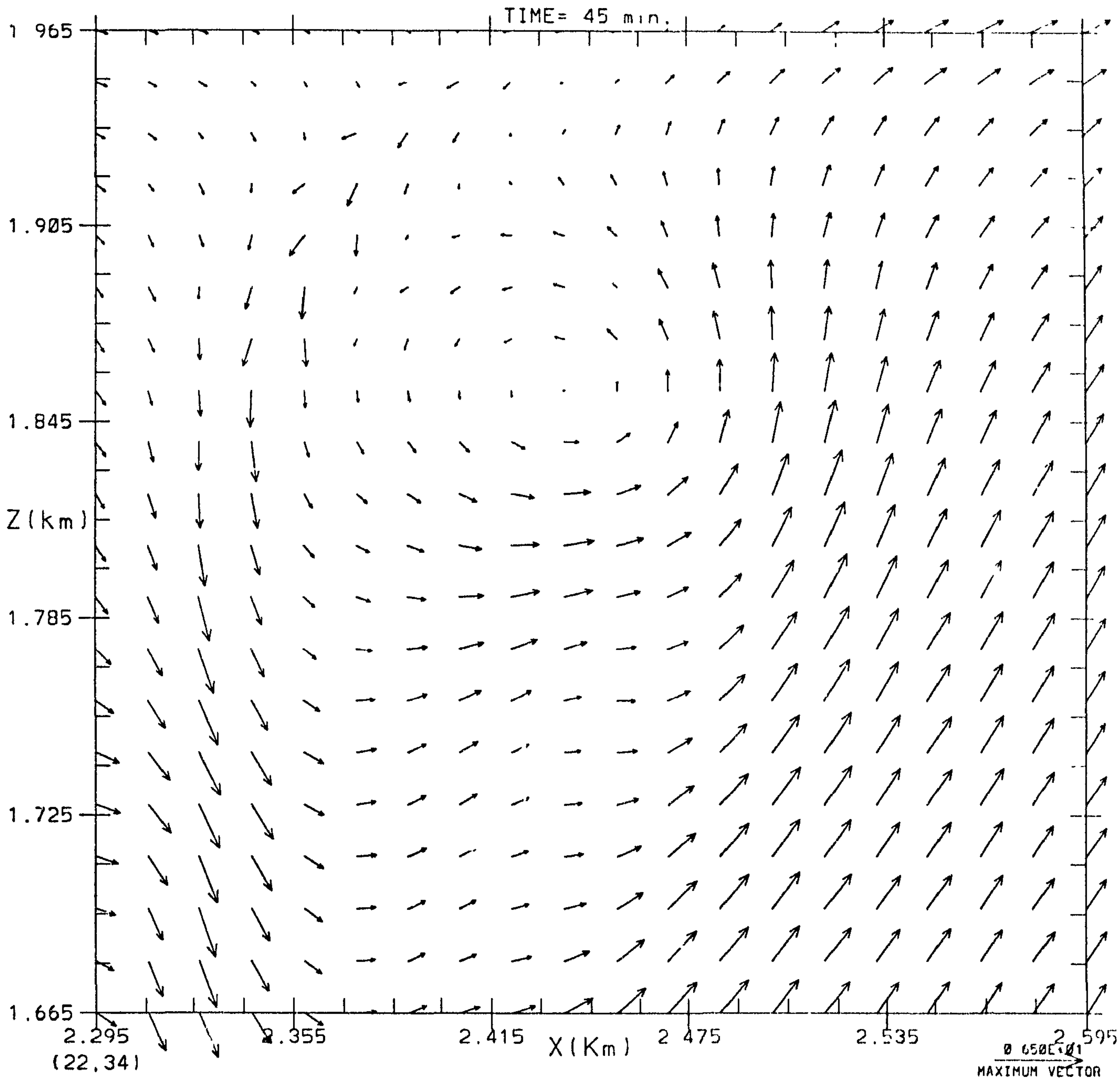

Figure 32: Velocity vectors for domain of figure 31.

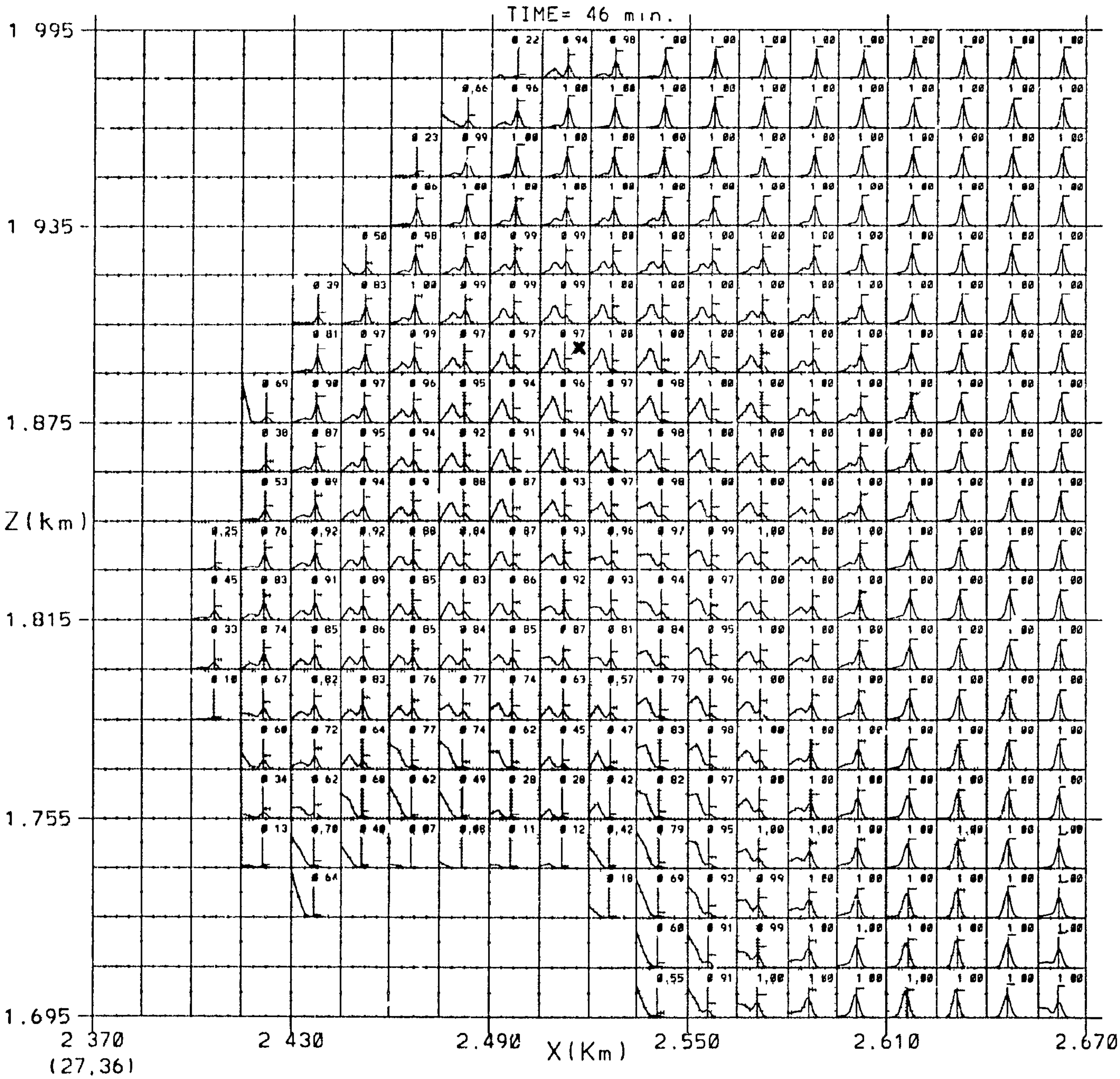

Figure 33: B^2–distributions at $t = 46min.$ for upper upshear portion of cloud.

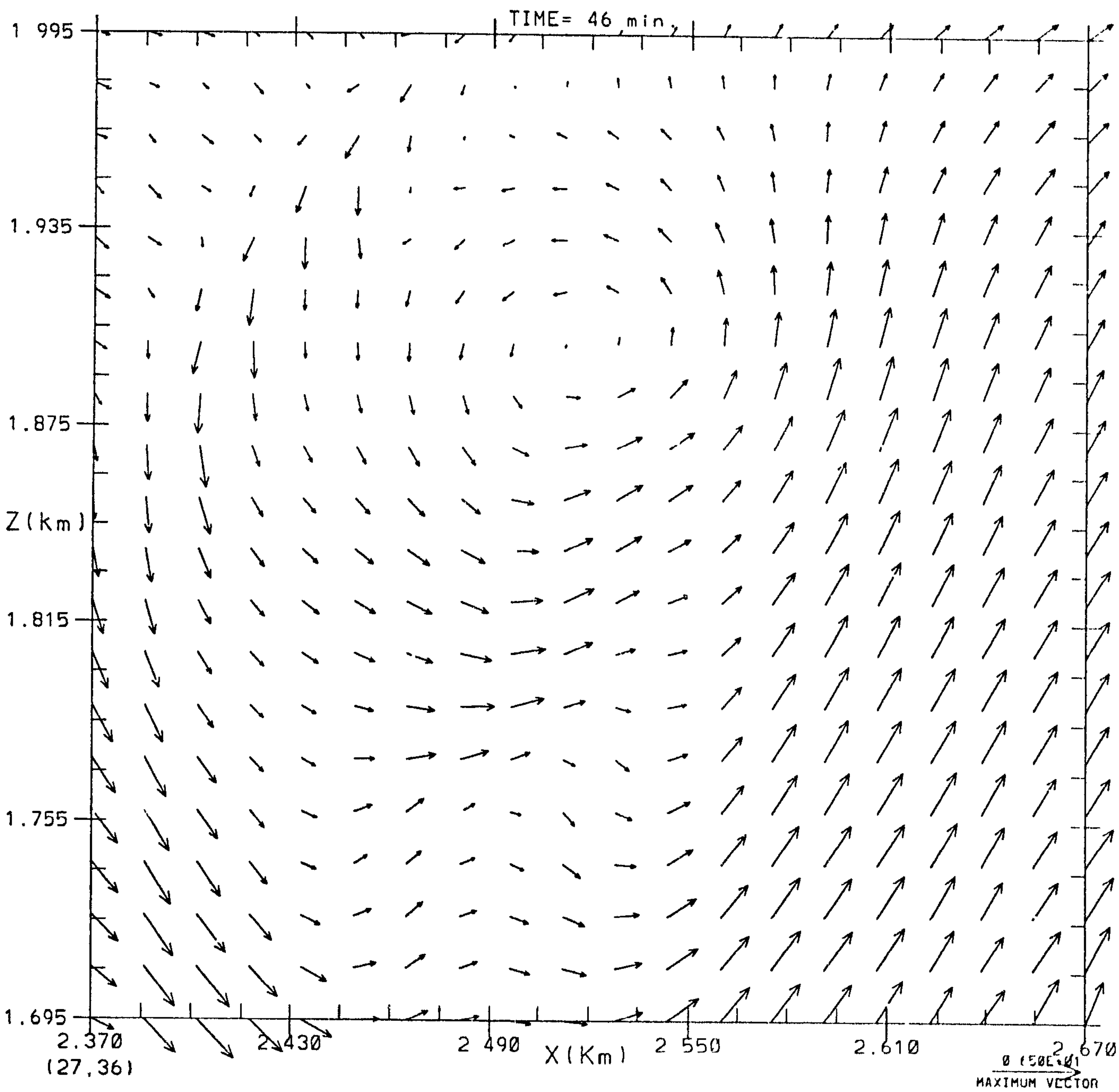

Figure 34: Velocity vectors for domain of figure 33.

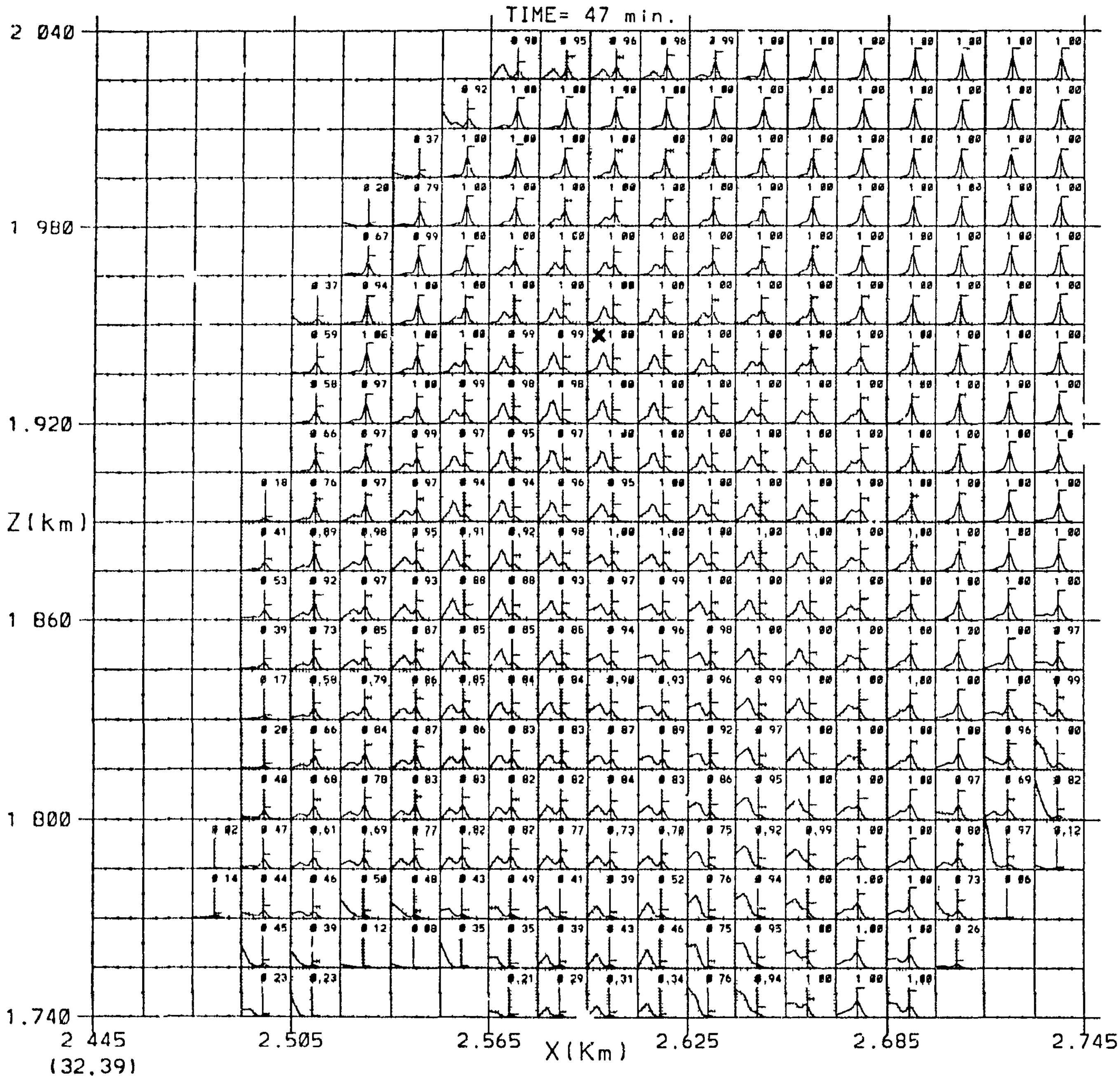

Figure 35: B^2-distributions at $t = 47min.$ for upper upshear portion of cloud.

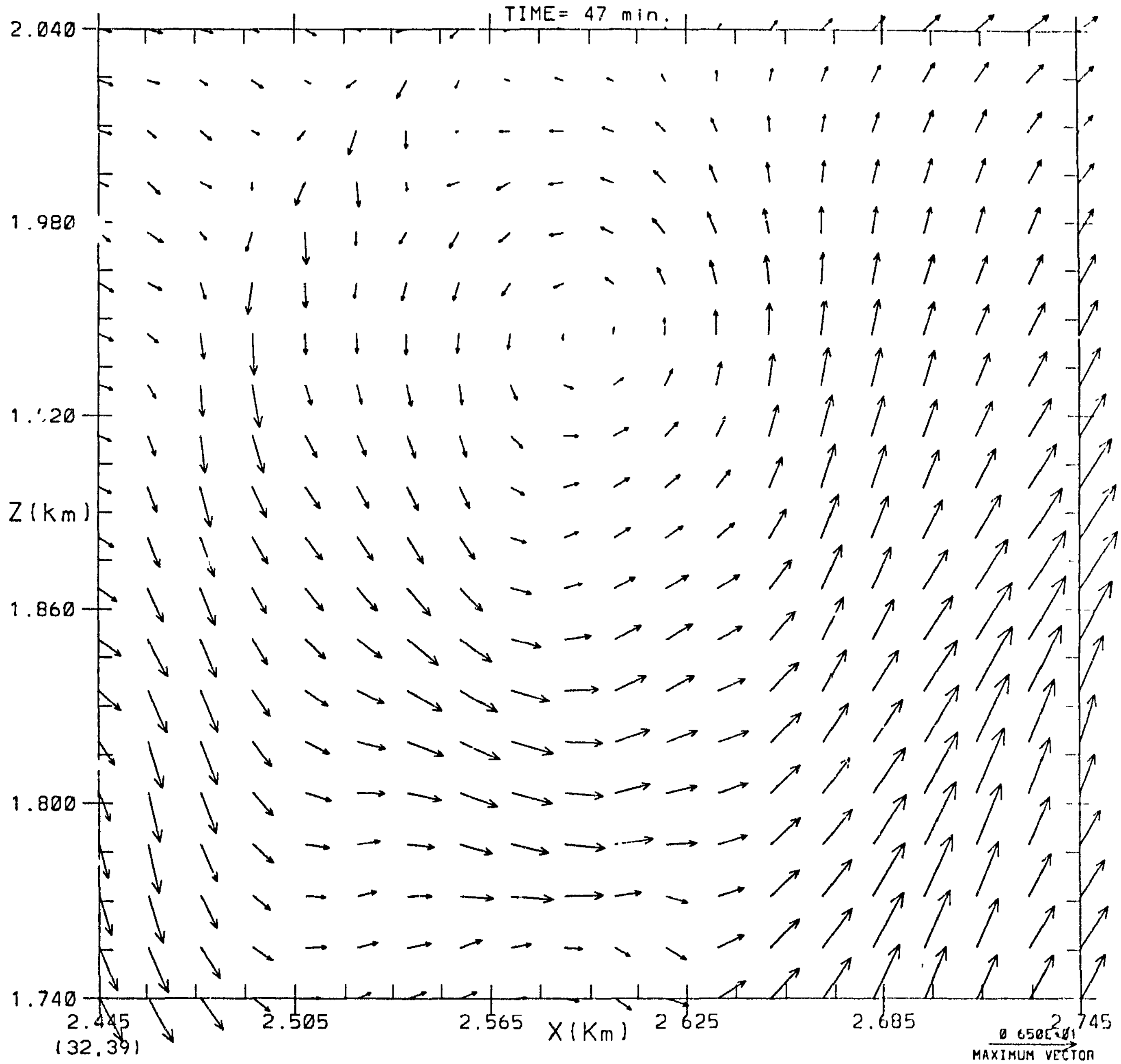

Figure 36: Velocity vectors for domain of figure 35.

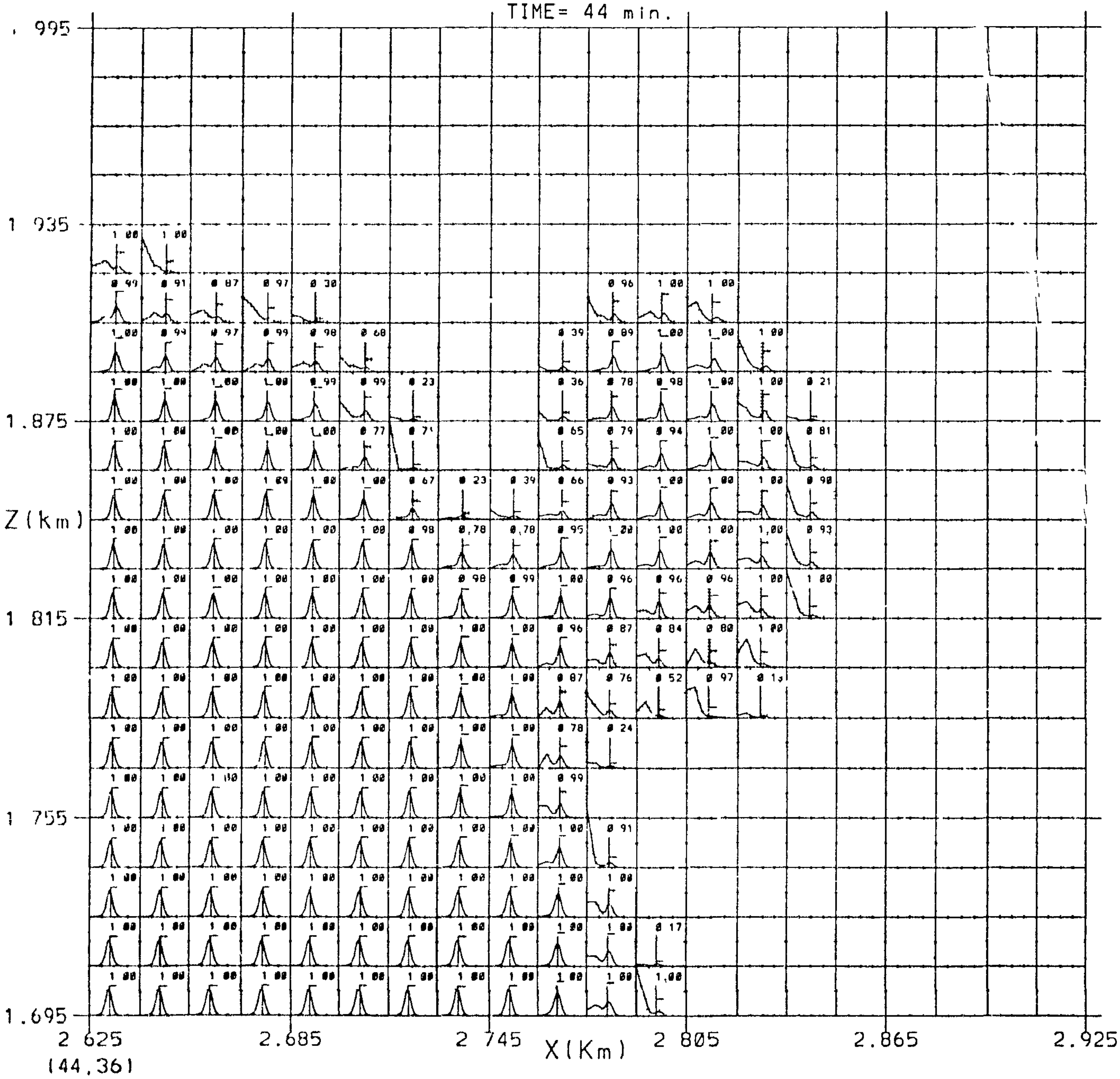

Figure 37: B^2-distributions at t = 44min. for upper downshear portion of cloud.

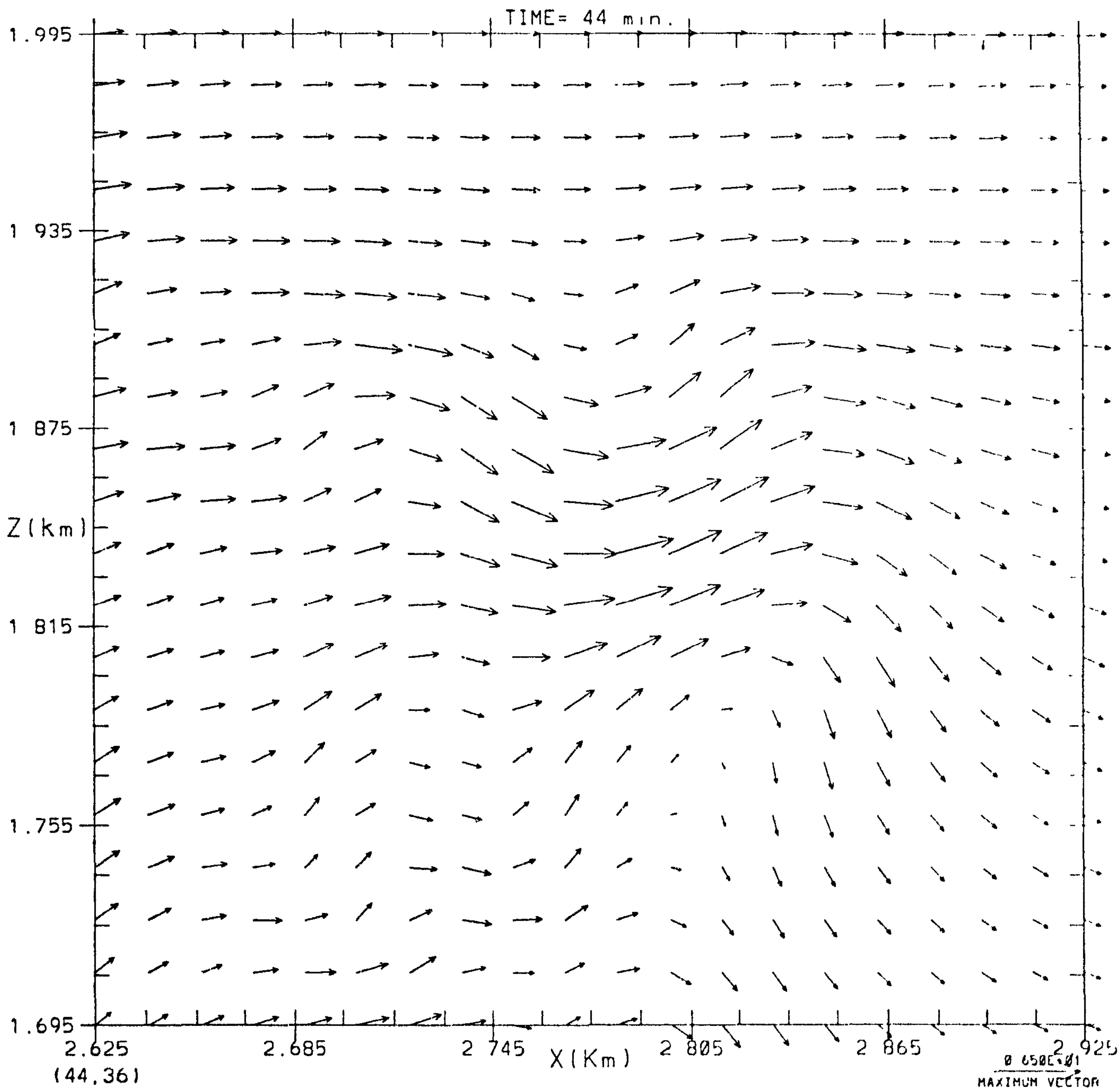

Figure 38: Velocity vectors for domain of figure 37.

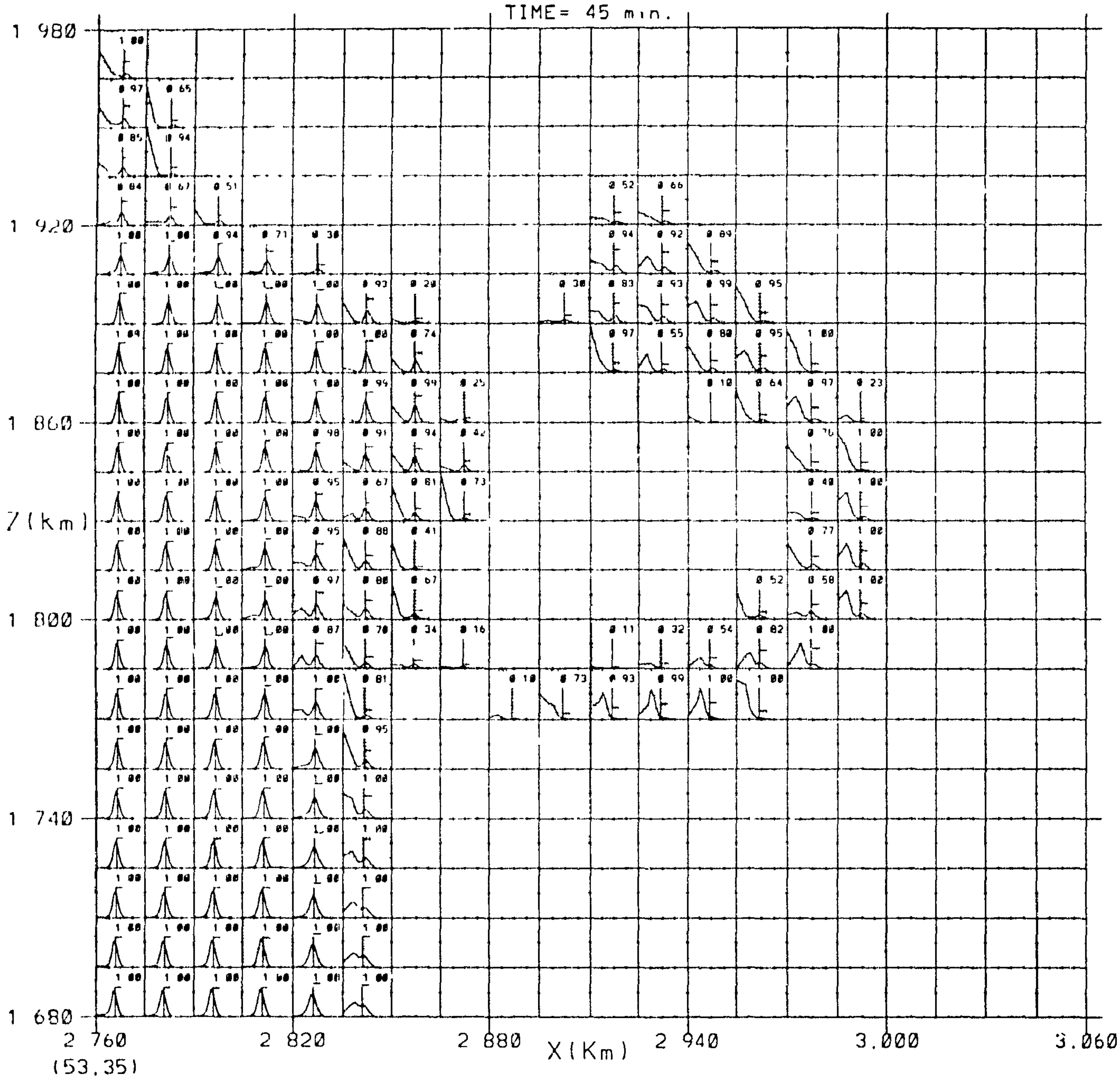

Figure 39: B^2–distributions at $t = 45min.$ for upper downshear portion of cloud.

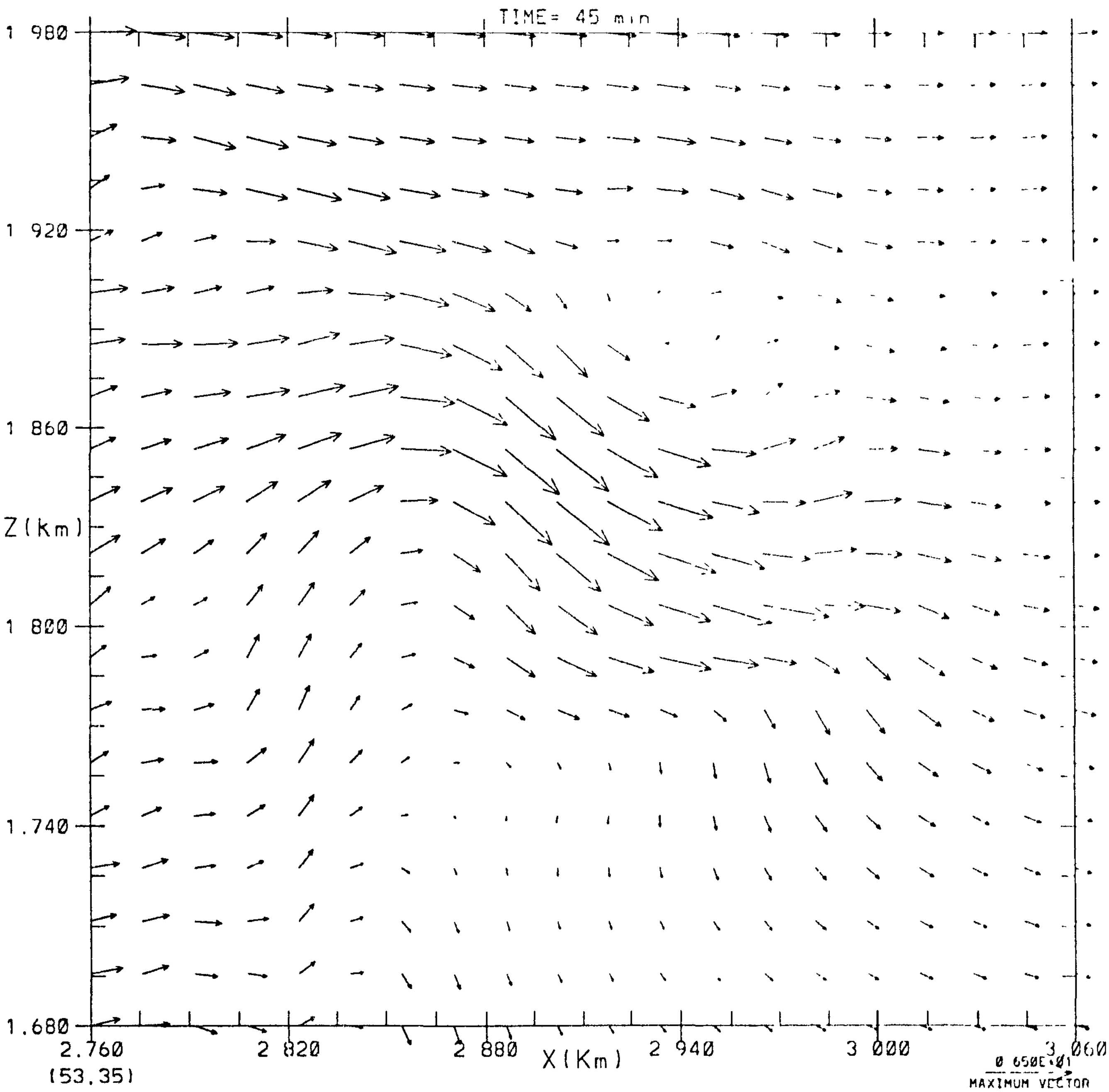

Figure 40: Velocity vectors for domain of figure 39.

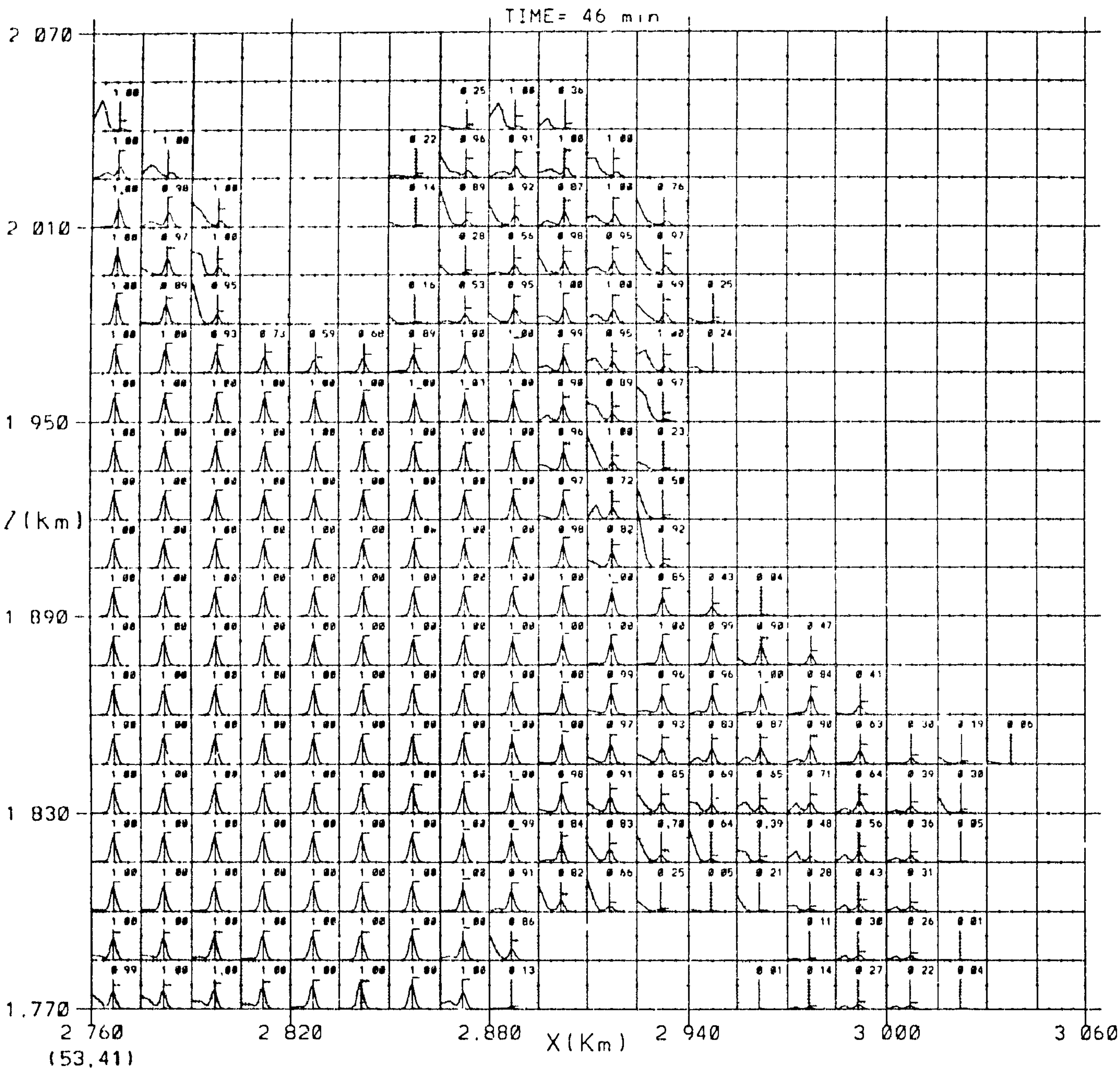

Figure 41: B^2–distributions at $t = 46min.$ for upper downshear portion of cloud.

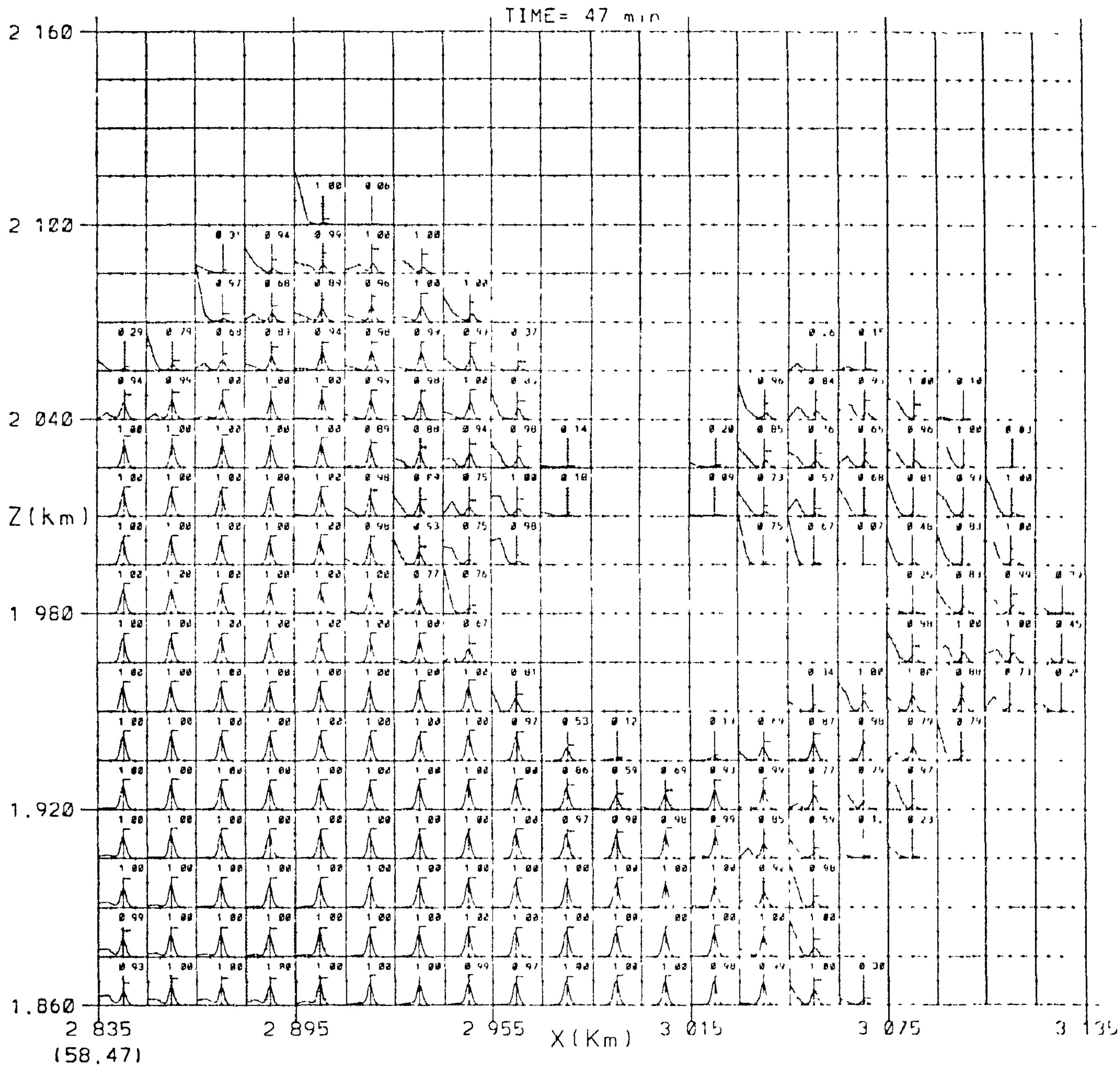

Figure 42: B^2–distributions at $t = 47min$. for upper downshear portion of cloud.

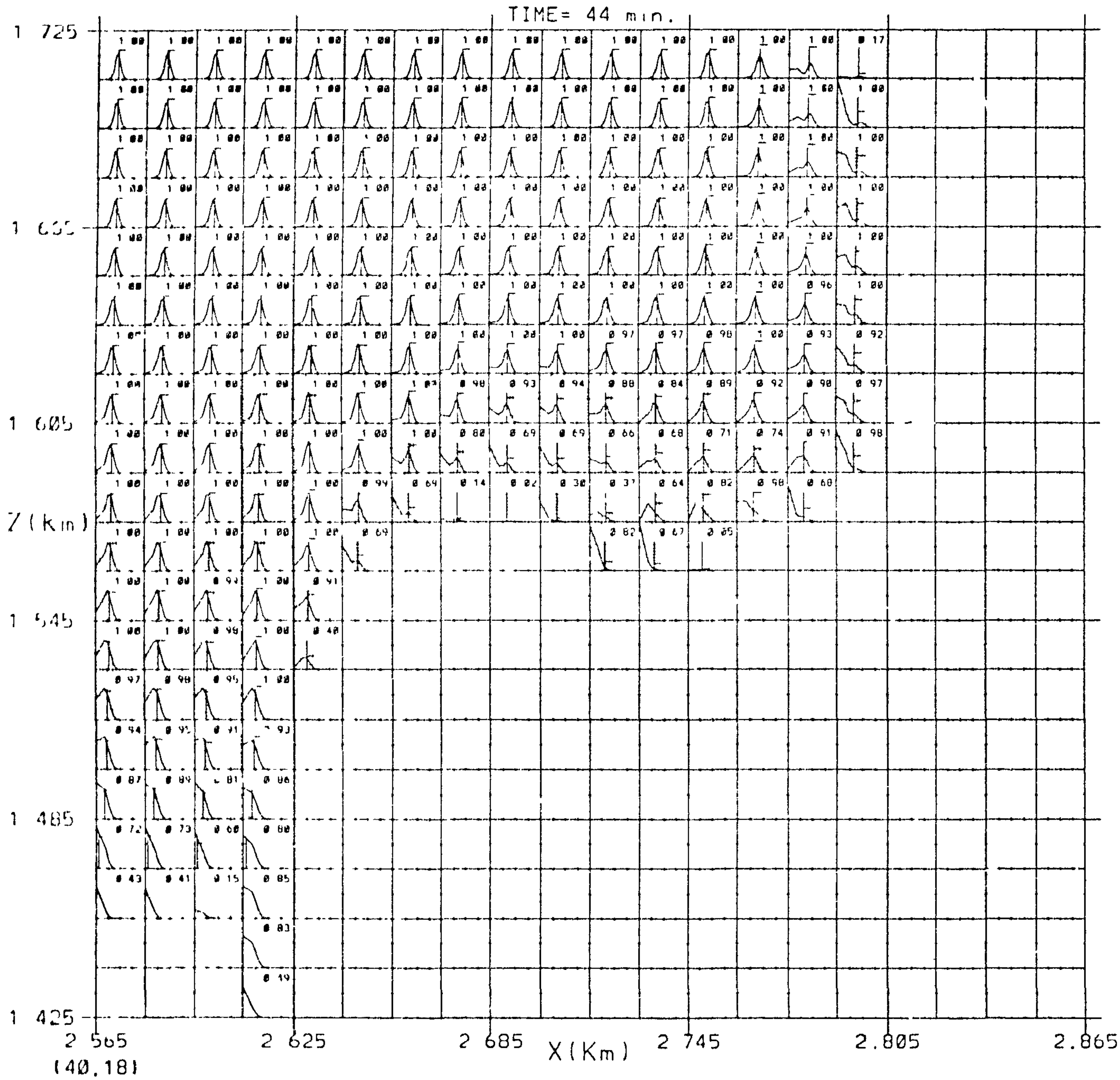

Figure 43: B^2-distributions at $t = 44min.$ for lower downshear portion of cloud.

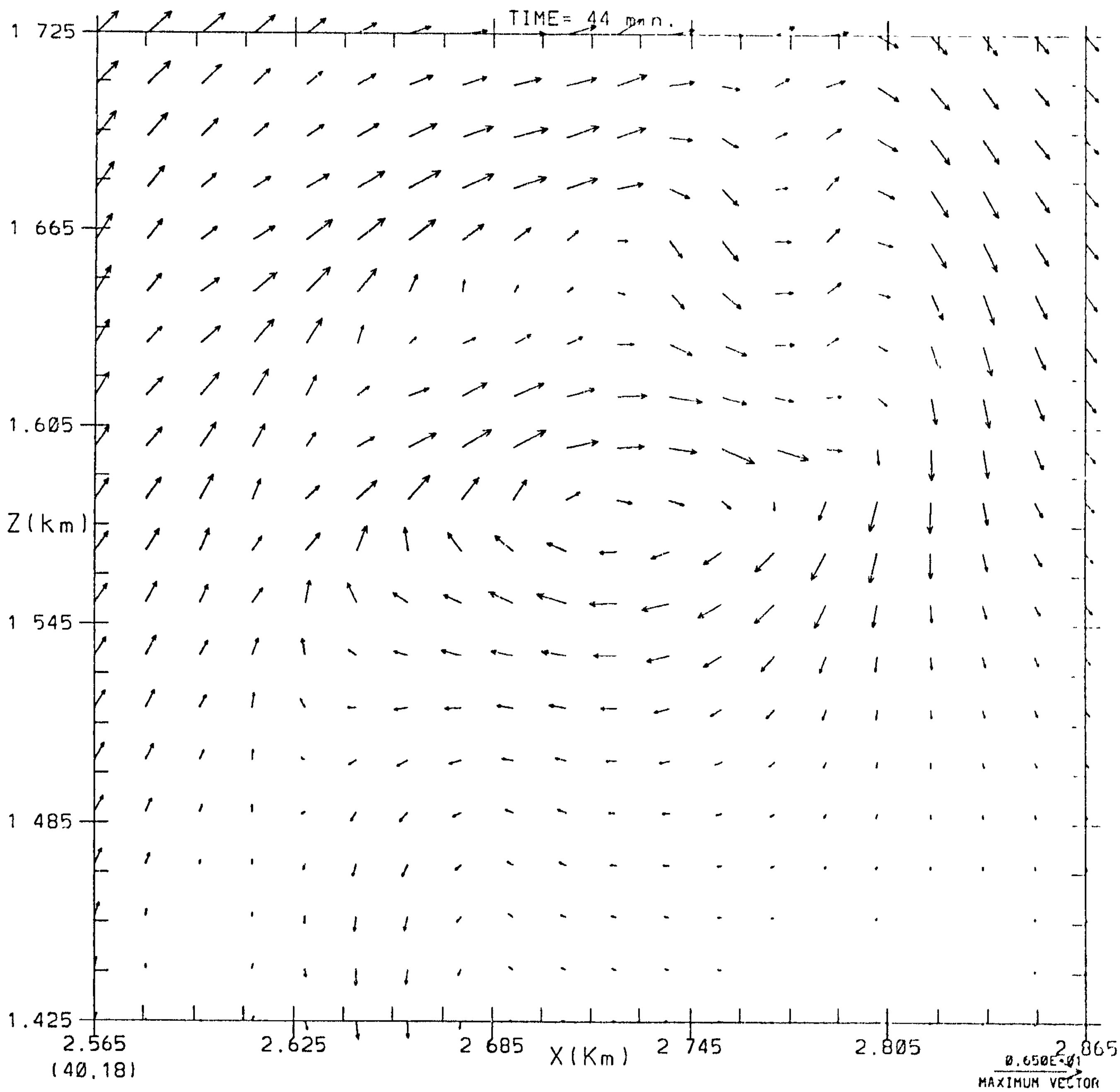

Figure 44: Velocity vectors for domain of figure 43.

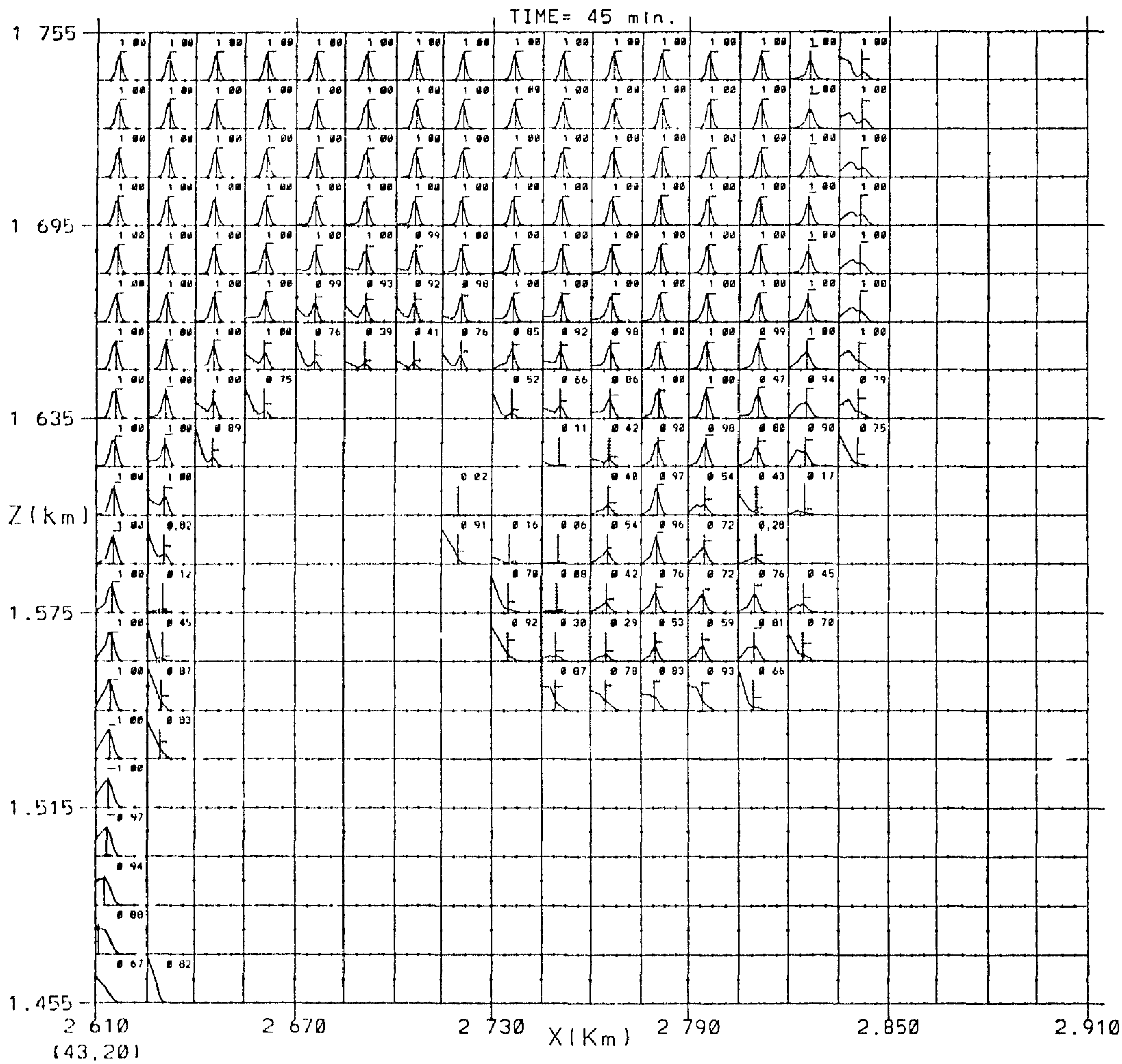

Figure 45: B^2-distributions at $t = 45min.$ for lower downshear portion of cloud.

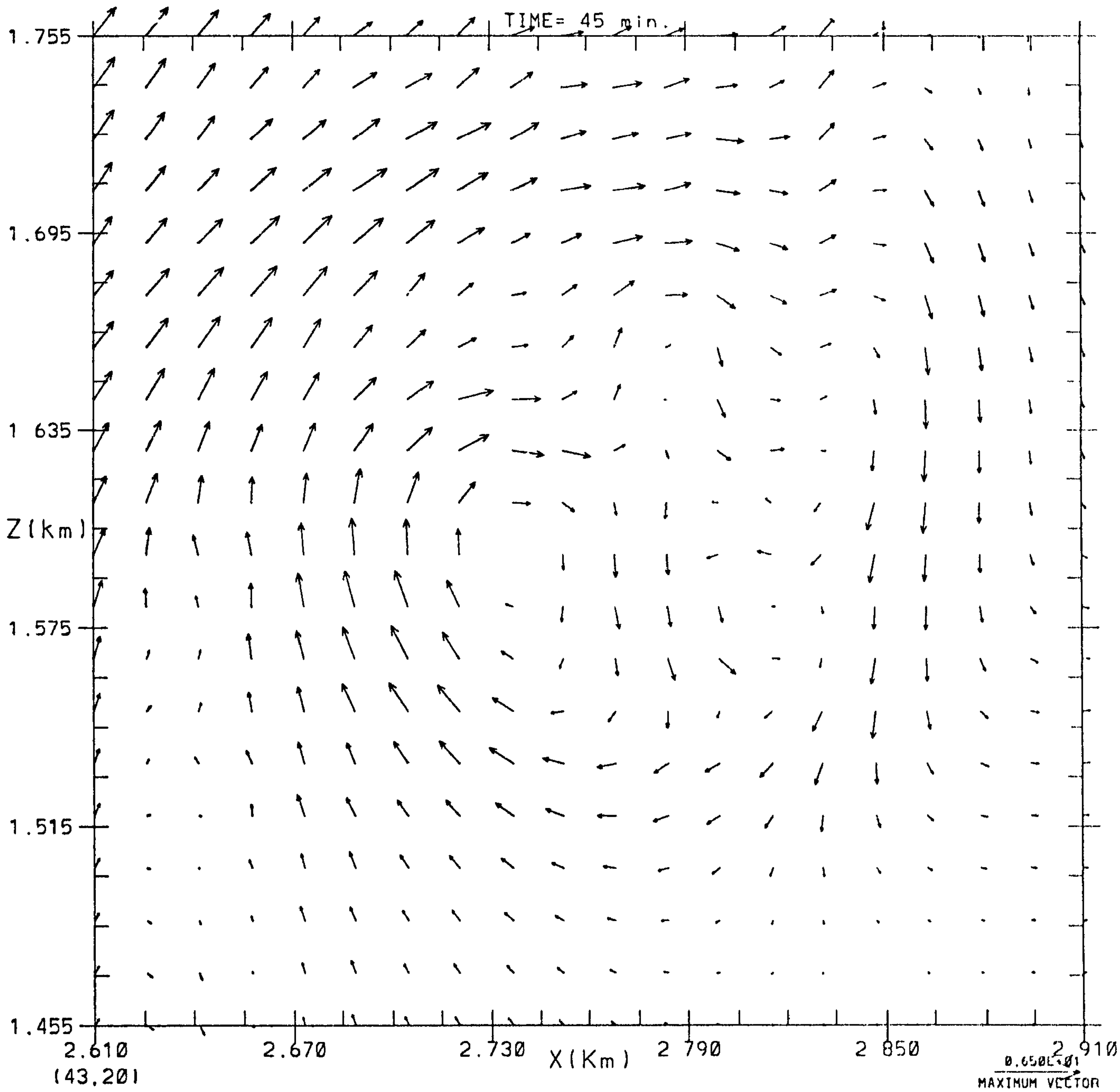

Figure 46: Velocity vectors for domain of figure 45.

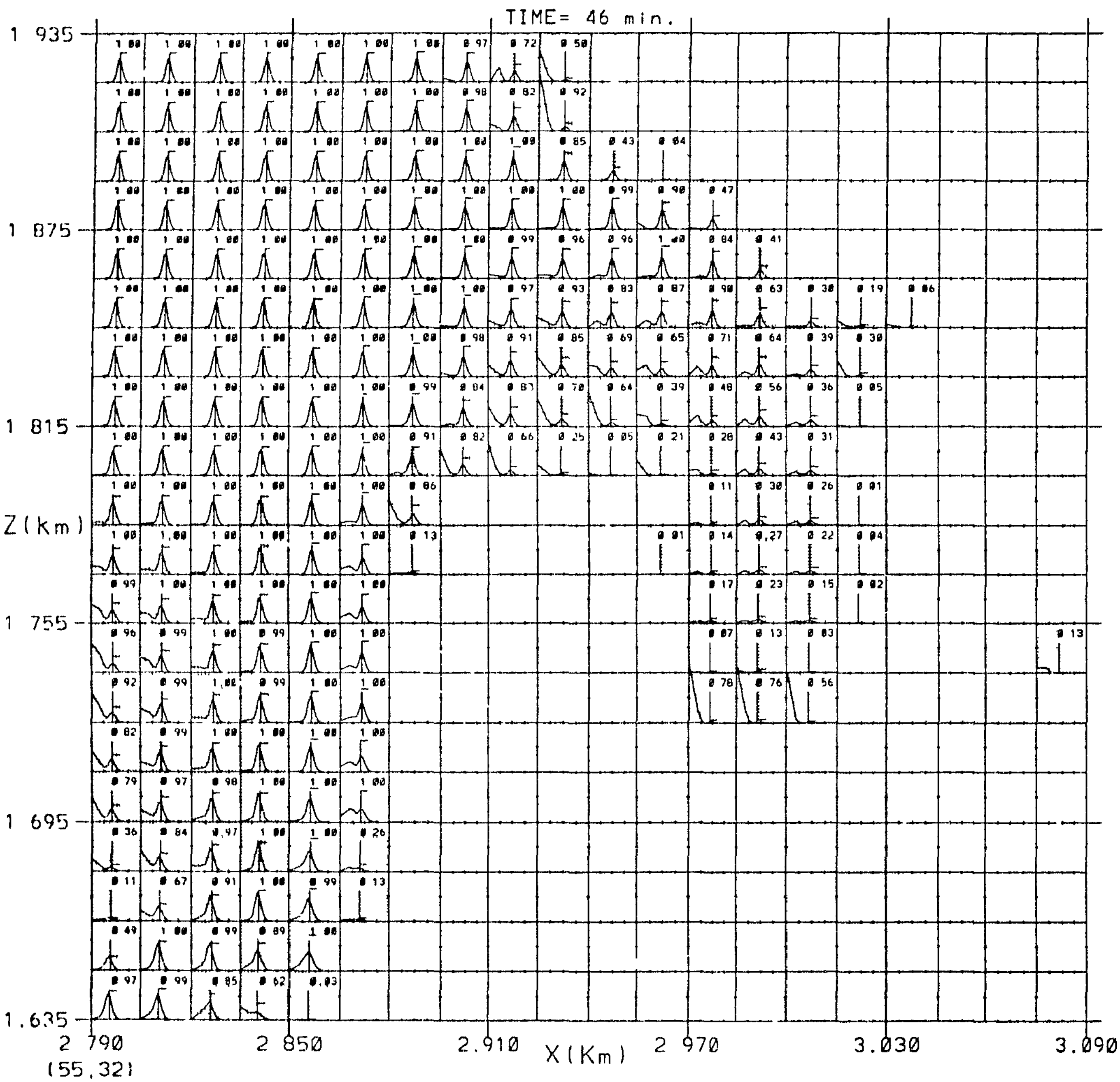

Figure 47: B^2–distributions at $t = 46min.$ for middle of downshear portion of cloud.

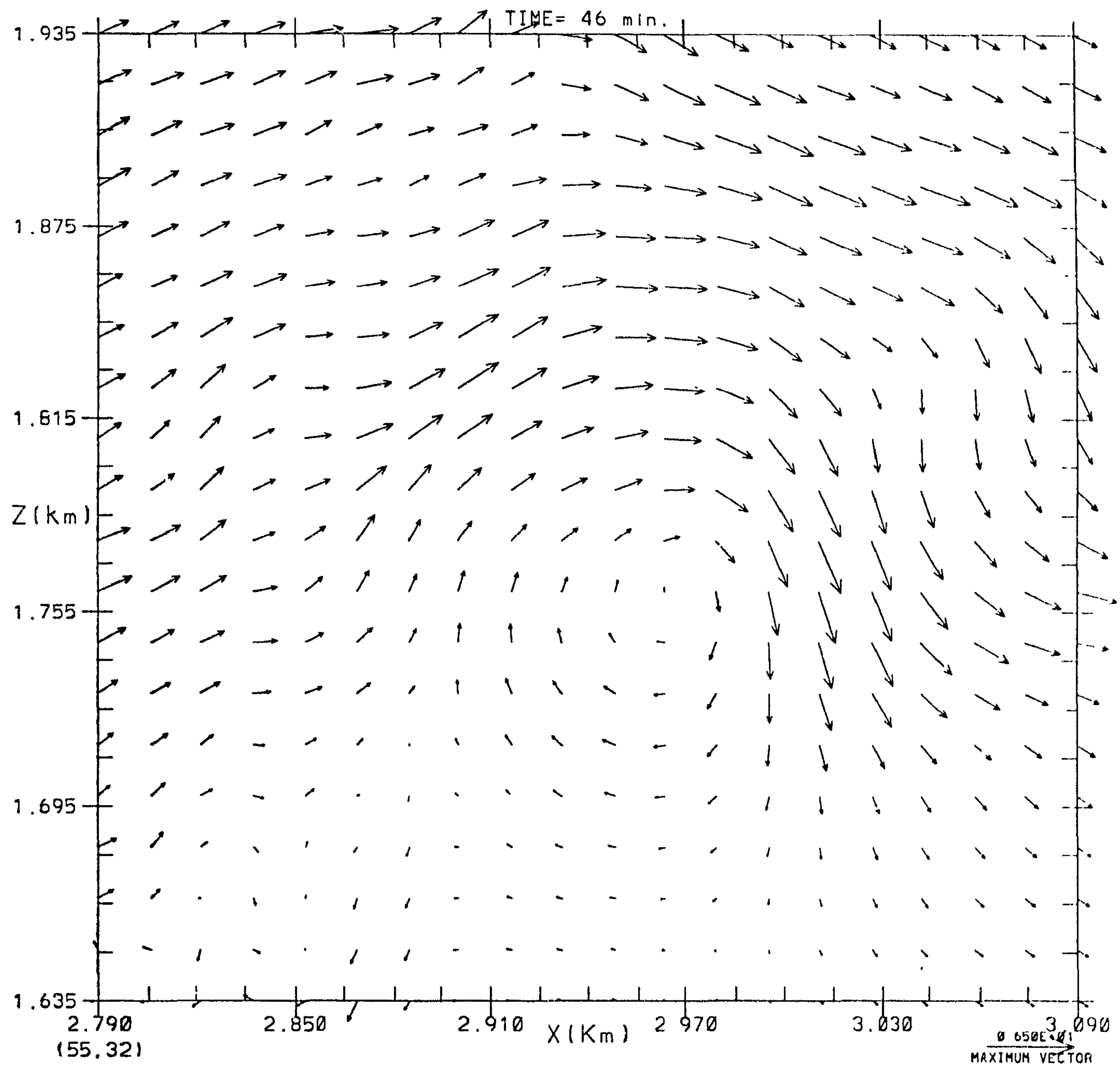

Figure 48: Velocity vectors for domain of figure 47.

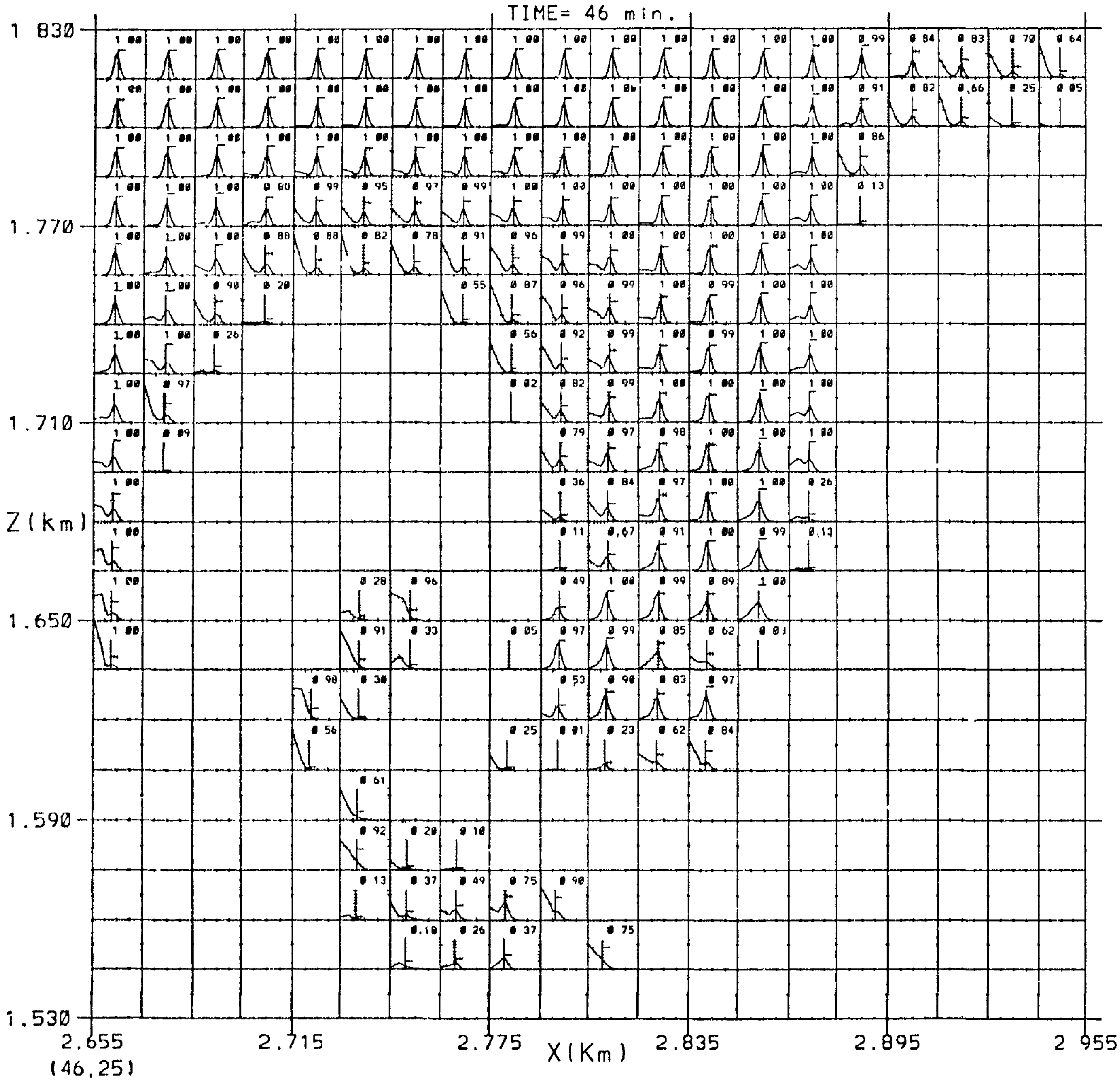

Figure 49: B^2–distributions at $t = 46min.$ for lower downshear portion of cloud.

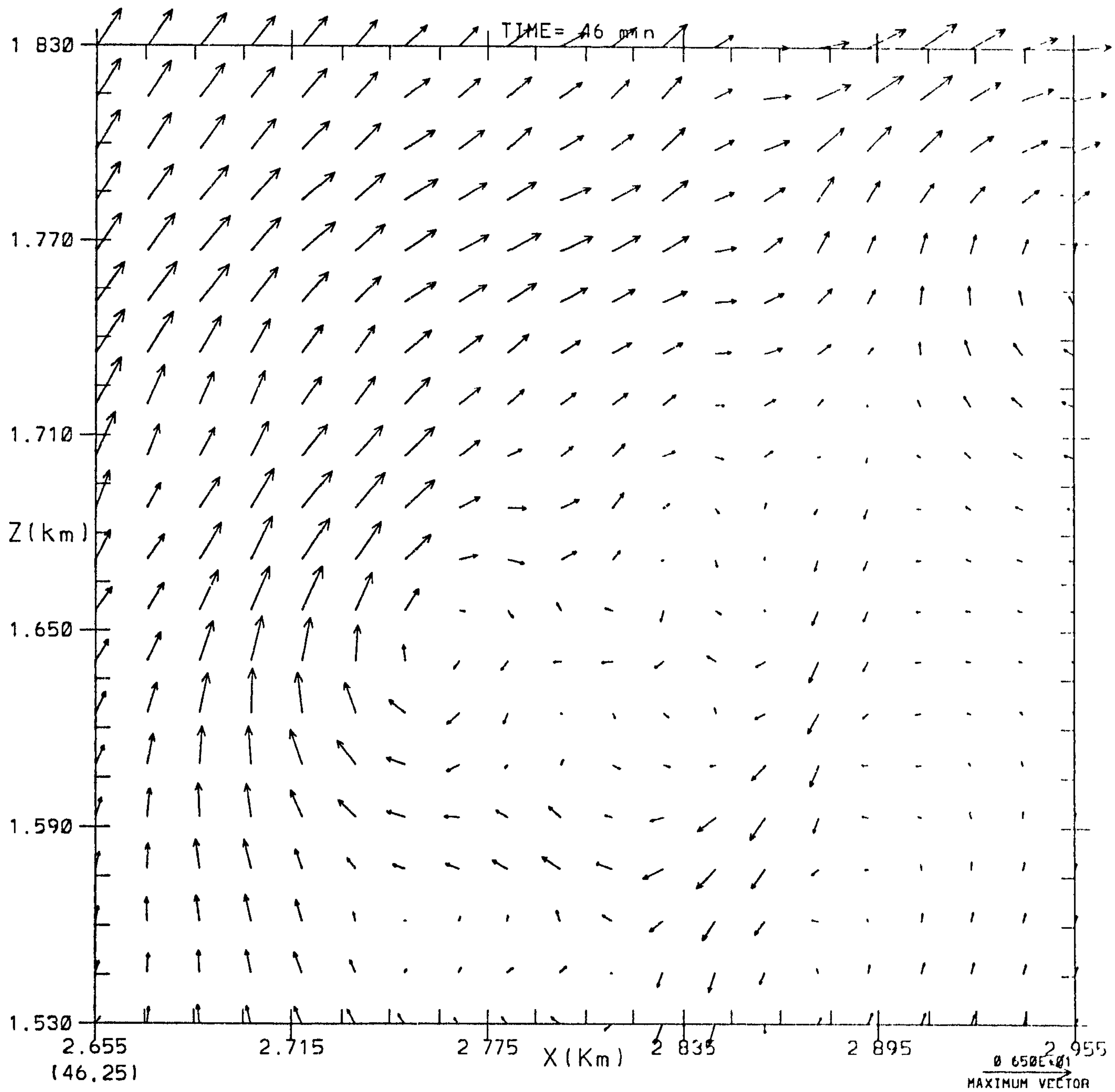

Figure 50: Velocity vectors for domain of figure 49.

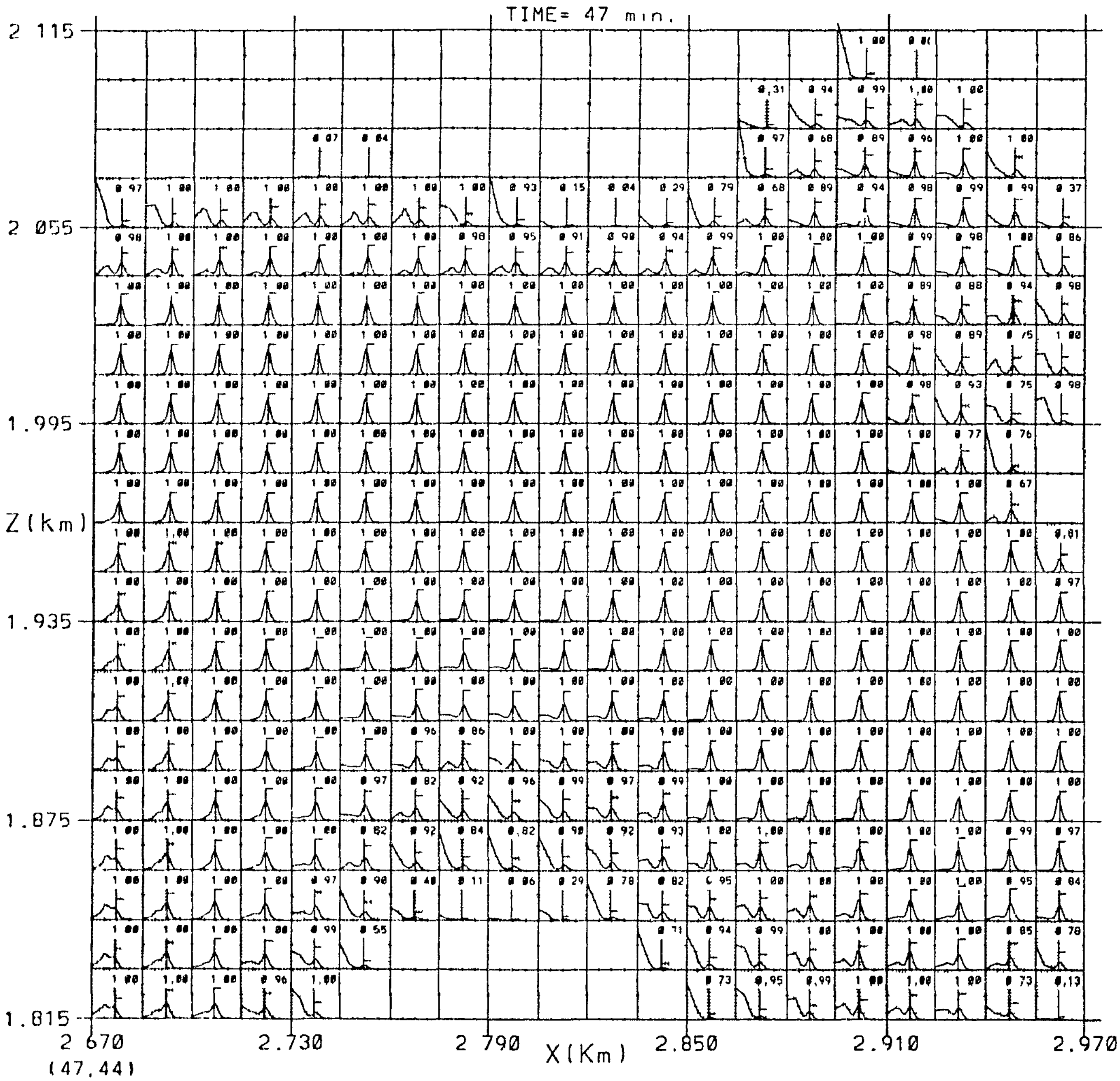

Figure 51: B^2–distributions at $t = 47min.$ for cloud core.

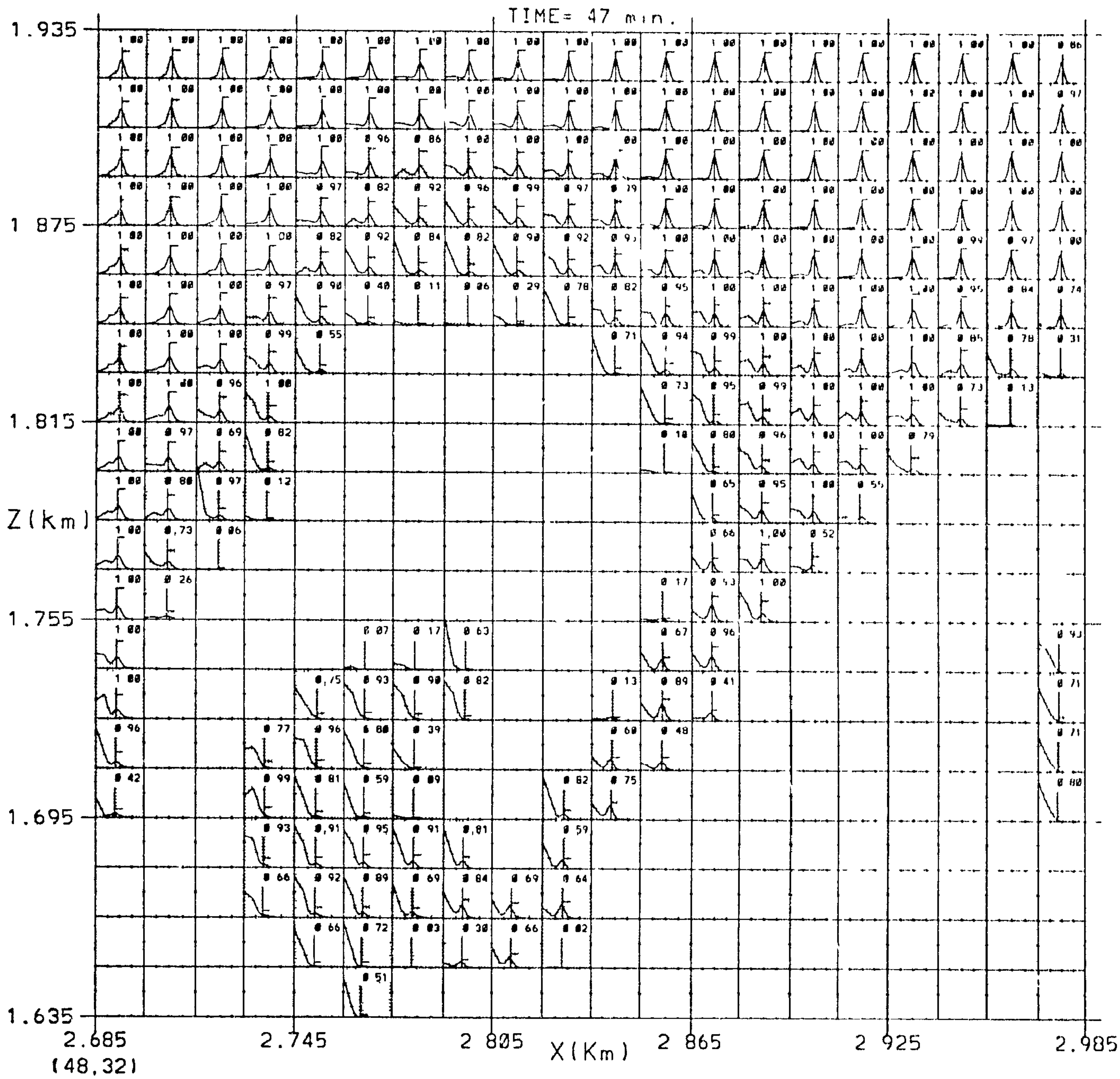

Figure 52: B^2–distributions at $t = 47min.$ for lower downshear portion of cloud.

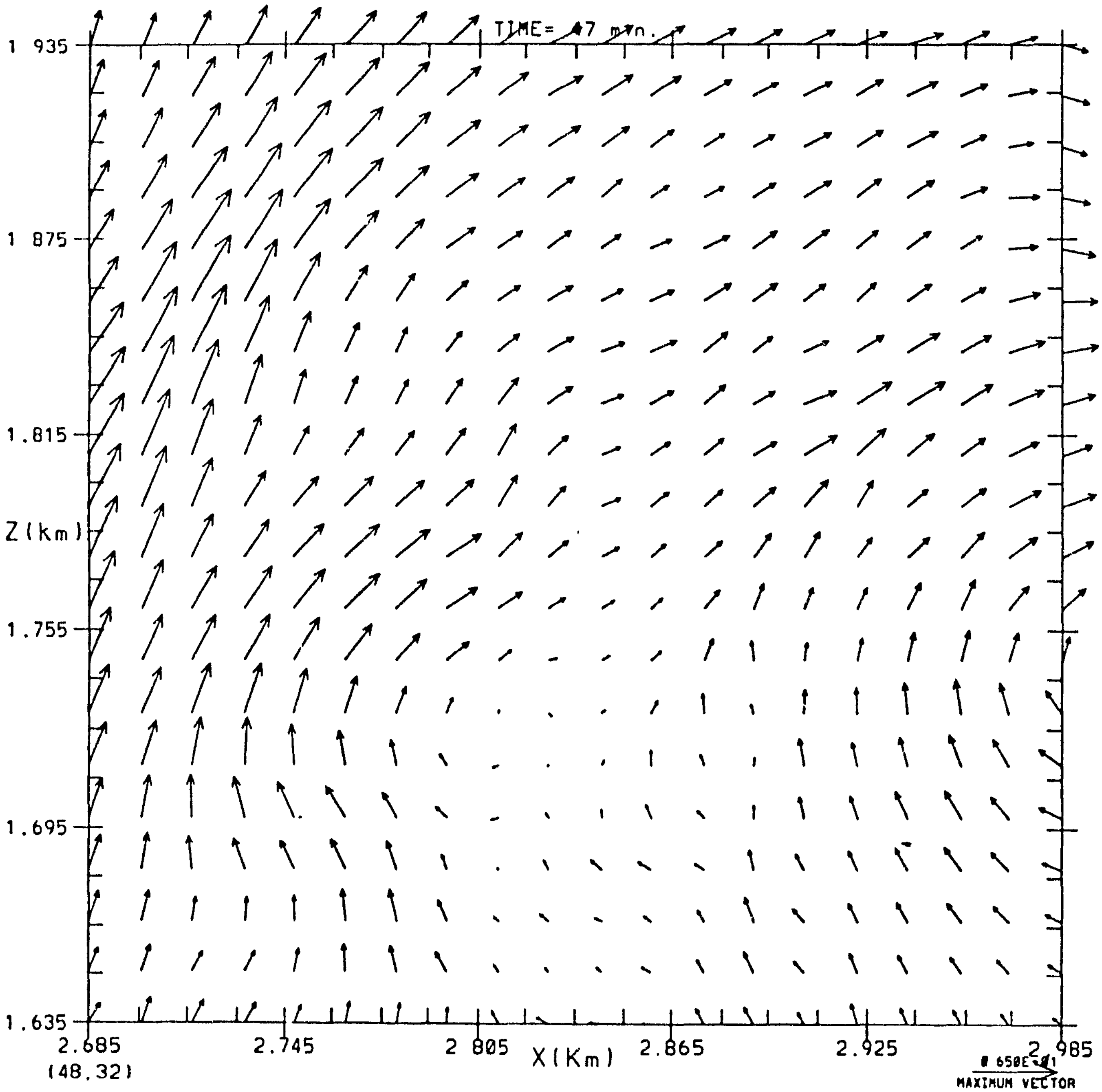

Figure 53: Velocity vectors for domain of figure 52.

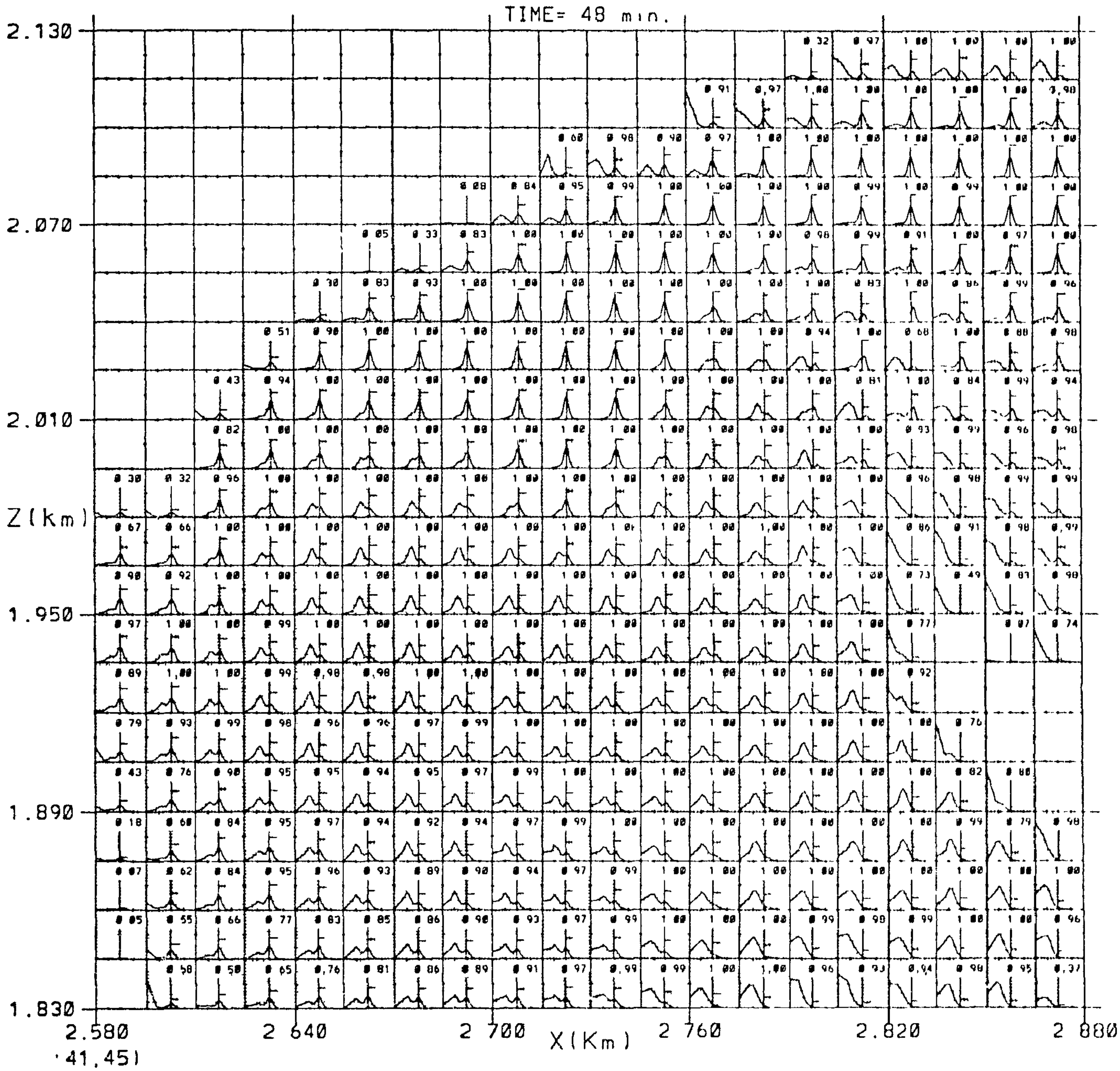

Figure 54: B^2–distributions at $t = 48min.$ for upshear portion of cloud.

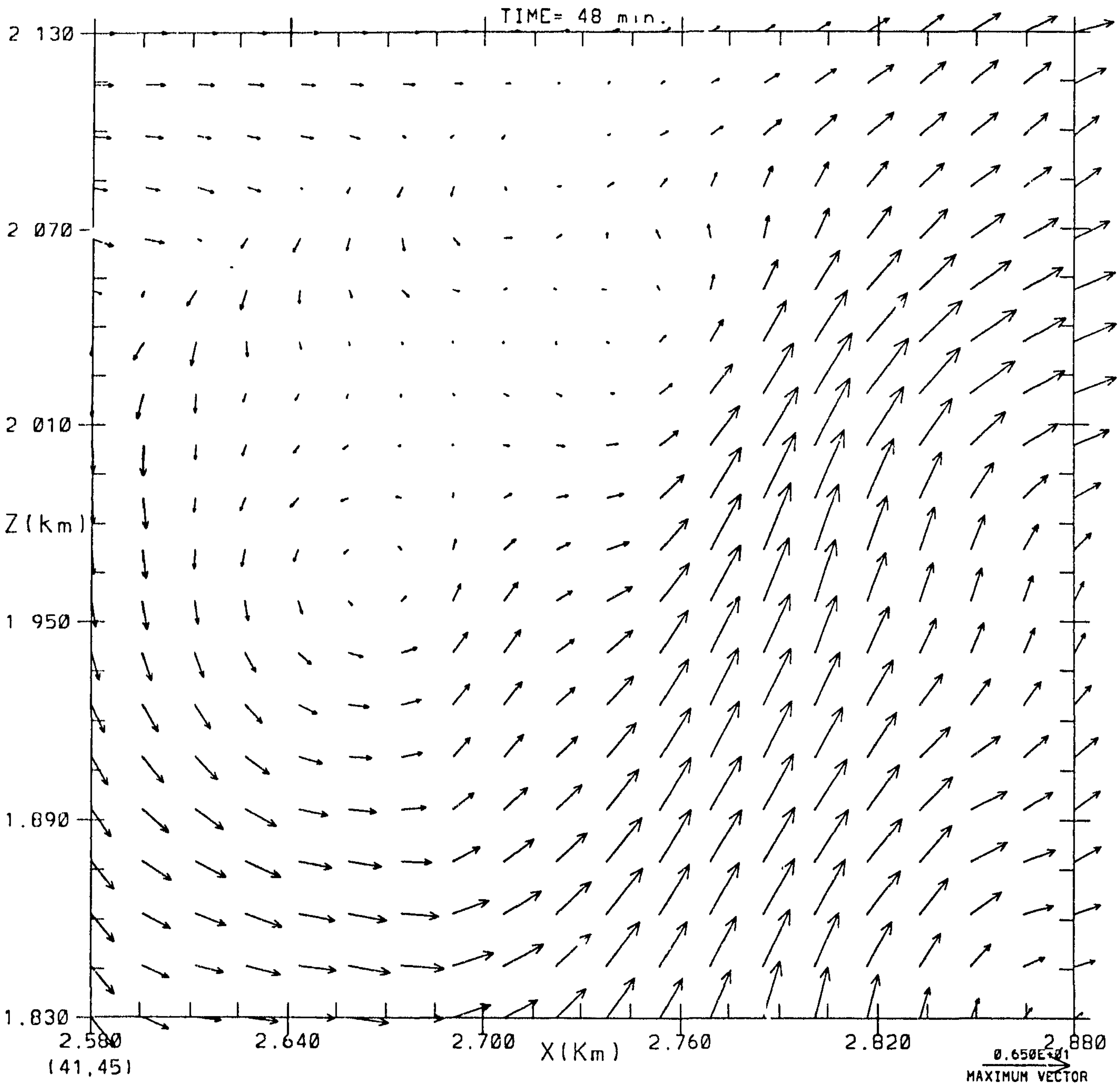

Figure 55: Velocity vectors for domain of figure 54.

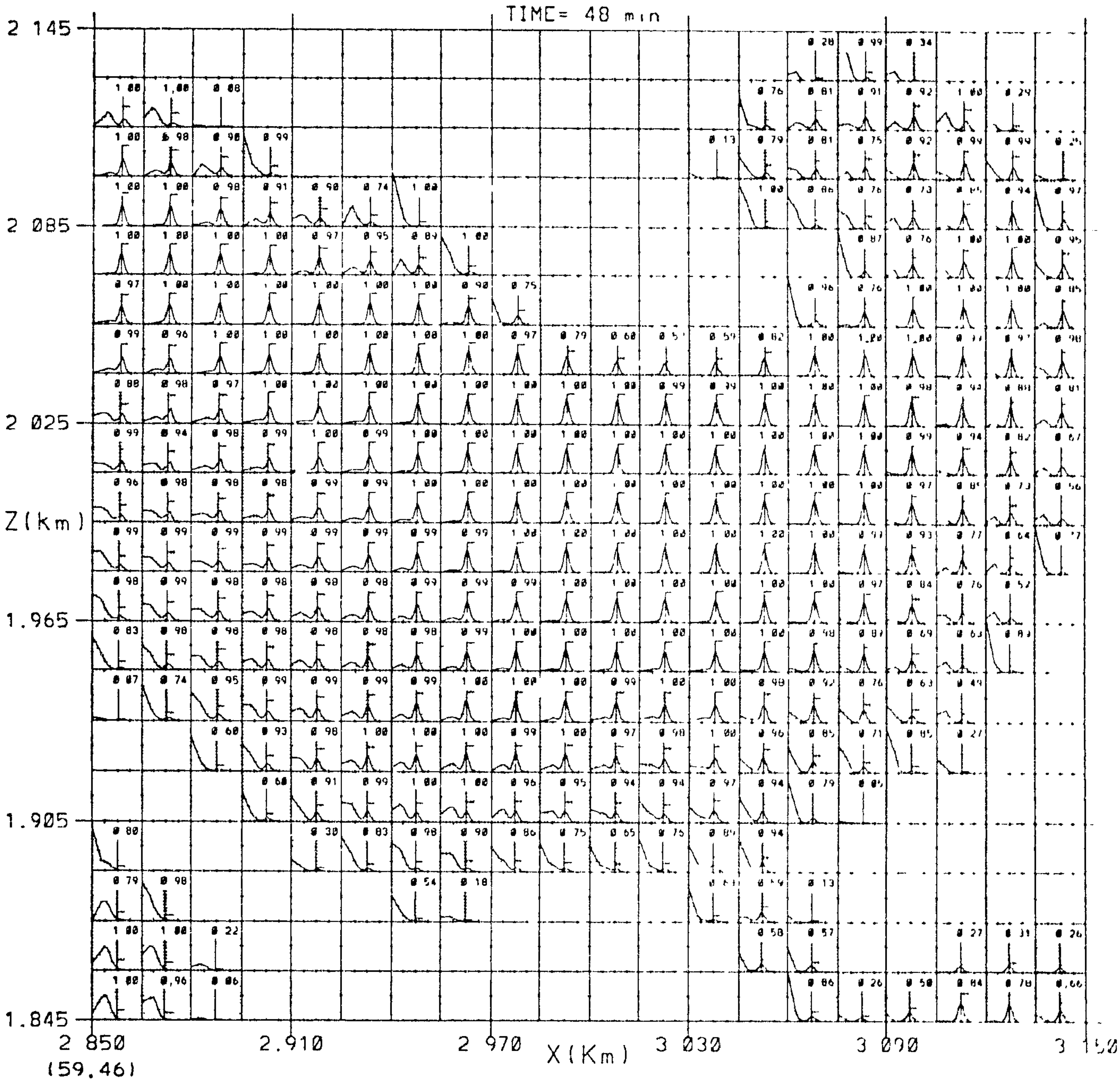

Figure 56: B^2–distributions at $t = 48min.$ for downshear portion of cloud.

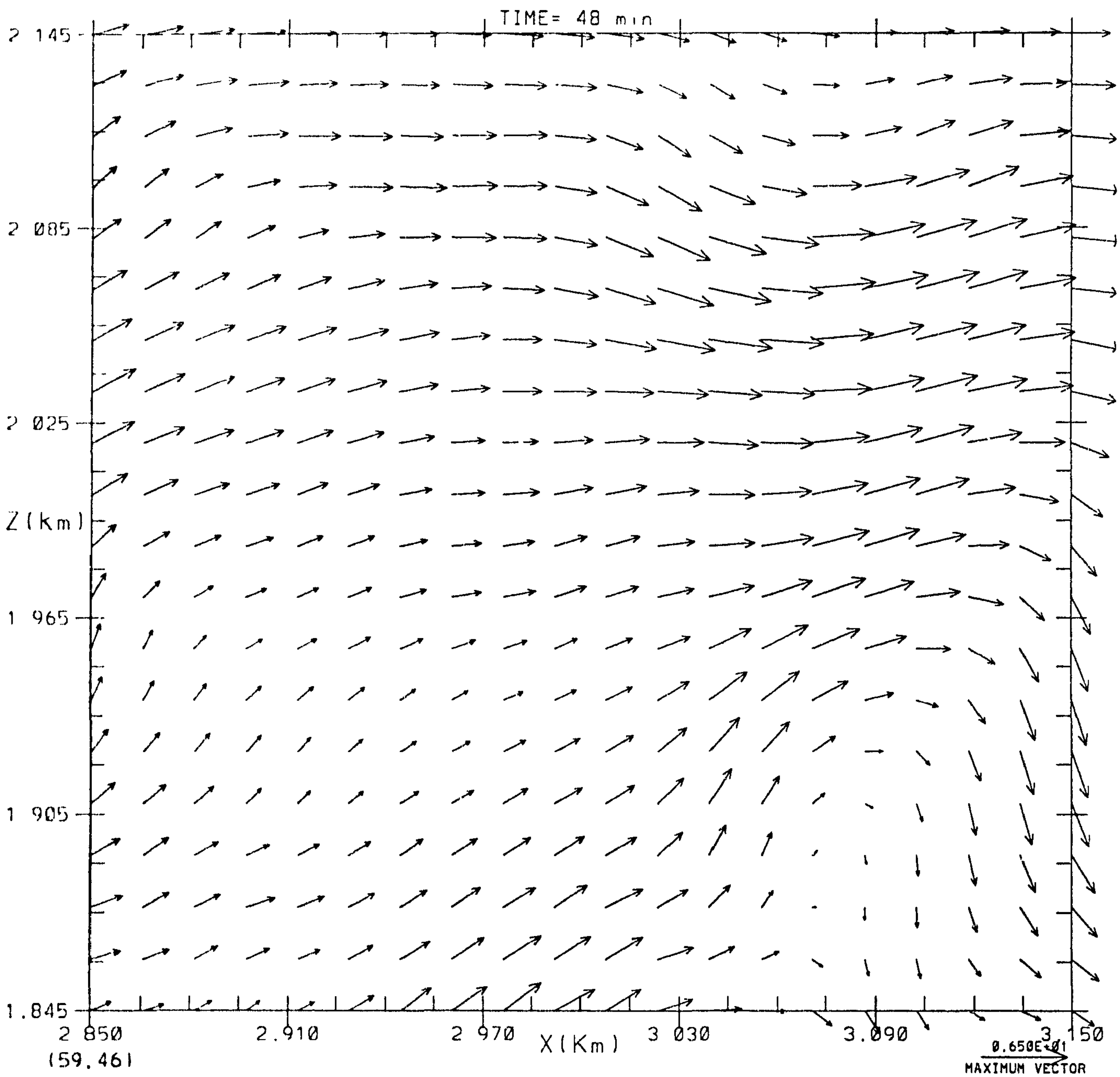

Figure 57: Velocity vectors for domain of figure 56.

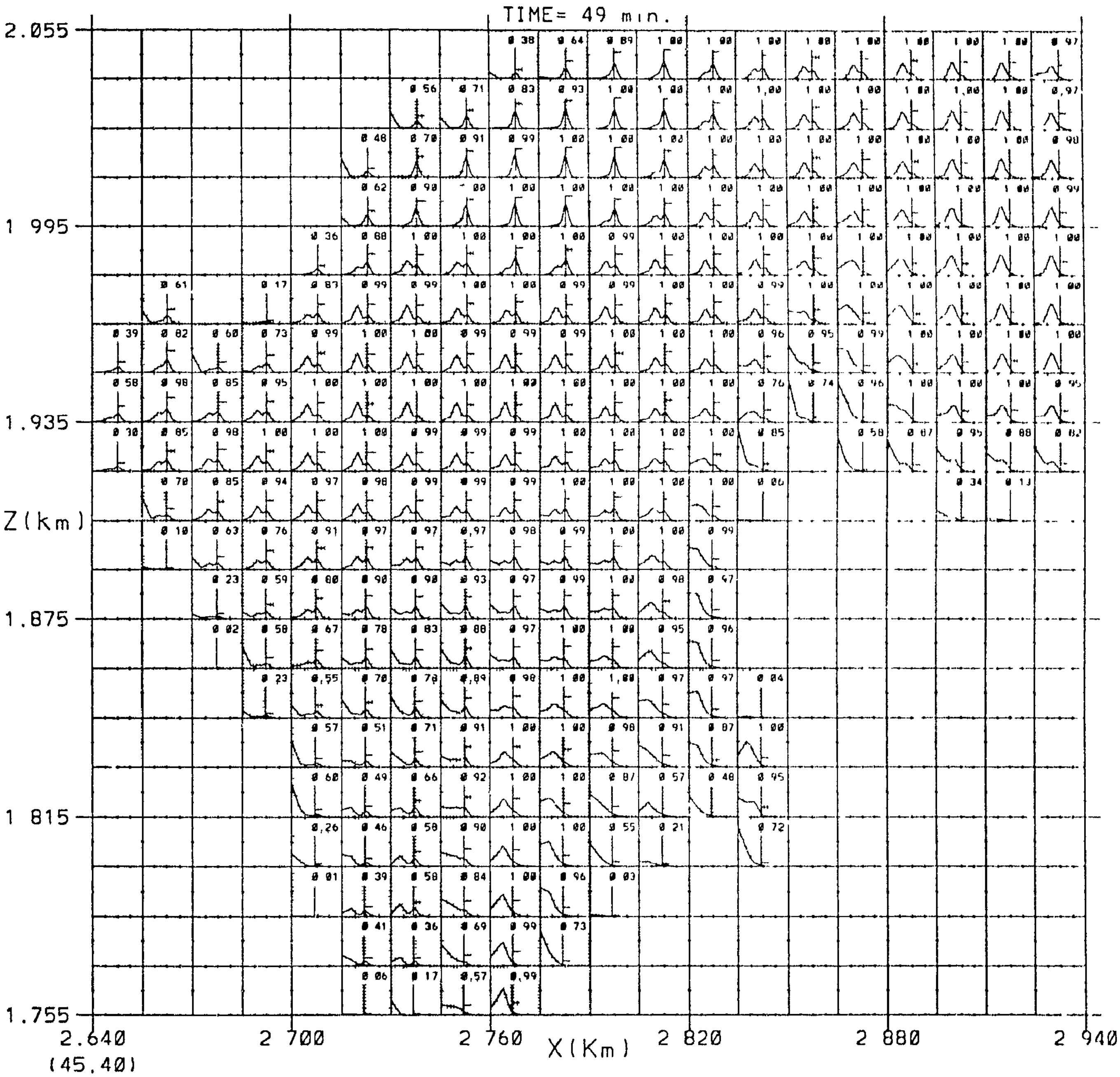

Figure 58: B^2–distributions at $t = 49 min.$ for left portion of cloud.

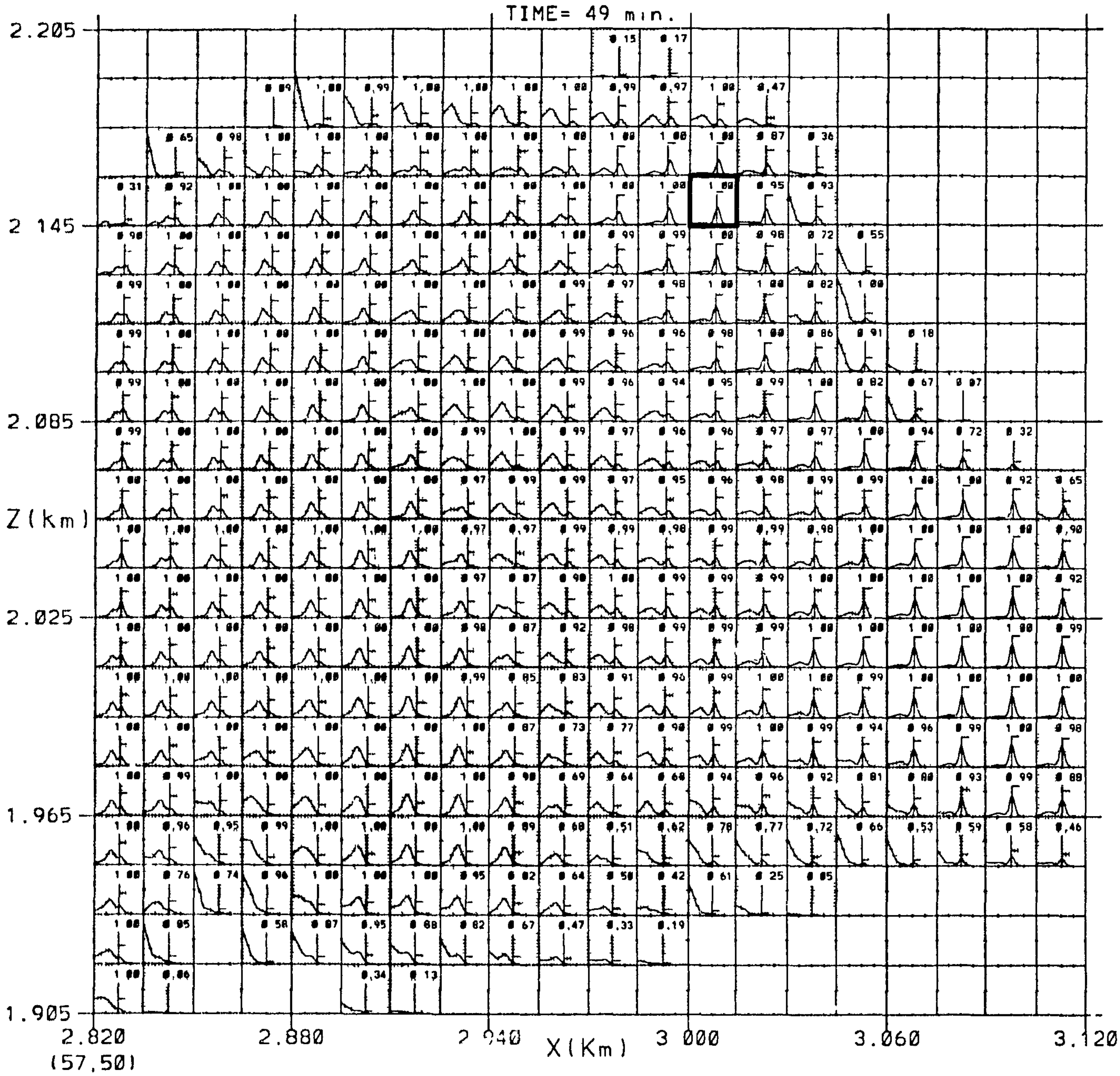

Figure 59: B^2-distributions at $t = 49min.$ for middle portion of cloud.

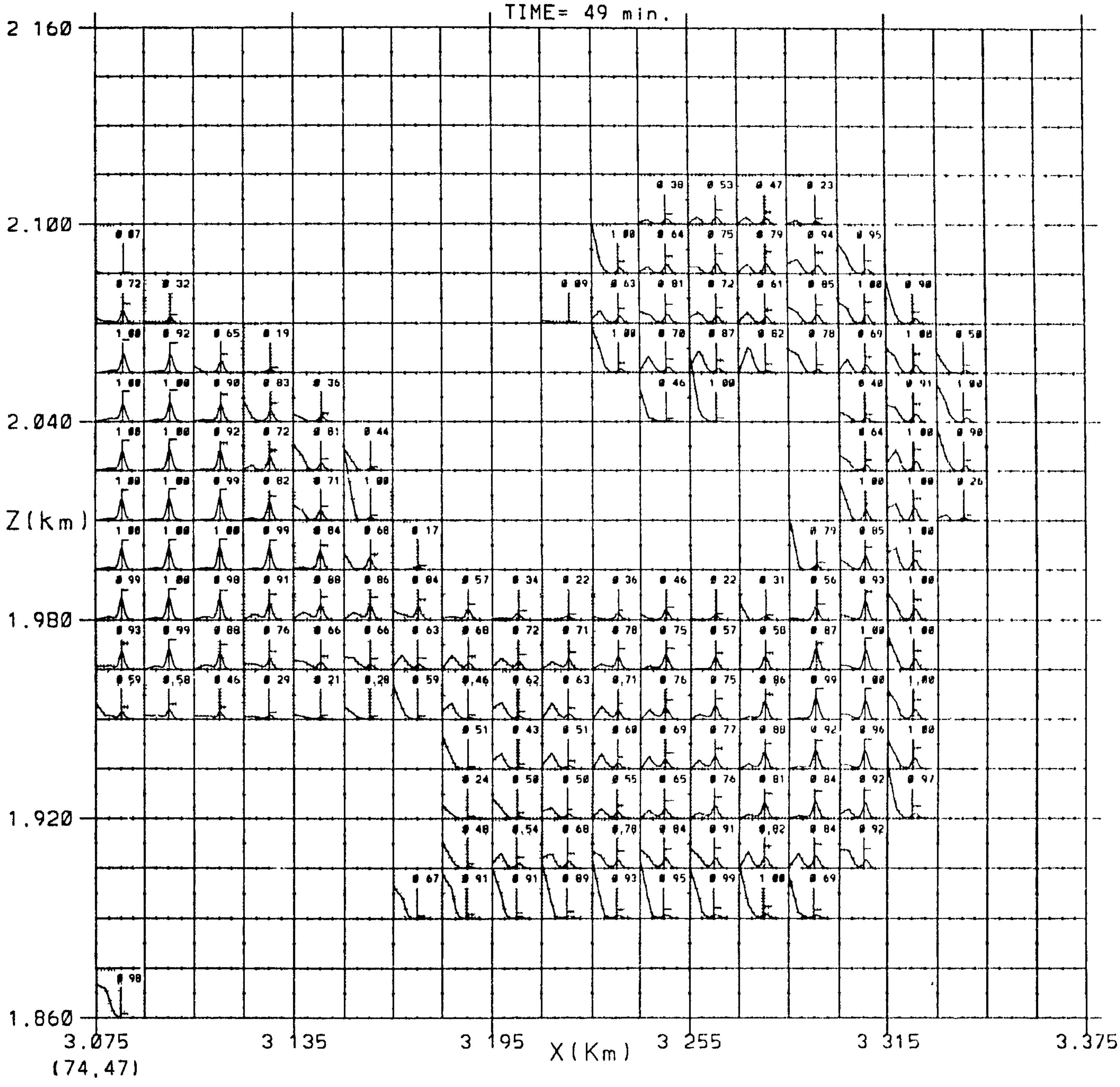

Figure 60: B^2–distributions at $t = 49min.$ for right portion of cloud.

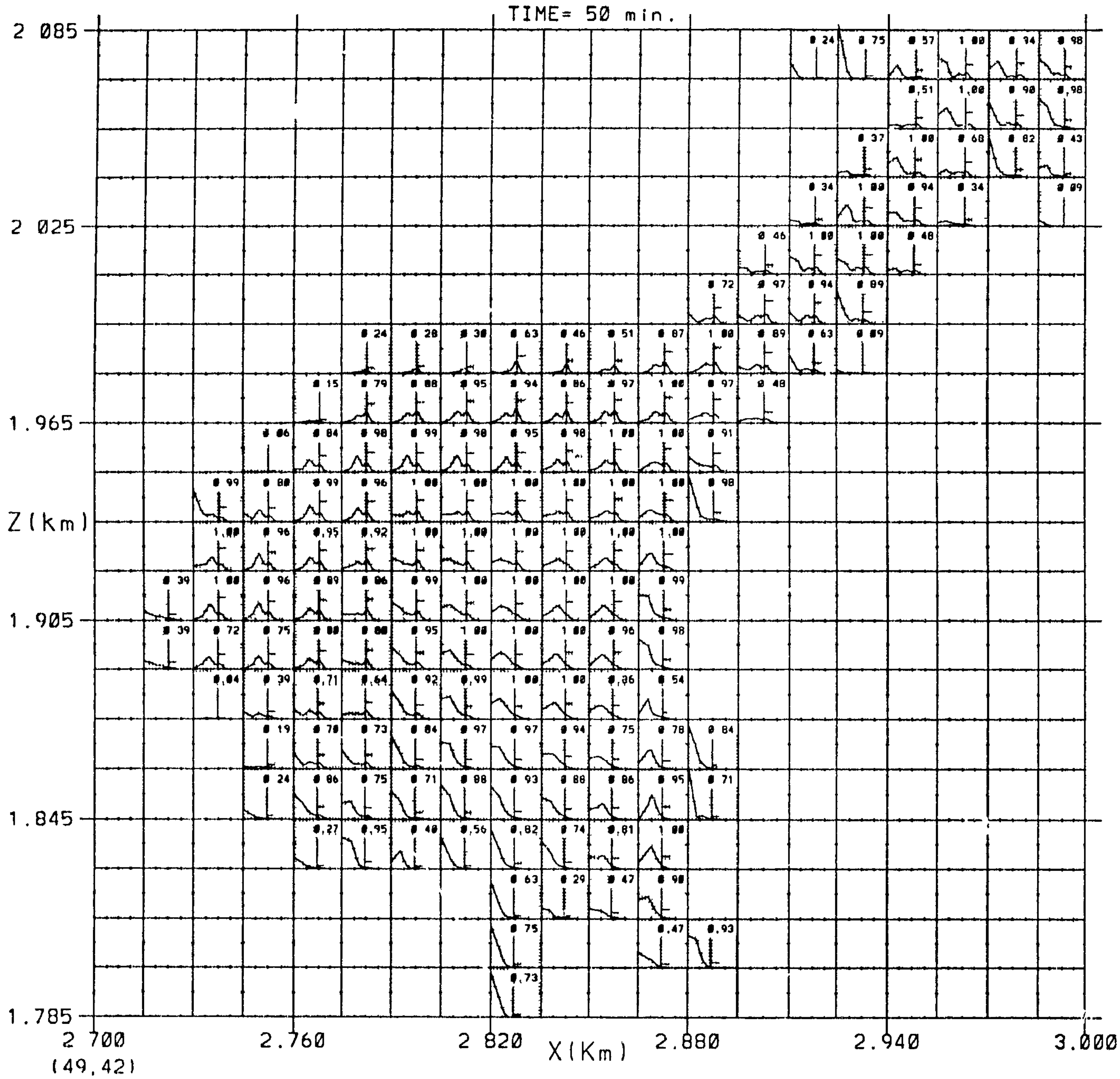

Figure 61: B^2–distributions at $t = 50min.$ for left portion of cloud.

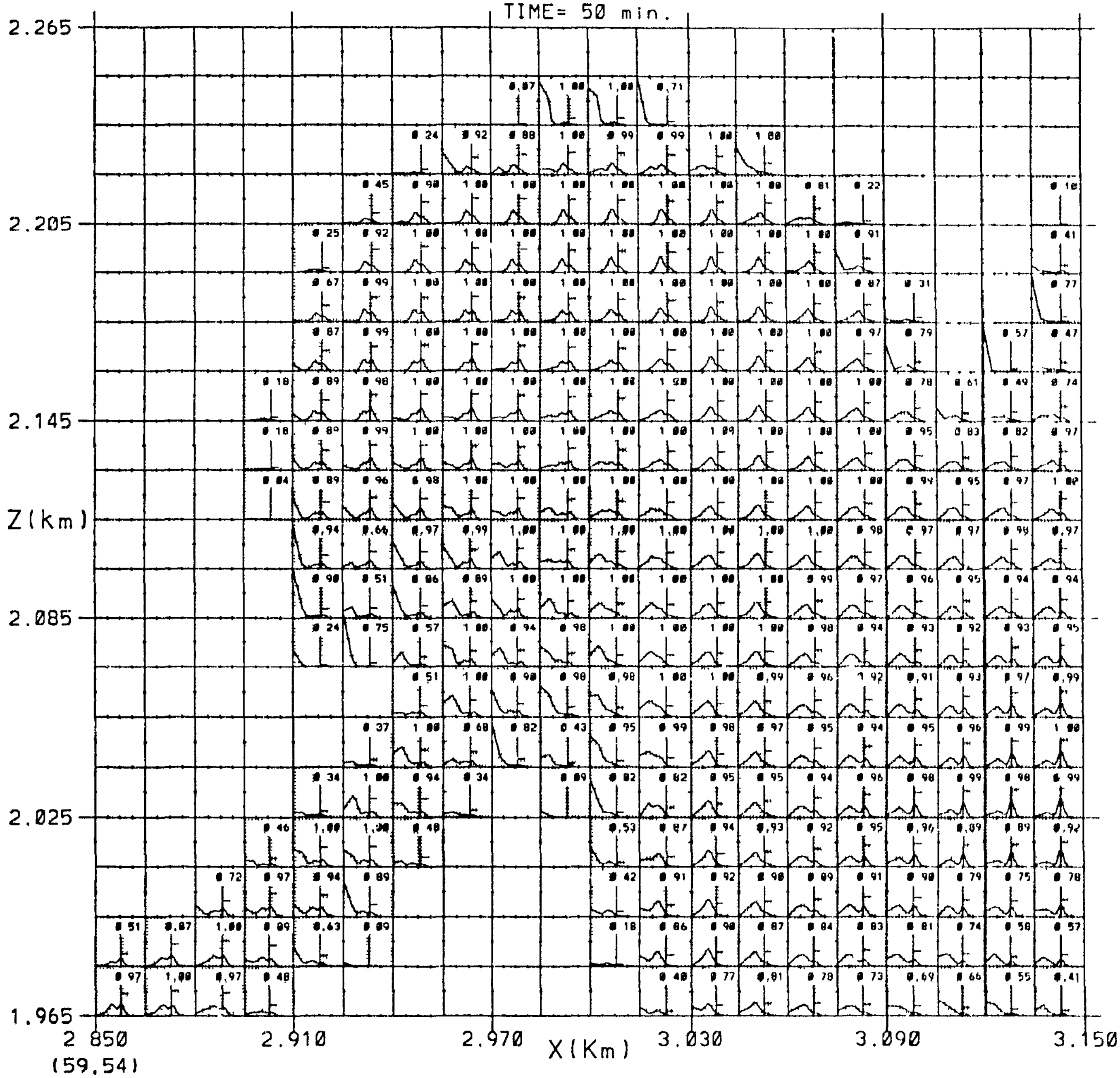

Figure 62: B^2–distributions at $t = 50min.$ for middle portion of cloud.

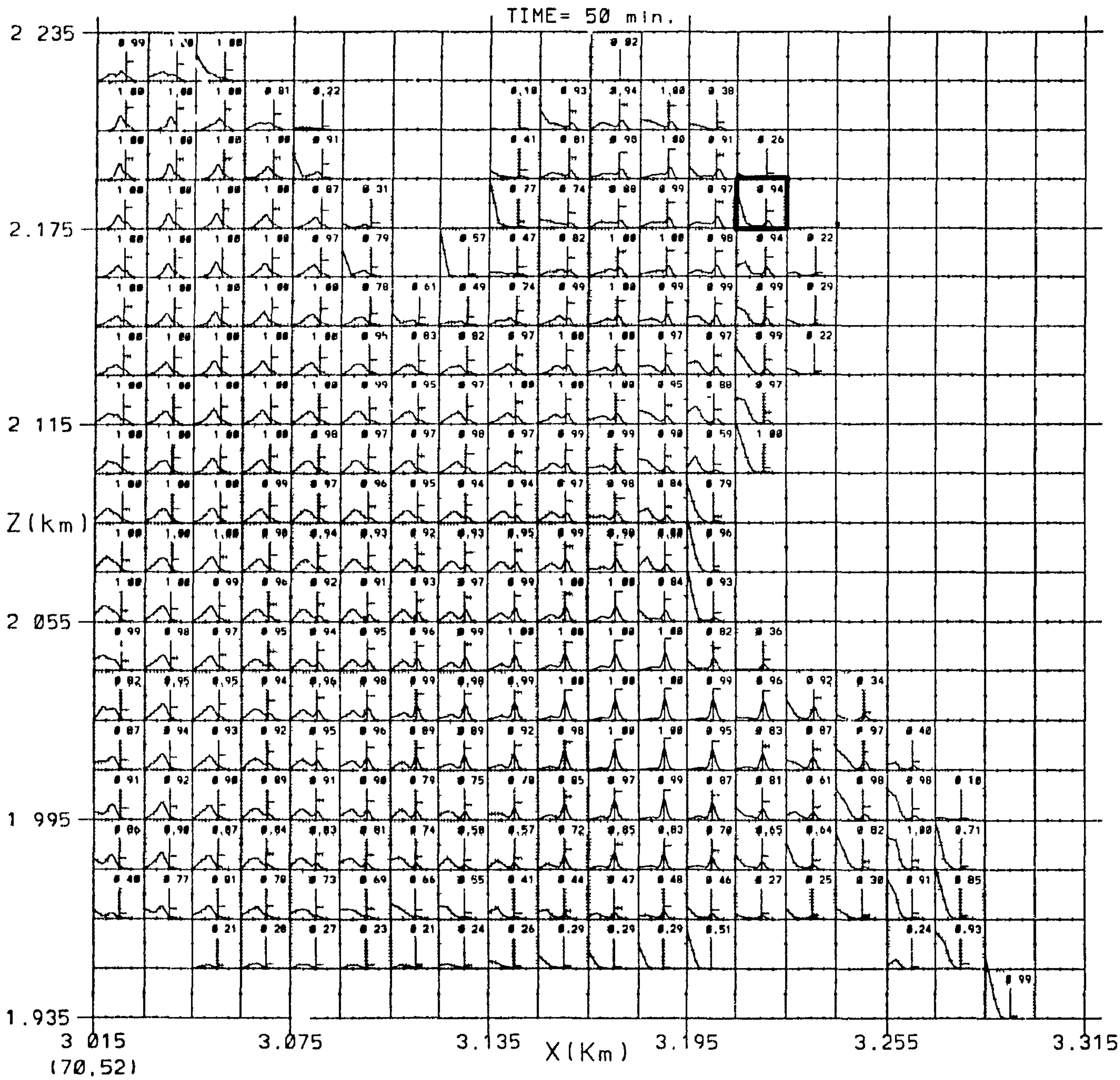

Figure 63: B^2–distributions at $t = 50min.$ for right portion of cloud.

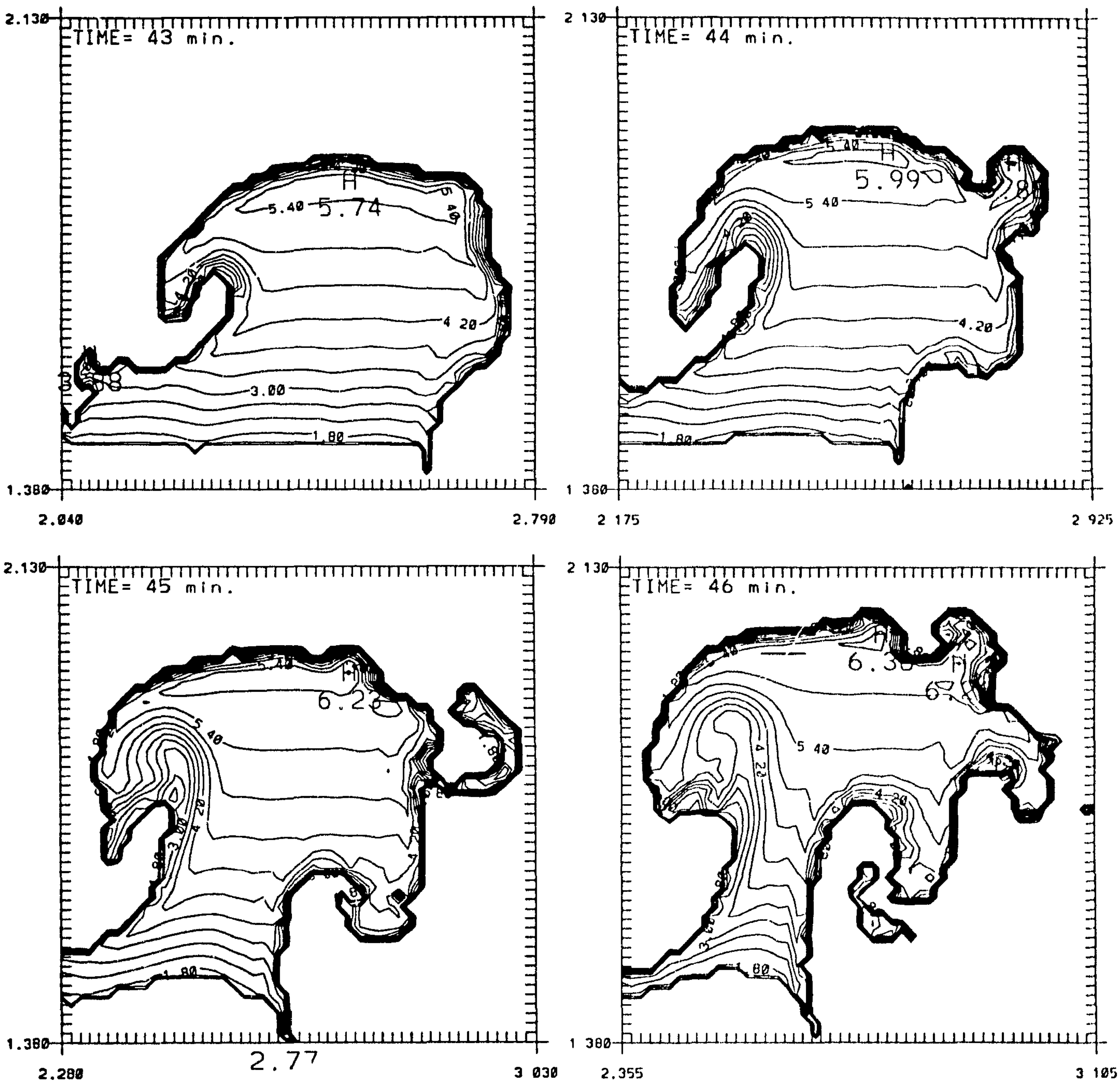

Figure 64: Average radius of size distribution, $\overline{R}$, for $t = 43, 44, 45, 46min.$.
Contour interval of $0.4\mu m$. H indicates high values.

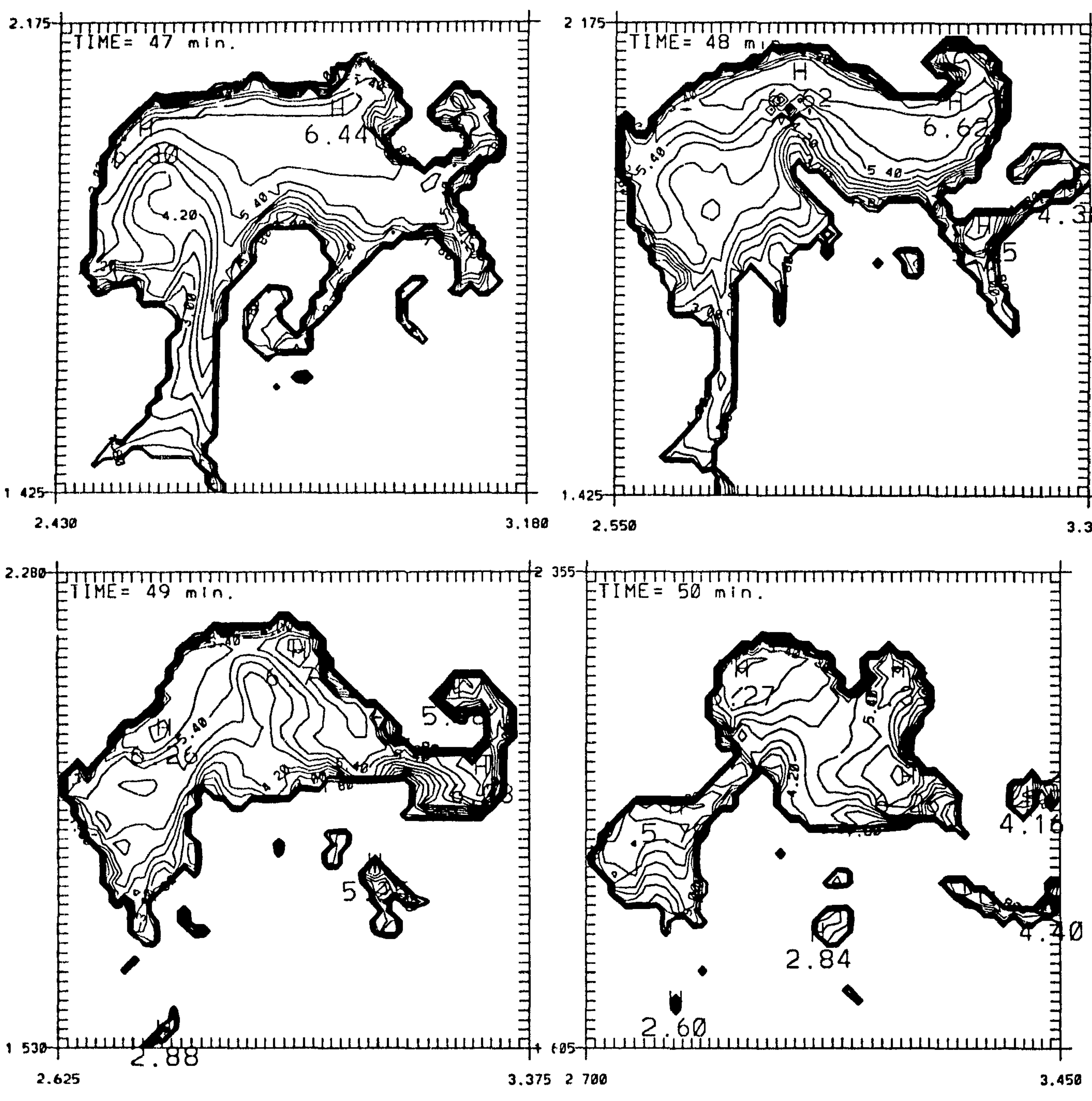

Figure 65: Average radius of size distribution, $\overline{R}$, for $t = 47, 48, 49, 50 min.$. Contour interval of $0.4\mu m$. H indicates high values.

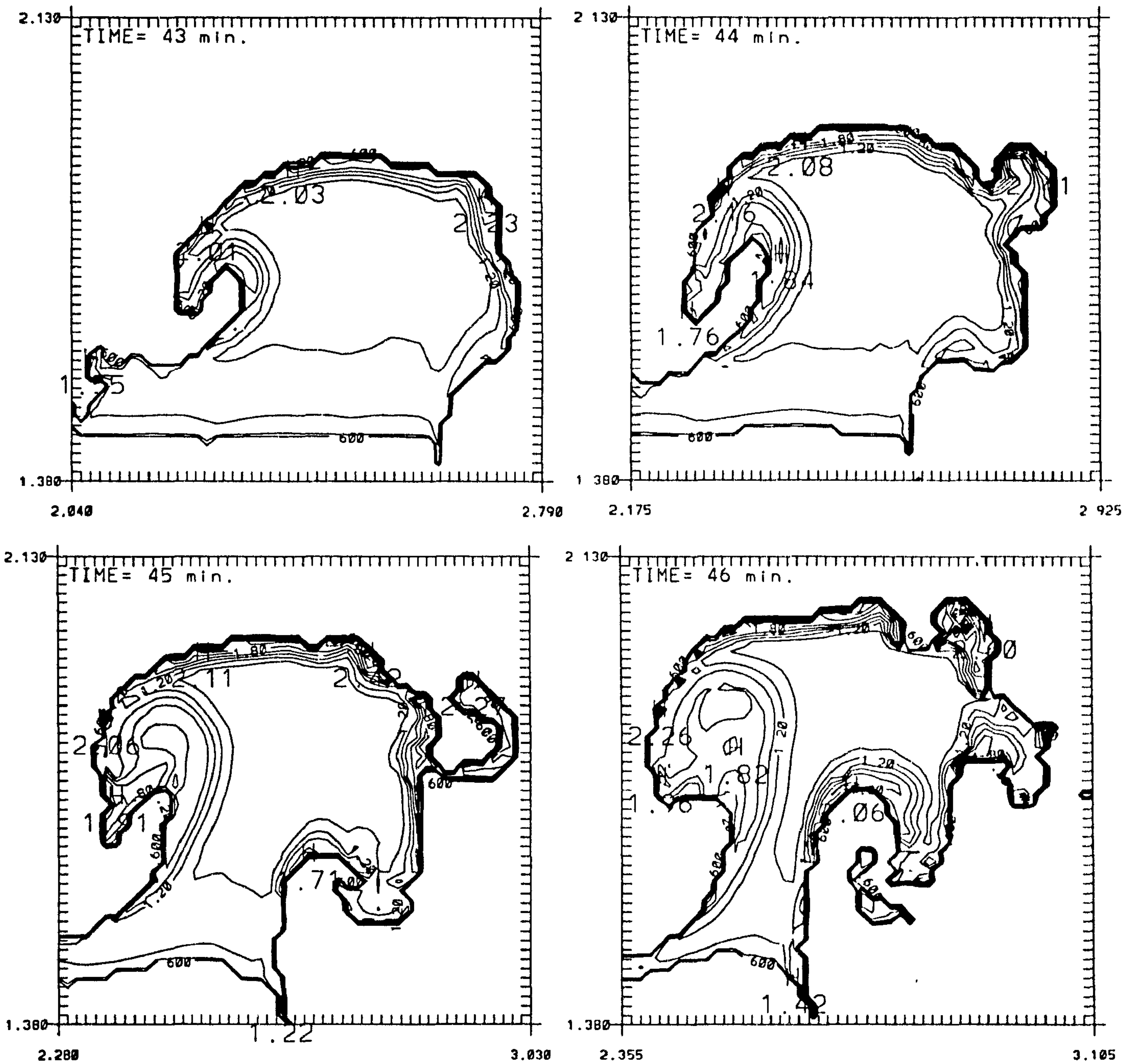

Figure 66: Standard deviation of size distribution, σ, for t = 43, 44, 45, 46min.. Contour interval of 0.2μm. H indicates high values.

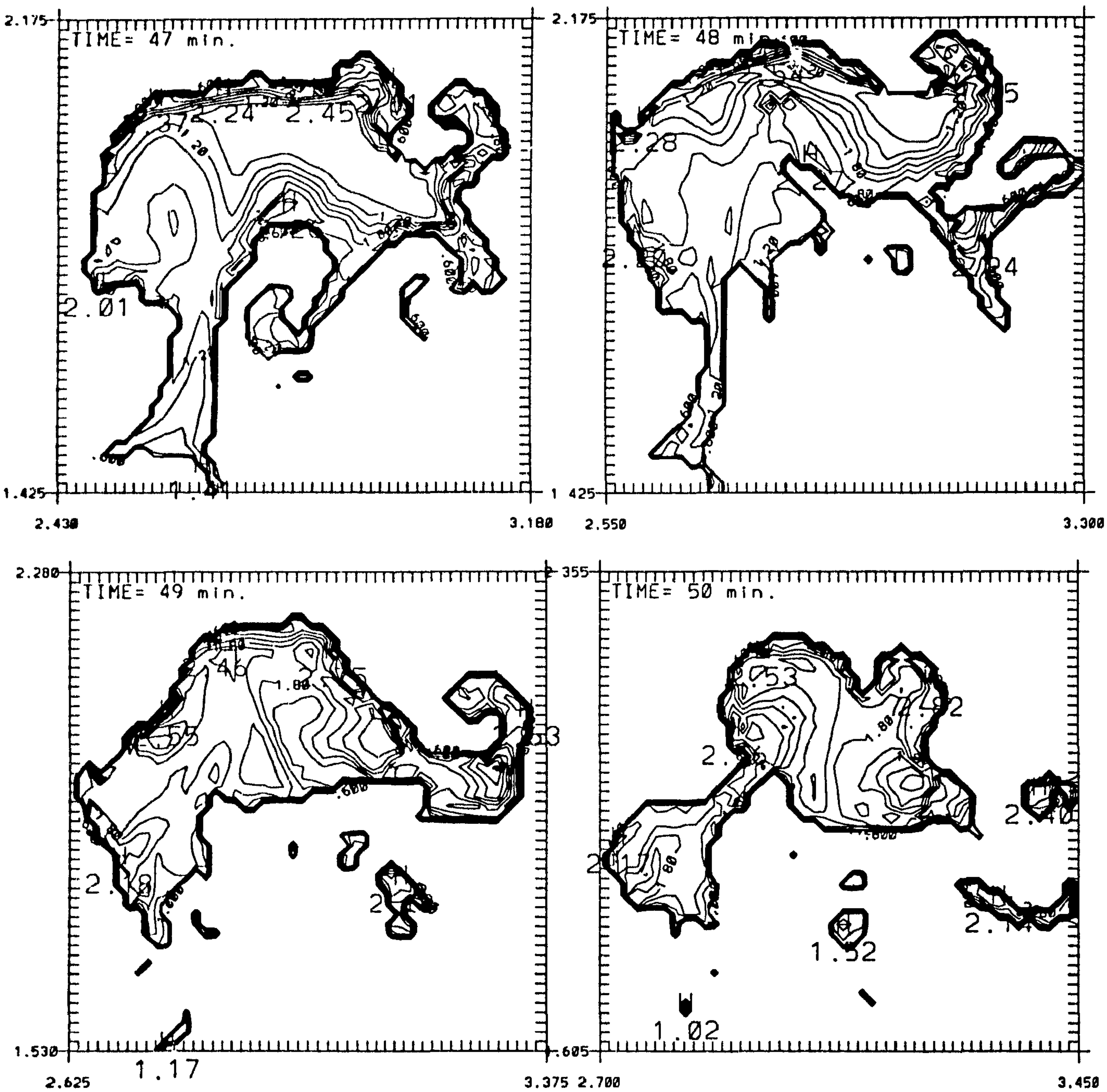

Figure 67: Standard deviation of size distribution, σ, for t = 47, 48, 49, 50$min.$. Contour interval of 0.2μm. H indicates high values.

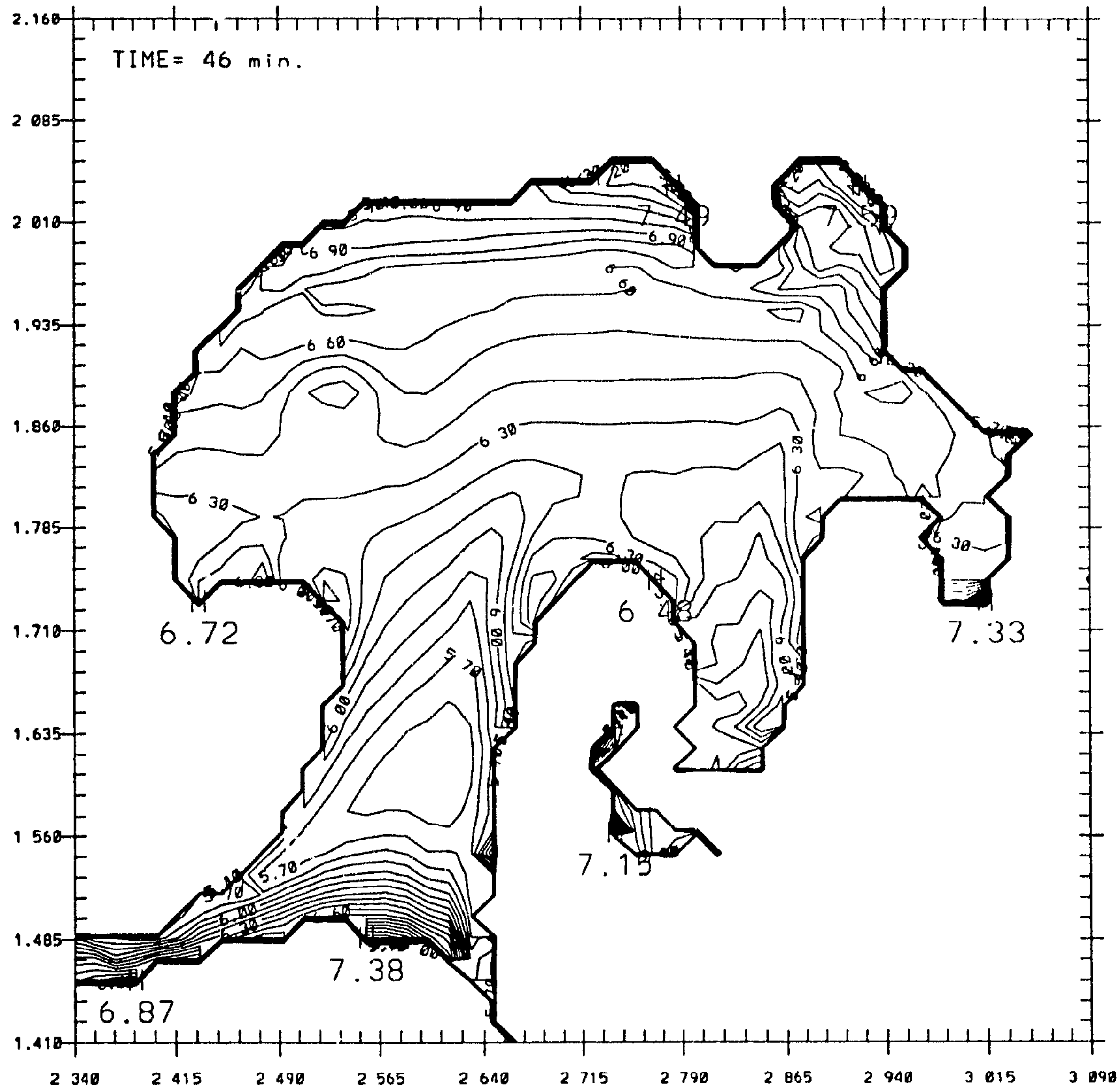

Figure 68: Equivalent radius of the mean mass of the mass density function, R_g, at $t = 46min.$. Contour interval of $0.1\mu m$. H indicates high values.

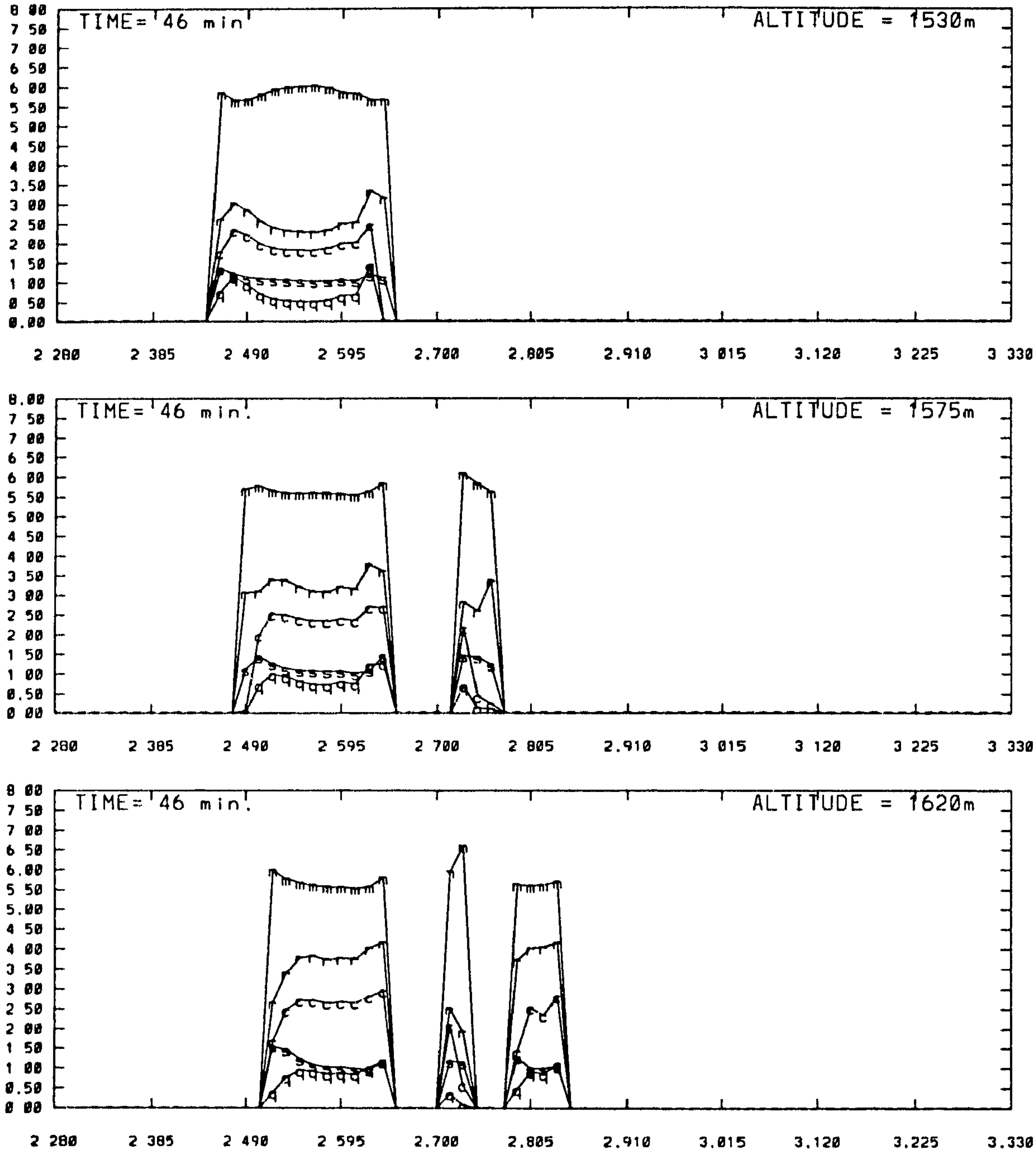

Figure 69: Horizontal cross-sections of $\overline{R}$(r–curve[μm]), σ(s–curve[μm]) , R_g(m–curve[μm]), q_c/q_c^a(q–curve) and concentration of droplets with $R > 12\mu m$(c–curve[$5 \times mg^{-1}$]) at altitudes $1530, 1575, 1620m$.

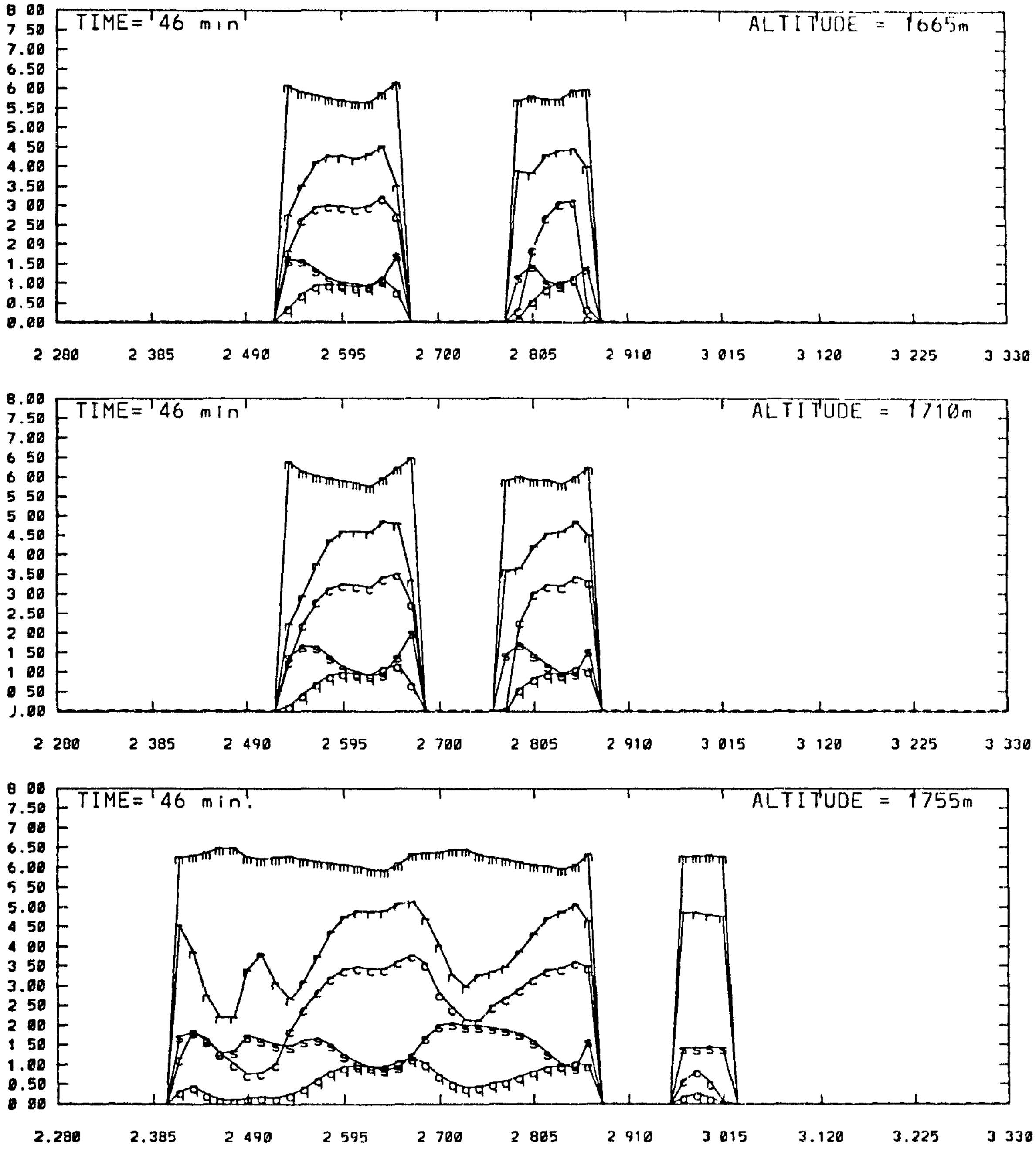

Figure 70: As in figure 69 but for altitudes 1665, 1710, 1755m.

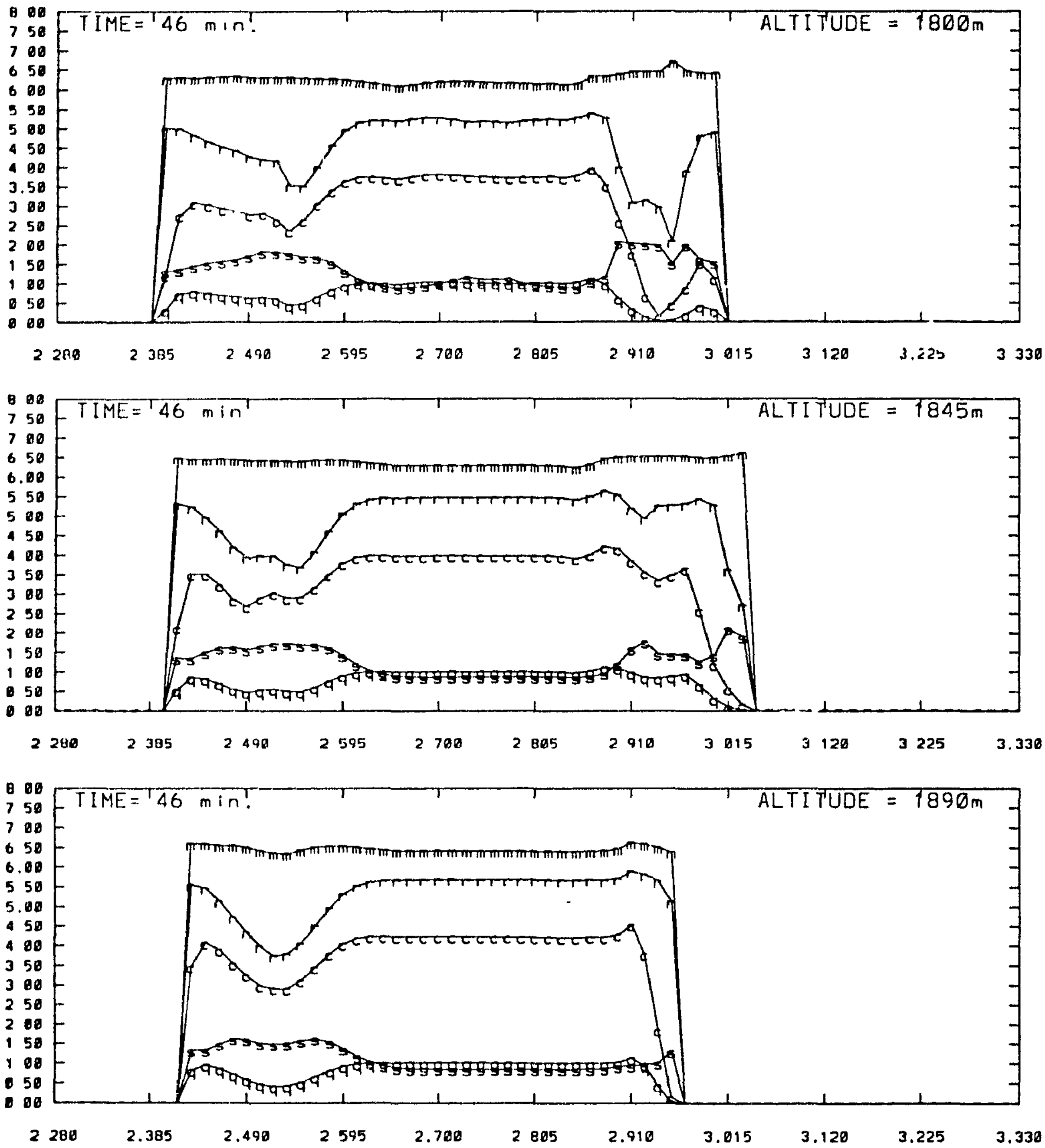

Figure 71: As in figure 69 but for altitudes 1800, 1845, 1890m.

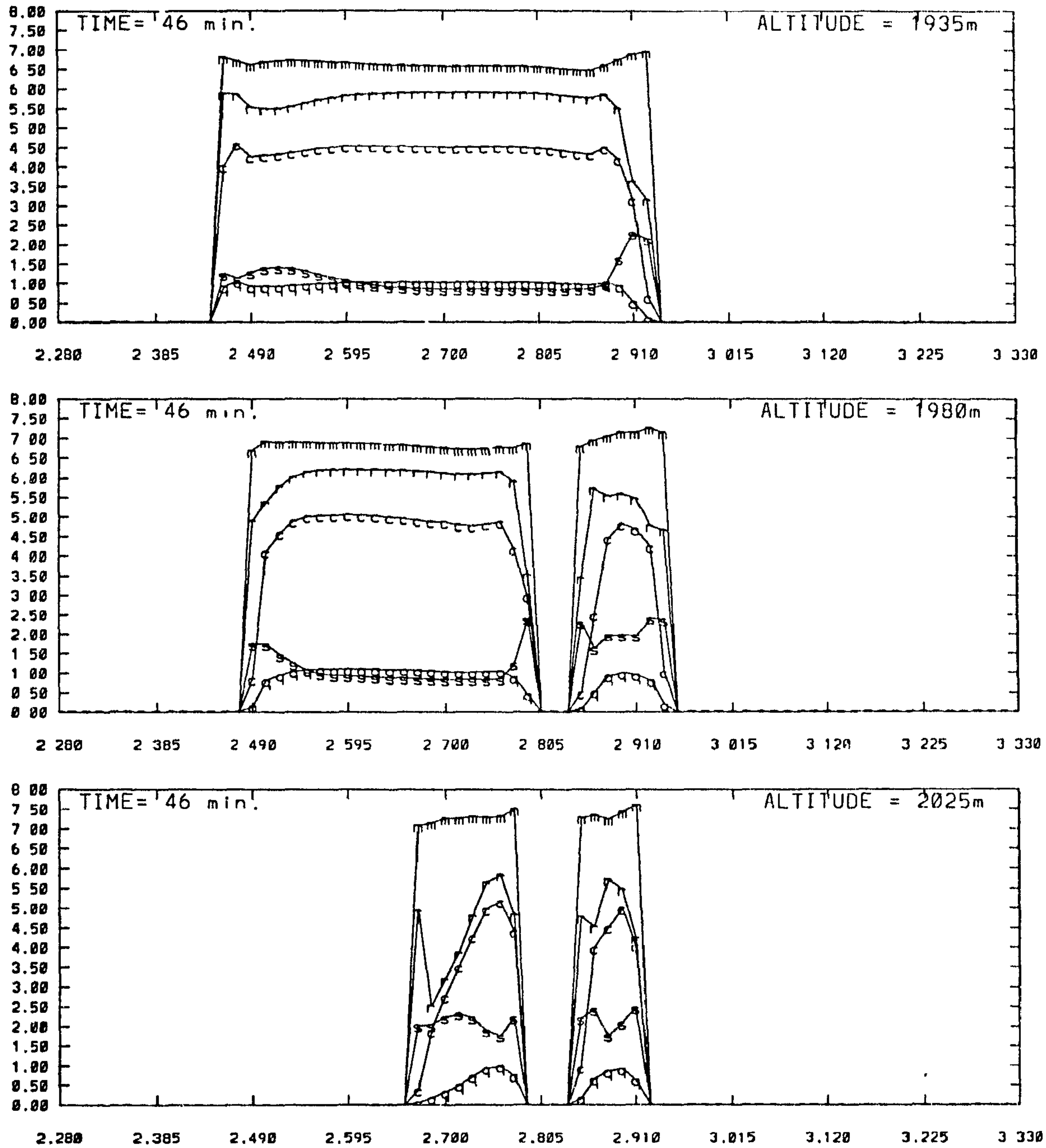

Figure 72: As in figure 69 but for altitudes 1935, 1980, 2025m.